3D NUMERICAL MODELING OF DRY/WET CONTACT MECHANICS FOR ROUGH, MULTILAYERED ELASTIC – PLASTIC SOLID SURFACES AND EFFECTS OF HYDROPHILICITY/HYDROPHOBICITY DURING SEPARATION WITH APPLICATIONS

DISSERTATION

Presented in Partial Fulfillment of the Requirements for the

Degree Doctor of Philosophy in the Graduate School of

The Ohio State University

By

Shaobiao Cai, M. S.

* * * *

The Ohio State University

2008

Dissertation committee:

Professor Bharat Bhushan, Adviser

Professor Ahmet Kahraman

Professor Noriko Katsube

Professor James Schmiedeler

Approved by

_____

Adviser

Graduate Program in Mechanical Engineering

ABSTRACT

Adhesion, friction/stiction and wear are among the main issues in magnetic storage devices, microelectromechanical systems (MEMS/NEMS), and other commercial devices having contacting interfaces with normal or tangential motion. Relevant parameters, i.e., layer thicknesses and their mechanical properties for the contact solid surfaces, the roles of meniscus and viscous forces for separation of surfaces from liquid films, need to be studied to provide a fundamental understanding of the phenomenon and the physics of the experienced problems. The simulation of contact mechanics and the modeling of separation of two surfaces with and without liquid mediated contacts are effective ways to investigate these issues.

In the simulation of contact mechanics, a numerical three-dimensional (3D) rough multilayered contact model is developed to investigate the effects of roughness, stiffness, hardness, layer thicknesses, load, coefficient of friction, and meniscus contribution of elastic-perfectly plastic solid surfaces. The model is based on a variational principle in which the contact pressure distributions are those that minimize the total complementary potential energy. The quasi-Newton method is used to find the minimum. The influence coefficients of the displacements and stresses for a multilayered contact model are determined using the Papkovich-Neuber potentials with a Fast Fourier Transform (FFT) based scheme. Contact analysis of multilayered structures under both dry and wet conditions with and without sliding which simulates the actual contact situations of those devices is performed to identify and obtain optimum design parameters including materials with desired mechanical properties, layer thicknesses, and to predict and analyze the contact behavior of devices in operation.

In the modeling of separation of two surfaces with liquid mediated contacts, numerical models of normal and tangential separation of smooth or rough surfaces are

developed. The analyses for both forces during normal and tangential separation of hydrophilic and hydrophobic smooth or rough surfaces with symmetric and asymmetric contact angles, and viscous force effects during tangential separation are presented. The important design parameters, i.e., separation distance, initial meniscus height, separation time, contact angle, and roughness are analyzed. The analyses provide a fundamental understanding of the physics of separation process and insights into the relationships between both the forces. Implications of these analyses in macro/micro/nano technologies are discussed.

Applications of the 3D multilayered rough contact model to magnetic storage devices and applications of the model of separation of two surfaces from liquid thin film to macro/micro/nano technologies are discussed.

Dedicated to my parents, my wife, and my lovely son

ACKNOWLEDGMENTS

I would like to first thank my parents and, wife for bearing with me, and my lovely son for bringing me delightful time. These make me feeling energetic in conducting my research work.

I would like give my sincere thanks to my advisor, Professor Bharat Bhushan, for his patient guidance, intellectual support, encouragement, and enthusiasm which made this thesis possible, and thank him for giving me this opportunity to work with him in the state-of-the-art laboratory to conduct engineering and scientific researches. I would like also to extend my sincere appreciation for my doctoral committee members: Professor Ahmet Kahraman, Professor Noriko Katsube, and Professor James Schmiedeler for their valuable advices and time.

Thanks are also given to Dr. Wei Peng for the valuable discussions and to friends in the laboratory for offered many help.

VITA

November 30, 1970 …..... Born, Hunan, P. R. China

1994 …..... B.S. Mechanical Engineering,

University of Science and Technology, Beijing

1998 …..... M.E. Engineering Management,

Northern Jiao Tong University

2003 …..... M.S. Mechanical Engineering,

Southern Illinois University, Carbondale, IL

2004 – present ….....Graduate Research Associate, The Ohio State University

RESEARCH PUBLICATIONS

1. Shaobiao Cai, Bharat Bhushan, 2005, A Numerical Three-dimensional Contact Model for Rough, Multilayered Elastic/Plastic Solid Surfaces, *Wear* **259**, 1408-1423.

2. Shaobiao Cai, Bharat Bhushan, 2006, Dry/Wet Contact Analysis of Multilayered Elastic/Plastic Solids with Rough Surfaces, ASME, *J. of Trib.* **128**, pp.18-31.

3. Shaobiao Cai, Bharat Bhushan, 2007, Three-Dimensional Sliding Contact Analysis of Multilayered Solids with Rough Surfaces, ASME, *J. of Trib.* **129**, 40-59.

4. Shaobiao Cai, Bharat Bhushan, 2007, Meniscus and Viscous Forces During Normal Separation of Liquid-Mediated Contacts, *Nanotechnology* **18**, 465704, 1-14.

5. Shaobiao Cai, Bharat Bhushan, 2007, Effects of Symmetric and Asymmetric Contact Angles and Division of Menisci during Separation, *Phil.Mag.* **87**, 5505-5522.

6. Shaobiao Cai, Bharat Bhushan, 2008, Meniscus and Viscous Forces during Separation of Hydrophilic and Hydrophobic Smooth/Rough Surfaces with Symmetric and Asymmetric Contact Angles, Phil. Trans. R. Soc. A, doi:10.1098/rsta.2007.2176.

7. Shaobiao Cai, Bharat Bhushan, 2008, Viscous Forces during Tangential Sliding of Micro Meniscus, *Phil. Mag.* **88**, 449-461.

FIELDS OF STUDY

Major Field: Mechanical Engineering

TABLE OF CONTENTS

LIST OF TABLES

LIST OF FIGURES

NOMENCLATURE

A_m	meniscus area
C	influence coefficients
E	Young's modulus
F	Fourier transform operator
G	shear modulus
h_k	the k^{th} layer's thickness
H_k	the k^{th} layer's hardness
H_e	effective hardness
h_m	meniscus height
$\sqrt{J_2}$	von Mises stress
p_n	nominal contact pressure
p	contact pressure
R_z	autocorrelation function
u	displacement
u_{max}	maximum displacement
U_E^*	internal complementary energy
U_E	elastic stain energy
V^*	total complementary potential energy
W	normal load
$x_{\max}, y_{\max}, z_{\max}$	location of maximum von Mises stress
$x'_{\max}, y'_{\max}, z'_{\max}$	location of maximum principal tensile stress
$x''_{\max}, y''_{\max}, z''_{\max}$	location of maximum shear stress
$\beta_x, \beta_y, \beta^*$	correlation length
v	Poisson's ratio
δ'	rigid body movement
δ	delta function
σ	standard deviation of surface heights
σ_t	principal tensile stress
$\sigma_{xx}, \sigma_{yy}, \sigma_{zz}, \sigma_{xy}, \sigma_{xz}, \sigma_{yz}$	stress components
$\varphi^{(k)}, \psi^{(k)}$	potentials
α	distance from a point to coordinate center
ξ, η	coordinates in frequency domain
γ	surface tension of liquid

μ	coefficient of friction
A_{total}	total meniscus area
A_N	individual meniscus area
D	sphere-to-flat distance
d_0	difference between meniscus height and sphere-to-flat distance
g	gravitational acceleration
F_m	meniscus force
F_v	viscous force
F_L	attractive force due to Laplace pressure
F_T	attractive force due to surface tension
F_m^*	dimensionless meniscus force
F_v^*	dimensionless viscous force
$(F_m)_{max}$	maximum meniscus force for N menisci
$(F_v)_{max}$	maximum viscous force for N menisci
F_{m-NT}	total meniscus force due to division
F_{v-NT}	total viscous force due to division
f_l, f_u	solid-liquid interfacial circumferences
f_1, f_2	intermediate functions
h	separation distance for flat-on-flat
h_s, D_s	break distance, h_s for flat-on-flat, D_s for sphere-on-flat
H(x)	geometrical shape function of a sphere
$\bar{\kappa}$	mean meniscus curvature
I_v	viscous impulse
L	separation distance
M	meniscus shape functions
N	total number of menisci
n	number of menisci in a row or column of a square contact
p	ambient pressure
Δp	pressure difference
Δp_{avg}	average pressure difference
r	arbitrary radius within a meniscus in the central plane of the meniscus in the direction of separation
R	radius of the sphere
r_1, r_2	radii of the meniscus in two orthogonal planes
r_k	Kelvin radius
r_b	liquid-air interfacial boundary
s	meniscus height for sphere-on flat
T	absolute temperature
t_s	separation time
V	molar volume
V_m	volume of the meniscus
v	translating velocity
v_0	initial meniscus volume
x'_n	radius of the outmost solid-liquid circular interface
x_{ni}	meniscus radius at the location i
x_c, y_c	the center coordinates

γ	liquid surface tension
γ_{sl}	solid-liquid interface surface tension
ϕ	filling angle
$\Delta\rho$	density difference
Ω	meniscus area
η	kinematic viscosity
$\Re$	ideal gas constant
τ	shear stress
θ	contact angle

CHAPTER 1

INTRODUCTION

1.1. Motivation

Contact of rough surfaces is very common in engineering applications. When two surfaces are brought into contact, surface roughness causes contact to occur at discrete contact spots. Deformation occurs in the region of the contact spots, establishing stresses that oppose the applied load. The sum of the areas of all the contact spots constitutes the real area of contact, and for most solid materials with applied load, this is only a small fraction of the nominal area of contact. The proximity of the asperities results in adhesive contacts caused by interatomic interactions. When two surfaces move relative to each other, the adhesion of these asperities and other sources of surface interactions contribute to the friction force. Repeated surface interactions and surface and subsurface stresses, developed at the interface, result in the formation of wear particles and eventual failure (Bowden and Tabor, 1950, 1964; Bhushan, 1996a, 1999a, b, c, 2001, 2002, 2005). The maximum contact pressure, real area of contact and surface and subsurface stresses contribute to friction and wear of two contacting rough surfaces, which are functions of surface roughness, material properties and interfacial loading conditions. The deposition of thin layers, ranging from a few nanometers to a few microns, is an effective way to improve the tribological properties of contacting surfaces because it can be used to lower the maximum contact pressure, the real area of contact and surface and subsurface stresses (Bhushan and Gupta, 1991; Bhushan, 1996b, 2001). Examples are the multilayered construction of magnetic heads and disks in magnetic rigid disk drives

(Bhushan, 1996a) and the use of low friction and low wear films such as diamond-like carbon (DLC) films on the Si substrate in MEMS/NEMS devices (Bhushan, 2007). Layers applied in these devices are as thin as 1 nm. The tribological performances of these layered solids directly depend on the layer properties. A lower contact pressure, smaller real area of contact, and lower surface and subsurface stresses are preferred to minimize friction and wear. Appropriately chosen layers can reduce the coefficient of friction and wear rate without having to change the bulk material.

With the presence of a thin liquid film at the contact interface, micro menisci form around the contacting and near-contacting asperities due to surface energy effects in the presence of a thin liquid film (Haines, 1925; Fisher, 1926; Adamson, 1990; Israelachvili, 1992; Bhushan, 1999, 2002, 2003, 2005). A small amount of liquid held at a point of contact between two solid surfaces form a meniscus which is axisymmetric or nearly so, and is often called a pendular ring. If the surfaces are slightly apart, the liquid may form an axisymmetric liquid bridge between them. Liquid bridges are formed on near-contacting asperities. For two hydrophilic surfaces, concave-shaped menisci are formed, and for two hydrophobic surfaces, convex-shaped menisci are formed. For a hydrophilic one, the lower pressure inside the meniscus, i.e., negative Laplace pressure, results in an intrinsic attractive force, called the meniscus force or capillary force, acting on the interfaces. This force results in high static friction. In some cases, this may be too high and prevent start up. High static friction due to liquid mediated adhesive force is referred to as "stiction." Stiction is a common problem in contacts involving ultra smooth surfaces and/or lightly loaded conditions such as magnetic devices and micro/nano devices which involve relative motion. For hydrophobic surfaces, a repulsive meniscus force will act. The resultant force, adhesive or repulsive, is highly dependent on the formed meniscus area, contact angles, number of menisci, separation time, and surface tension and viscosity of the liquid. Meniscus size and shape are also a central part to characterizing the condensation and evaporation in porous media as reported by Defay and Prigogine (1966), Everett (1967), and Melrose (1966). When separation of two surfaces is required, the viscosity of the liquid requires an additional viscous force for shearing. If hydrophilic surfaces are used, both meniscus force and viscous forces will

contribute to an adhesive force which leads to high adhesion, friction and stiction. In order to reduce the adhesion, friction and stiction due to the formed menisci, it is necessary to understand the forces involved and their roles.

1.2. Research objectives and scope

Adhesion, friction, stiction, and wear are among the main issues in magnetic storage devices and micro/nanoelectromechanical systems /nanoelectromechanical systems (MEMS/NEMS), having contact interfaces with normal or tangential motion. The adhesion, friction, stiction, and wear are known to be associated with contact statistics, contact stresses, and meniscus and viscous forces (when a liquid film presents at the contact interface). Numerical models which simulate the actual contact situations of those devices are needed to obtain those information and to optimum design parameters including materials with desired mechanical properties, layers thickness, and to predict and analyze the contact behavior of devices in operation. In the current work, numerical models, namely, a 3D contact model of rough multilayered solid surfaces and models for separation of two surfaces from liquid mediated contacts in normal and tangential directions, are developed. The purpose of the work is to understand the mechanics of rough multilayered surfaces in contact and the roles the forces involved in separation of two surfaces from liquid mediated contacts, and to obtain lower adhesion, friction, stiction and wear. The literature review is presented in this chapter in section 1.3 and section 1.4.

For the numerical 3D contact modeling of rough multilayered solid surfaces, the objectives are to develop a rough multilayered contact model to predict the contact statistics (fractional contact area, the value of contact pressure) and stresses, and to identify optimum design parameters of surfaces and layers for layered media through the trend studies of the contact statistics and contact stresses by using computer generated rough surfaces. In this model, real area of contact, contact pressure profiles, maximum stresses (von Mises, principal tensile and shear stresses) are calculated. The formulations of these stresses are listed in Appendix A. Plastic contact area is calculated based on the onset of plasticity information of the elastic-perfectly-plastic contact model. A larger real

area of contact indicates higher friction, and higher contact pressure and stress levels indicate higher potential of wear. The von Mises stresses are calculated as these relate to the von Mises yield criterion. According to this criterion, plastic yielding initiates once the maximum von Mises stresses reaches the yield stress in pure shear. Principal tensile stresses are calculated as these affect propensity of crack propagation which is important in brittle materials. Shear stresses are calculated as they relate to another commonly used Tresca yield criterion. According to this criterion, the yielding will occur when the maximum shear stress reaches the yield stress in pure shear. In addition, the maximum shear stress relates to delamination in layered solids (Bhushan, 1999, 2002). These models have been used to study the effects of roughness, layer properties, i.e., stiffness, hardness and layer thickness, load and coefficient of friction. These results have been used to study the trend of friction and wear of rough multilayered solid surfaces in contact. The work for numerical 3D contact modeling of rough multilayered solid surfaces and the relevant recommendations for future work are presented in chapter 2.

For the modeling of separation of two surfaces from liquid mediated contacts, the objectives are to develop a numerical approach to characterize meniscus and viscous forces during normal and tangential separation of two liquid-film mediated surfaces, with/without roughness, to provide a fundamental understanding of the physics of the separation processes, and to provide criteria for design of interface with lower adhesion and friction. The models include dynamic normal separation of both hydrophilic and hydrophobic surfaces and tangential separation of hydrophilic surfaces with liquid-mediated contacts. These models apply for rigid body only without considering solid-solid adhesion. The equations developed to calculate viscous force during normal or tangential separation are analytically formulated and can be used to calculate the forces at arbitrary separation distance. The effects of separation distance, initial meniscus height, separation time, contact angle, division of menisci, and roughness on both meniscus and viscous forces are reported and discussed in detail. Examples of applications and recommendations are shown in the field of the magnetic storage devices, digital micro-mirror devices, and diesel fuel injectors. The work for modeling of separation of two

surfaces from liquid mediated contacts and the relevant recommendations for future work are presented in chapter 3.

Conclusions of the two parts are presented in chapter 4.

1.3. Contact of solid surfaces

Due to the complex of the problem, numerical approaches are commonly used to study the contact mechanics of two solid surfaces in contact. The numerical approaches, such as finite difference method (FDM), finite element method (FEM), or boundary element method (BEM), are commonly used to perform simulation tasks for contact problems depending on the way the rough solid is being divided. FDM discretizes the entire object into finite elements. An algebraic equation of stresses and displacements is created by enforcing the governing differential formulation of elasticity on each node inside the whole object. FDM has the advantages of simplicity and parallelization, but is limited for the regular domain and not for complex geometries or non-isotropic material, e.g., a layered rough surfaces contact. FEM employs the governing integral formulation of elasticity rather than the differential formulation of elasticity in each element inside the whole object to create an algebraic equation (Zienkiewicz, 1977; Beer and Watson, 1992). FEM has a good adaptability and theoretically is capable of solving rough surface contact, for example by Komvopoulos and Choi (1992), Oden and Martin (1985), Martin et al. (1990), and Kikuchi and Oden (1988). BEM is an effective method to solve partial differential equations. When BEM is used to solve contact problems, the governing differential equations set for contact pressure, stress, and displacement for the continuous region inside the object is transformed to the corresponding boundary integral equation set for the surface of the object. The boundary integral formulation of elasticity is employed on each boundary element to create an algebraic equation. In general, FEM and BEM are more flexible than FDM, and theoretically both are applicable to multiple asperity contact. As compared to FEM, BEM can achieve high computational efficiency due to the discretization of only the contact interface (Man, 1994). A contact problem can be formulated with different principles depending on the complexity of the problem. Typically, there are three methods to formulate the problem, namely, direct formulation,

weighted residual formulation, and minimum total potential energy formulation. The minimum total potential energy formulation allows the use of a quadratic programming method, such as the quasi-Newton method, to solve an optimization problem, which theoretically guarantees the convergence and the uniqueness of the solution. The conjunction of minimum total potential energy formulation with the BEM approach is feasible to solve the 3D rough surfaces contact problems with a large number of contact points due to their associated advantages. Thus, the multilayered rough contact model can be simulated based on them. The relationship of these approaches and methods is shown in Fig.1.1.

Layered surfaces in contact have long been of interest. A number of numerical models for the contact of layered surfaces have been developed to find the pressure and stress distributions. For analysis of a single asperity contact, stress and deformation equations are written in terms of harmonic functions, e.g., Green function in two dimensions and Papkovich-Neuber potentials in three dimensions. Fast Fourier Transformation (FFT) is commonly used to speed up the computation, for example by Nogi and Kato (1997), Peng and Bhushan (2001), and Liu and Wang (2002). A single layer on a half space under prescribed axisymmetric normal loading was initially done by Burmister (1945) and extended by Chen (1971) to axisymmetric and non-axisymmetric loading for the analysis of stress state. O'Sullivan and King (1988) obtained a set of explicit forms of so called influence coefficients to describe applied load-displacement and applied load-stress relations by using Papkovich-Neuber potentials to study the contact of a spherical indenter with a single layered flat surface. A least square method was used to find the pressure distribution under the indenter. Kral and Komvopoulos (1997) developed a 3D model to analyze the elastic-plastic contact of a rigid smooth sphere sliding on a layered, smooth and flat solid; Plumet and Dubourg (1998) studied the contact of a smooth rigid ellipsoid with a layered elastic half space using FFT scheme.

Surface roughness has been taken into consideration in later studies. Merriman and Kannel (1989) adopted a 2D cylindrical single asperity contact model and introduced roughness as a height perturbation relative to the smooth cylinder. An influence matrix

containing influence coefficients for the 2D layered elastic solid based on point loads was constructed by using the Gupta and Walowit (1974) equation (which was developed for a 2D cylindrical single asperity in contact with a layered elastic solid) to study the contact pressure distributions with or without a soft layer. A conventional matrix inversion technique and an iterative process were used to obtain the contact pressure distributions and real area of contact. Cole and Sayles (1992) performed a contact analysis of a 2D layered elastic solid and a rough elastic indenter by using the same technique used by Gupta and Walowit (1974) and Merriman and Kannel (1989). The introduced rough surface was represented as an array of points at a fixed distance with certain heights, and the integral part of normal surface deflection was evaluated by a least square method. Unit constant pressures instead of unit point loads were used to avoid assumptions of the size of sampling interval and layer thickness. Mao et al. (1996,1997) extended Cole and Sayles (1992) approach from normal contact to frictional contact. A 2D quasi-sliding contact of an elastic rough cylinder on an elastic layered half-space was performed to calculate the stress fields.

3D rough single layered contact models were also developed by researchers. Nogi and Kato (1997) used the 3D influence coefficients initially developed by O'Sullivan and King (1988), to study the stress field, displacements, and pressure distributions for a rough indenter in contact with a flat single layered surface. Conjugate gradient method was applied to solve a system of linear equations that relate pressure to displacement for unknown pressures during iterative processes. The technique is good to solve for pressure distributions for rough surfaces with a moderate number of contact points. However, with an increase of contact points and layers, the influence coefficient matrices can become very large and possibly ill-conditioned due to round-off errors. In order to avoid this problem, Peng and Bhushan (2001) extended a variational approach (which was introduced by Tian and Bhushan (1996) for homogeneous rough surfaces contact models) to study single layered rough surfaces in contact under both normal and tangential loading. The variational approach employs minimum total complementary potential energy method to formulate the problem. It uses a quadratic programming method to solve the problem and guarantees the uniqueness of the solution. Thus, it's feasible to

solve the 3D rough surface contact problem with a large number of contact points and reduces computing time. The model was also used to perform quasi static sliding contact analysis (Bhushan and Peng (2002) and Peng and Bhushan (2002, 2003)). In quasi static sliding, friction force is introduced at the contact points, but no physical motion is considered. In the current work, the rough single layered contact model was the first time (in the literature to our best knowledge) further extended to multilayered rough surface contact under combined normal and friction forces to simulate the real contact phenomena of multilayered surfaces.

In this model, real area of contact, contact pressure profiles, maximum stresses (von Mises, principal tensile and shear stresses) are calculated. The formulations of these stresses are listed in Appendix A. Plastic contact area is calculated based on the onset of plasticity information of the elastic-perfectly-plastic contact model. A larger real area of contact indicates higher friction, and higher contact pressure and stress levels indicate higher potential of wear. The von Mises stresses are calculated as these relate to the von Mises yield criterion. According to this criterion, plastic yielding initiates once the maximum von Mises stresses reaches the yield stress in pure shear. Principal tensile stresses are calculated as these affect propensity of crack propagation which is important in brittle materials. Shear stresses are calculated as they relate to another commonly used Tresca yield criterion. According to this criterion, the yielding will occur when the maximum shear stress reaches the yield stress in pure shear. In addition, the maximum shear stress relates to delamination in layered solids (Bhushan, 1999, 2002). These models have been used to study the effects of roughness, layer properties, i.e., stiffness, hardness and layer thickness, load and coefficient of friction. These results have been used to study the trend of friction and wear of rough multilayered solid surfaces in contact. Applications using the analysis is discussed.

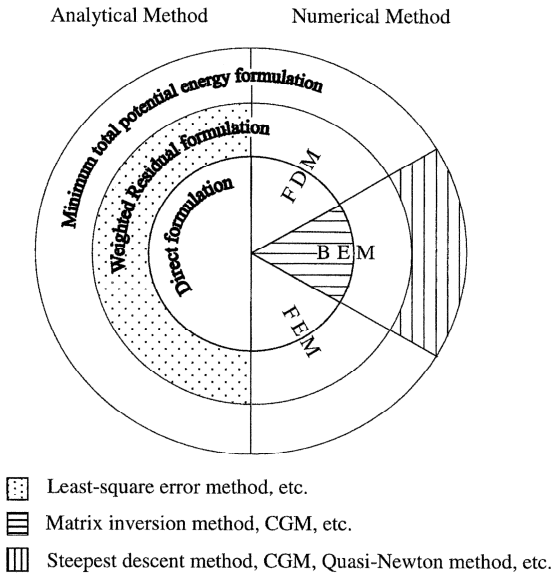

Figure 1.1 Various methods classified into several categories: direct, weighted residual, and minimum total potential energy formulations in radial direction; analytical and numerical (Finite Difference Method or FDM, Finite Element Method or FEM, Boundary Element Method or BEM) methods in circumferential direction. Among them, the analytical weighted residual formulation applies exclusively to single asperity contact, and the numerical direct formulation and minimum total potential energy formulation apply toboth single asperity contact and multiple asperity contact [Bhushan and Peng, 2002].

1.4. The study of meniscus and viscous forces

When a thin film liquid presents at the contacting interface, both meniscus and viscous force play important roles when separation of two surfaces is needed. Meniscus (capillary) forces have been of interest due to their relevance to many fields of study and their many industrial applications, for example the investigations of friction/stiction in an atomic force microscope (AFM) tip in contact with a sample, and the contacts in magnetic storage devices, micro/nano devices, and fuel injectors in automobiles (Bhushan, 1994; 1996a, b, 1998, 1999, 2001, 2002, 2005, 2007, Bhushan and Peng, 2002), microassembly through micromanipulation (Obata et al. 2004; Chandra and Batur, 2006), adhesion in bio-creatures (the forces developed for attachment by insects, spiders and lizards to various surfaces) (Gorb, 2001), soil mechanics (Haines, 1925; Fisher, 1926; Bachmann and van der Ploeg, 2002), concrete mechanics (Bentz et al., 1995), and granular materials (Bocquet et al., 1998; Halsey and Levine, 1998).

The experimental studies have primarily focused on the effect on adhesive forces of factors such as the size of the surfaces, liquid properties (surface tension, contact angle, and viscosity), and operating conditions (including temperature, humidity, and velocity). The effect of humidity on adhesion was studied by McHaffie and Lenher (1925). They showed that the thickness of the film and adhesion both increase with an increase of humidity. McFarlane and Tabor (1950) conducted quantitative studies on adhesion due to liquid film through a number of experiments. They observed that with a clean hard surface in dry air, adhesion is negligibly small; however, adhesion is appreciable in moist air. Similar observations of the effect of humidity on adhesion have been made by Miyoshi et al. (1988). As shown in Fig. 1.2, they reported that the effect of water vapor on the adhesive force for a hemispherically-ended pin of Ni-Zn ferrite in contact with a flat Ni-Zn ferrite surface. Measured adhesive force under a saturated condition (~100% relative humidity) could be calculated using the meniscus equation, which verified that the source of adhesion was a meniscus, and meniscus contribution can be significant. Shaw (1986) studied meniscus forces for the fluid interactions for embedded particles. More experimental measurements of the meniscus forces have been reported by O'Brien and Yu (1972), Hotta et al. (1974), Padday et al. (1975), and

Bayramli et al. (1978). In addition to the meniscus force, the importance of viscous force to adhesion was stressed by Bikerman (1947, 1950). McFarlane and Tablor (1950) examined the relationship between the viscous force and separation time by separating a glass lens with a pool of castrol oil. The force as a function of separation time at temperature 18^{o} and 22^{o}C is shown in Fig. 1.3. It was reported that the product of the slope and the viscosity is a constant which implies that the viscous force is proportional to the liquid viscosity and separation rate, implying Newtonian viscous flow.

The numerical approaches mainly include the calculation of meniscus curvature and forces for selected contacting surfaces with a certain shape and size. Particular attention has been given to the determination of liquid bridges between two spheres (Fisher, 1926; Rose , 1958; Woodrow et al., 1961; Cross and Picknett, 1963a, Mason and Clark, 1965; Melrose, 1966; Heady and Cahn, 1970; Hotta et al., 1974); a sphere and a flat surface (Cross and Picknett, 1963b; Clark et al., 1968; Orr et al., 1975); flat-on-flat surfaces (Fortes, 1982; Carter, 1988); and two cylinders (Erle et al., 1971). Some other analyses are also available to study the stability of the curvature (Mastrangelo and Hsu, 1973; de Boer and de Boer, 2007), creep rupture modeling (Tsai and Raj, 1982; Marion et al., 1983), and kinetics of meniscus force (Mate, 1992; Chilamakuri and Bhushan, 1999). More complete meniscus curvature solutions can be found in the study performed by Orr et al. (1975), who took a sphere-on-flat case and reported a systematic set of solutions for different shapes of meniscus profiles in terms of elliptic integrals of pendular rings for negligible gravity cases. Surface roughness, properties of layered contacting solids (such as layers' Young's modulus and hardness), and liquid film thickness (including relative humidity), have also been introduced in many later studies. Tian and Bhushan (1996) studied the micro-meniscus effect based on a multiasperity contact model for homogeneous solids. Peng and Bhushan (2001) and Cai and Bhushan (2006) studied the meniscus effects in rough layered contact models and examined the dependence of meniscus force on layer properties.

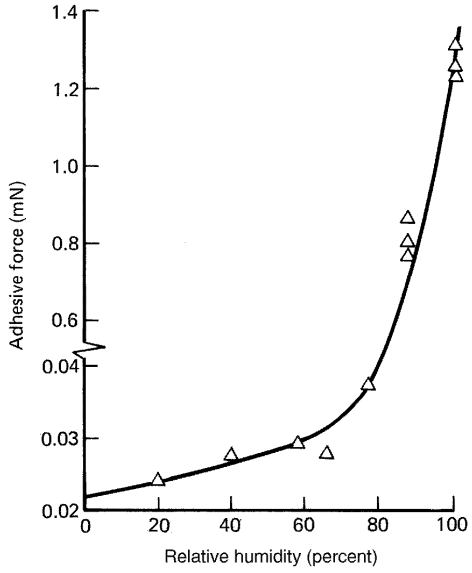

Figure 1.2. Effect of humidity on adhesion of a hemispherically ended pin of 2 mm radius of Ni-Zn ferrite in contact with a flat of Ni-Zn ferrite in nitrogen atmosphere in the load range of 0.67-0.87 mN [Miyoshi et al., 1988].

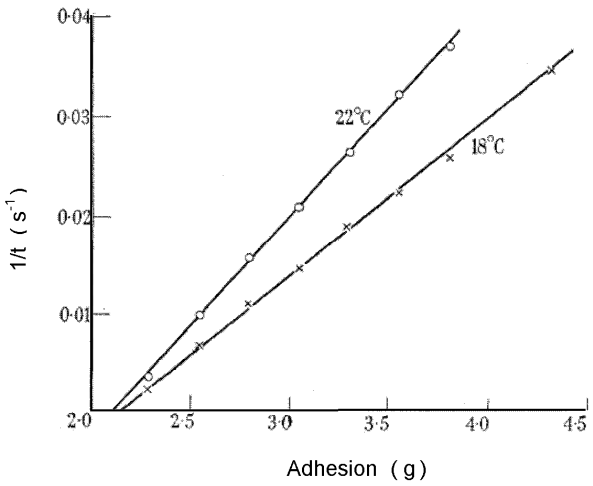

Figure 1.3. Adhesion as function of time of separation, glass lens resting in a pool of castor oil [McFarlane and Tabor, 1950].

The numerical studies on meniscus forces just reported were based on static contact configurations. However, in many practical devices, the separation of two contacting surfaces occurs within a short designated time. The criteria for dealing with practical engineering problems such as the design of macro/micro/nano devices based on static meniscus force is not sufficient. During separation of two surfaces from liquid mediated contacts, an external force larger than the meniscus force is needed to initiate the separation process. After the initial motion, both meniscus and viscous forces operate inside the meniscus. During separation, the meniscus force continues to decrease with the separation distance because of decrease in the meniscus area, whereas the viscous force continues to increase with the separation distance. Either meniscus or viscous force can be a dominant one during the separation process.

The study of dependence of the meniscus force on separation distance has been carried out by a number of authors, for example by Huppmann and Rieggger (1975), Fortes (1982), Carter (1988), Gao (1997), Stifter et al. (2000), and de Boer and de Boer (2007), who investigated meniscus force-distance relationship, which is one of the important relationships during separation. Stifter et al. (2000) further reported the relative contribution of meniscus and van der Waals forces (solid-solid adhesion) as a function of separation distance due to the effect of relative humidity (p/p_0) and sphere radius as shown in Fig. 1.4. The results present a clear picture that the meniscus force is an important source of adhesion, and it can be a dominant one when the separation of two surfaces goes beyond about 0.5 nm in the studied cases. The distance dependence of meniscus forces was presented, whereas, these studies were confined to a purely static meniscus force analysis since viscous force was not considered. Chan and Horn (1985) calculated the viscous force due to viscous dissipation for the case of a sphere moving normally to a flat surface with some separation by using the Reynolds lubrication equation. The force equation derived is suitable for an infinitely wetted region. Matthewson (1988) modified the viscous force equation to be applicable to a finite wetted region. The model works if the break distance is much larger than the radius of the meniscus. But it leads to an error when the separation distance is comparable to the radius of the meniscus.

The vibration of the surfaces would affect the forces involved in the separation of two surfaces with liquid bridges. As a result of vibration, meniscus may get broken and affect the separation distance, consequently, meniscus forces. The vibration is expected to contribute mainly to the viscous force due to viscous dissipation. Matsuoka et al. (2002) analyzed the dynamics of a meniscus bridge between two parallel flat surfaces by assuming a small vibration of the spacing. The application of the analysis may be limited since the meniscus bridge remains unbroken, and the force capacity is largely dependent on a prescribed displacement function which is practically unknown beforehand. Analysis of the viscous force contribution has not been carried out.

It is know that high adhesion, friction and stiction are among the main issues for many devices such as discussed at the beginning. In order to reduce the adhesion, friction and stiction, it is necessary to understand the forces involved and their roles. In the current study, we first developed models to study the meniscus and viscous forces during the separation of two hydrophilic smooth surfaces with symmetric contact angles. These models are then extended to investigate asymmetric contact angles by integrating a moving boundary technique into the previous numerical simulation to capture the liquid-solid interface differences between the two sides of a meniscus. These models are further extended to investigate the separation of two hydrophobic surfaces and to investigate the viscous force during tangential separation process. As compared to the models available in the literature, the current models developed can be used to calculate both meniscus and viscous forces at arbitrary separation distance in a whole dynamic separation process. The effects of separation distance, initial meniscus height, separation time, contact angle, division of menisci, and roughness on both meniscus and viscous forces are reported and discussed in detail. Examples of applications and recommendations are shown in the field of the magnetic storage devices, digital micro-mirror devices, and diesel fuel injectors.

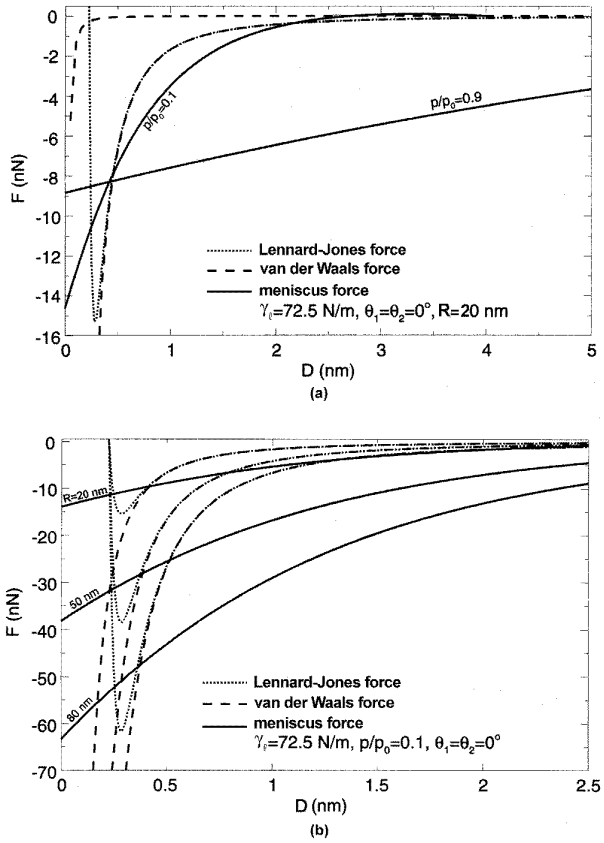

Figure 1.4. Relative contribution of meniscus and van der Waals forces as a function of separation distance (D), (a) effect of relative humidity (p/p_0), and (b) sphere radius (R) [Stifter et al., 2000].

CHAPTER 2

DRY AND WET CONTACT MODELING OF MULTILAYERED ROUGH SOLID SURFACES

The deposition of thin layers, ranging in thickness from a couple of nanometers to a few microns, has been proven to be an effective way to improve the tribological performances of contacting solids. Numerical models of layered surfaces in contact have been widely employed to study the contact mechanics and failure mechanisms like fracture, delamination, friction/stiction, and wear. The goals are to better understand contact phenomena and to provide design criteria for better contact qualities. Three methods, namely, direct formulation, weighted residual formulation, and minimum total potential energy formulation, are used to formulate the contact problems depending on the complexity of the problem, and the numerical techniques like FEM and BEM are commonly used to perform the simulation dependent on the way the elements are divided in contacting solids. In this section, the modeling work of a smooth single asperity and a rough spherical surface in contact with a single-layered flat surface will be briefly reported, and a comprehensive report will be given to the modeling of the contact of rough multilayer solid surfaces under both dry and wet conditions.

2.1. Dry contact modeling of multilayered rough solid surfaces

The studies of layered solid based on single and multiple asperities contact will be discussed in this section.

2.1.1. Single asperity contact

Single asperity contact is the basic component of multiple asperity contact, and therefore is of interest to better understand multiple asperity contact. Due to its simplicity, it usually has a unique solution, which makes it an ideal solution validation case for models developed for multiple asperity contact. Comprehensive reviews of the modeling of both homogenous and layered single asperity and multiple asperity contact have been presented by Bhushan (1996b, 1998) and Bhushan and Peng (2002). Here we review the models for layered single asperity contact. The asperity is usually assumed to be cylindrical, elliptical, or spherical. Since the approaches used for a single asperity contact are similar, only the modeling of a spherical asperity in contact with a layered flat surface is reported here for brevity. Figure 2a shows a schematic of an elastic sphere (with stiffness E_0) of radius R in contact with a layered elastic half-space. The real contact domain is represented by the contact radius a. In general, a is prescribed, and δ is the corresponding relative approach which is an unknown. Geometrical overlap is not allowed, and the adhesive forces are assumed negligible, i.e., no normal tension is allowed, and contact pressures must be positive or zero everywhere.

The single asperity contact problem is then framed in a polar coordinate system as

$$
\begin{aligned}
&u_{z0}(r,0) + u_{z1}(r,0) = u^*_{z0}(r,0) + u^*_{z1}(r,0), \quad |r| \le a \\
&u_{z0}(r,0) + u_{z1}(r,0) > u^*_{z0}(r,0) + u^*_{z1}(r,0), \quad |r| > a \\
&p(r) \ge 0, \quad |r| \le a \\
&p(r) = 0, \quad |r| > a
\end{aligned}
\tag{2.1}
$$

where p is the contact pressure, r is the distance from the center of the contact zone, u_{zi} and u^*_{zi} are the calculated and prescribed z-direction surface displacements of the sphere and the layered half-space over the real contact domain (identified by indices 0 and 1, i is

used here to represent 1 or 2), respectively. $u_{zi}(r,0)$ and $p(r)$ must also satisfy the governing formulation of elasticity in terms of surface displacements and contact pressures. Since the sum of prescribed z-direction surface displacements $u^*_{z0}(r,0)+u^*_{z1}(r,0)$ in the real contact domain is a function of R and a and thus known, so is $u_{z0}(r,0)+u_{z1}(r,0)$. The problem then becomes to find the contact pressure profile $p(r)$ satisfying the governing formulation of elasticity with given $u_{zi}(r,0)$.

Chen and Engel (1972) further expressed $u^*_{z0}(r,0)+u^*_{z1}(r,0)$ as $w(r)$, the surface profile of the indenter before deformation in reference to a cutting plane set at δ below the
cylinder top. Gupta and Walowit (1974) and O'Sullivan and King (1988) expressed $u^*_{z0}(r,0)+u^*_{z1}(r,0)$ as $w(r) + u_{z0}(a,0) + u_{z1}(a,0)$, where $w(r)$ was the undeformed surface profile of the indenter in reference to a cutting plane corresponding to $r = a$. Due to the geometrical simplicity of the single asperity, the problem is well-defined and thus a unique solution is guaranteed. Even though the formulation of the problem is not very complicated, obtaining an exact solution for the single asperity contact of layered surfaces is usually mathematically complicated and unnecessary. The contact pressure and stress profiles are usually found based on three approaches, namely, weighted residual method (for example least-square error method), BEM method, and FEM.

For the weighted residual method, i.e., least-square error method (for example by Chen, 1971; Chen and Engle, 1972; King and O'Sullivan, 1987, O'Sullivan and King, 1988; Gupta et al., 1973), under the approximated pressure distribution, the square error between the prescribed and calculated surface displacements over the real contact domain should be minimal. First, the unknown pressure distribution under the indenter is approximated in a series of simple basis functions, i.e., $p(r) = \sum_{j=1}^{N} a_j p_j(r)$, where a_j are unknown coefficients. The surface displacements $u_{zi,j}(r,0)$ due to $p_j(r)$ acting alone are calculated directly, either analytically or numerically. The total $u_{zi}(r,0)$ is obtained by assembling $u_{zi,j}(r,0)$. For materials with linear elasticity and small strain behaviors, the assembling is a simple linear superposition. The square of the error over the real contact domain due to the approximation is given as

$$\varepsilon^2 = \frac{1}{a^2}\int_0^a [u_{z0}(r,0) + u_{z1}(r,0) - w(r)]^2 \, r dr \tag{2.2}$$

Substituting $u_{zi}(r,0)$ into Eq. (2.2) and minimizing ε^2 with respect to the unknown coefficients a_j and d results in the pressure distribution in the contact zone.

BEM approach discretizes only the surface of the single asperity, thereby reducing the size of the problem and dramatically reducing the effort involved in obtaining the solution. A matrix inversion method (for example by Gupta and Walowit, 1974; Cole and Sayles, 1992), or quasi Newton method (for example by Peng and Bhushan, 2002), may be used in finding the contact pressure profile. For the BEM, the pressure and displacement are expressed as

$$[u_z^*] = [C^{u_z}][p], \tag{2.3}$$

where p is the vector of contact pressures and is denoted by $[p]^T = [p_1, p_2, \cdots p_{k,} \cdots p_M]$, $[u_z^*]$ is the total prescribed z-direction displacements vector and is denoted by $[u_z^*]^T = [u_{z1}^*, u_{z2}^*, \cdots u_{zk}^* \cdots u_{zm}^*]$, and $[C^{uz}]$ is the matrix of influence coefficients corresponding to $[u_z^*]$, which is developed in Section 2.1.3. It contains the surface displacements $u_{zi,j}(r,0)$ due to unit point load $p_j(r)$ acting alone.

FEM is a popular approach used to solve the single asperity contact problem, for example by Komvopoulos (1988, 1989), Diao et al. (1994), Smith and Liu (1953), Kral et al. (1993, 1995a,b), Stephens et al. (2000), Kral and Komvopoulos(1996a, b, 1997). FEM software packages are usually involved in the modeling. In FEM modeling, the selection of element type and meshing scheme affect the solution directly. For the single asperity contact, since only a relatively small number of regular shaped elements are in contact, they can be easily refined without exceeding the upper limit of the number of elements in the software. In this case, FEM provides rigorous results.

Representative results for the contact of a spherical asperity with a layered flat surface are shown in Fig. 2.1b and Fig. 2.2. Fig. 2.1b shows the contact pressure profile beneath the sphere. As compared to the homogeneous solid, the contact radius decreases while the contact pressure increases with a stiffer layer ($E_1/E_2 > 1$) and vice versa. Fig. 2.2 shows the contours of von Mises stress $\sqrt{J_2} / p_0$ at y = 0 at various E_1 /E_2 and coefficient of friction μ. It is observed that a stiffer top layer leads to higher maximum contact stresses, whereas a compliant top layer leads to smaller maximum contact stresses as compared to the homogeneous solids regardless of friction. The results also show that the introduction of friction leads to higher maximum stress level for the same solid, and the increase in the coefficient of friction leads the location of the maximum stress to move toward the surface.

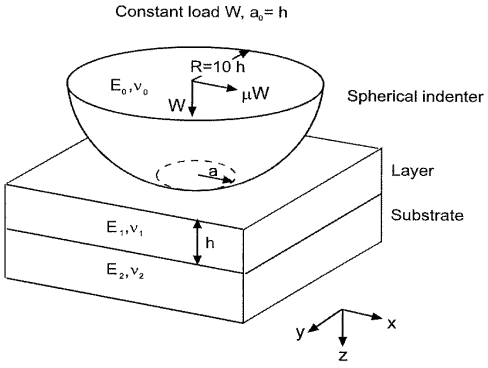

(a)

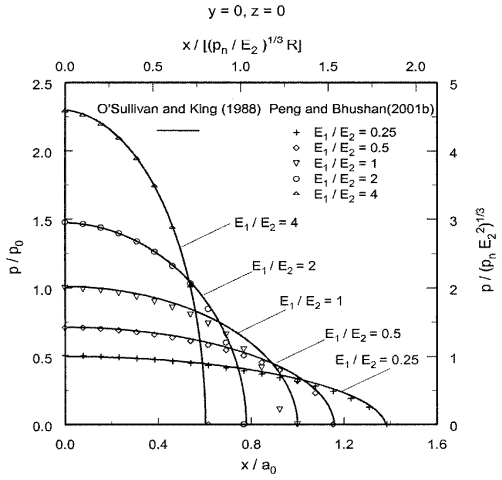

(b)

Figure 2.1. (a) Schematic of a sphere in contact with a layered half-space, and (b) Profile of contact pressures beneath sphere at various *E*1 /*E*2 [O'Sullivan and King, 1988; Peng and Bhushan, 2001].

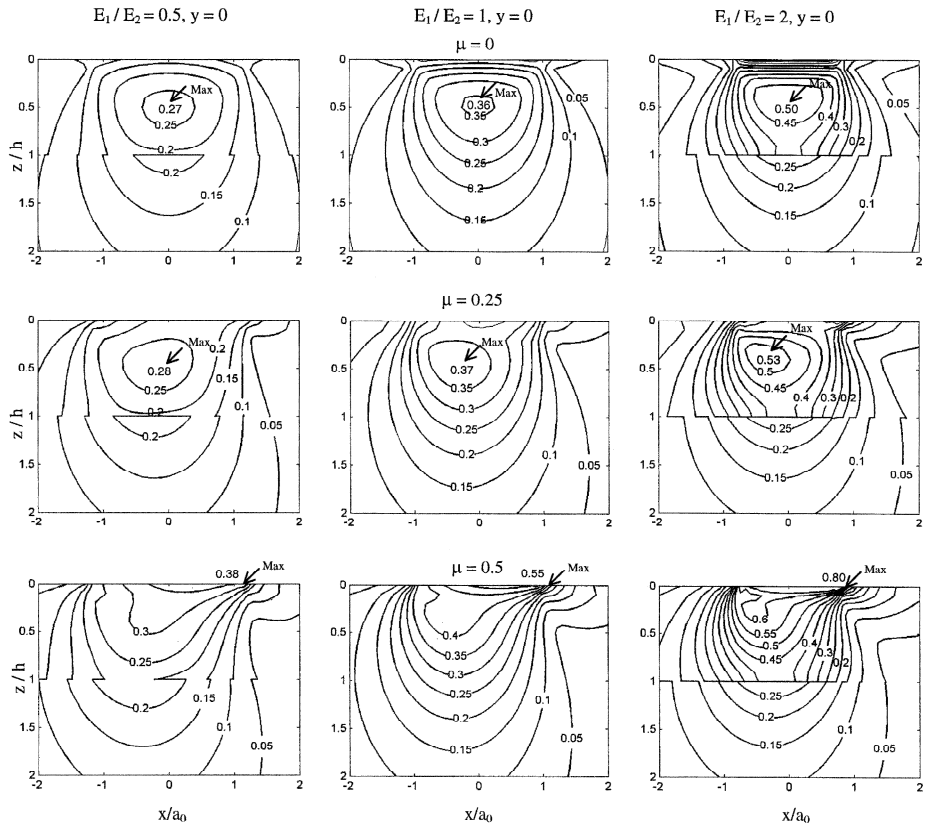

Figure 2.2 Contours of $\sqrt{J_2} / p_0$ at y = 0 at various E1 /E2 and coefficient of friction μ [Peng and Bhushan 2001].

2.1.2. Contact of a rough sphere with a layered surface

Multiple asperities are involved in contact when two rough surfaces are placed together. A comprehensive review of the modeling of the multiple asperity contact of homogenous rough surfaces has been presented by Bhushan (1998). Contact of multiple asperities with a single-layered solid surface has been simulated using either the FEM or BEM approach. For example, FEM was applied by Komvopoulos and Choi (1992) to solve a 2D (plane-strain) homogeneous elastic contact problem with a few cylindrical asperities in contact. Oden and Martin (1985) and Martin et al. (1990) applied FEM to solve a 2D homogenous sliding contact problem with two rough surfaces in contact. Kikuchi and Oden (1988) studied the elastic contact problems with FEM based on variational inequalities. The simulation with BEM is usually associated with using the matrix inversion method (Kannel and Dow, 1985; Merriman and Kannel, 1989; Mao et al., 1996, 1997) or conjugate gradient method (CGM) (Nogi and Kato, 1997; Polonsky and Keer, 1999, 2000a,b); or quasi Newton method (Peng and Bhushan 2001, 2002; Cai and Bhushan, 2005, 2006, 2007a). Though different models differ in detail, e.g., the shape of the asperity, they can be represented by two typical models from the formulation point of view, namely, contact of a rough sphere (some models adopted cylindrical shape) with a flat surface and contact of two rough flat surfaces. The modeling of two rough flat surfaces will be presented in detail in section 2.1.3. For a 3D sphere in contact with a flat surface, the problem can be addressed in a Cartesian coordinate system as (Bhushan and Peng, 2002)

$$u_{z0}(x,y,0)+u_{z1}(x,y,0)=u^{*}_{z0}(x,y,0)+u^{*}_{z1}(x,y,0), \quad (x,y)\in\Omega$$

$$u_{z0}(x,y,0)+u_{z1}(x,y,0)>u^{*}_{z0}(x,y,0)+u^{*}_{z1}(x,y,0), \quad (x,y)\notin\Omega$$

$$p(x,y)\geq 0, \quad (x,y)\in\Omega$$

$$p(x,y)=0, \quad (x,y)\notin\Omega \tag{2.4}$$

where Ω is the real contact domain p(x,y), and $u_z(x,y,0)$ must also satisfy the governing formulation of elasticity. If the real contact domain Ω and corresponding prescribed surface displacement u_z^* are given in the initial condition as in single asperity contact, the problem is readily solved, and the same results are obtained with all formulations. However, in general, prescribing Ω and u_z^* is impossible in multiple asperity contact due to the geometrically complicated interface. Instead, a normal load W or the relative approach δ is prescribed in the initial contact condition. The real contact domain Ω therefore has a many-to-one implicit relationship with the given initial contact condition. The problem becomes ill-defined, and the solution uniqueness is not guaranteed unless supplementary criteria are provided. FEM and BEM approaches with a certain method such as variational principle, conjugate gradient method (CGM), and quasi Newton method, are usually adopted to solve the problem.

Models for the contact of a rough sphere with a layered flat surface have been developed to study the contact pressure and stress distributions, for example by Nogi and Kato (1997) who performed a 3D normal contact analysis of a rigid rough sphere (spherical indentation) on an elastic layered half-space with a CGM-based purely elastic model. The indenter is defined by superposing a smooth sphere with a nominally flat rough surface, whose surface profile is shown in the top of Fig. 2.3a. The layer and substrate's properties are set as G_1 = 100 GPa, G_2 = 79.2 GPa, E_1 = 4.11 GPa, and E_2 = 0.929 GPa, i.e., a stiffer and harder layer. The layer thickness h = 6 μm, and the applied normal load W = 14.7 N. The calculated contact pressures and the surface displacements are shown in the middle and the bottom of Fig. 2.3a, respectively. The contact pressures and surface displacement differ considerably from those calculated by the smooth body theory, although the surface deformation is essentially Hertzian at the macroscopic scale. The maximum pressure is 6.37 times the Hertzian (smooth, homogeneous case) maximum value. Fig. 2.3b shows contour plots of $\sqrt{J_2}$ in the half-space beneath the spherical indenter. The surface pressures associated with asperity contacts produce highly stressed zones where the maximum $\sqrt{J_2}$ is very close to the surface. At greater depths z,

the influence of surface roughness decreases. According to the von Mises criterion, plastic yielding of materials initiates when the maximum value of $\sqrt{J_2}$ is equal to the shear strength of the material. Hence, the surface with material having a shear strength significantly higher than the substrate will help to reduce plastic yield in the contacting body. A comparison of the non-layered case (top of Fig. 2.3b) with stiffer-layered cases (bottom of Fig. 2.3b) shows that the influence of the layer on the subsurface stress states is little because the shear modulus of the layer is not much larger than the substrate (G_1 /G_2 = 1.263). However, the plastic yielding is considerably reduced because E_1 /E_2 = 4.423, thus the von Mises stresses in the layer can rise to a maximum approximately 4.4 times larger than the substrate.

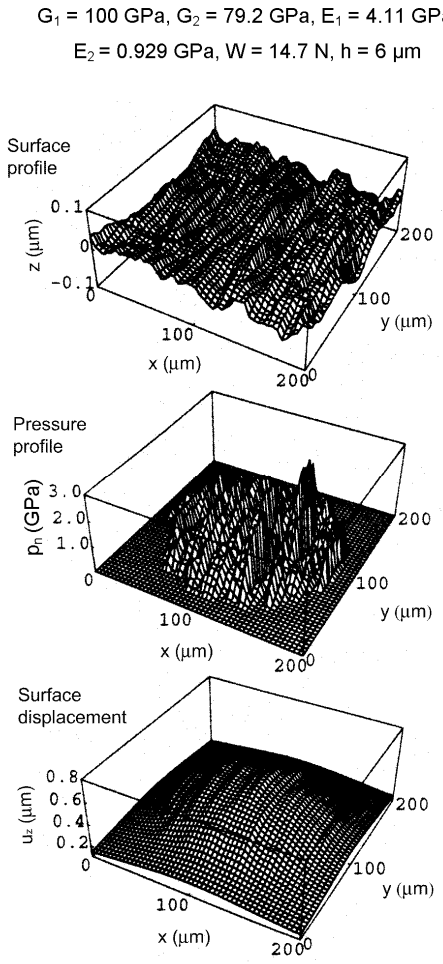

(a)

Fig. 2.3 (a)Profiles of a rough sphere with R = 0.0137 mm, and corresponding contact pressures and z-direction surface displacements at the contact interface, and (b) contours of von Mises stresses (in GPa) on x-z plane through the center of the rough sphere in a homogenous halfspace (top), and a layered half-space (bottom) [Nogi and Kato,1997]

Figure 2.3 (continued)

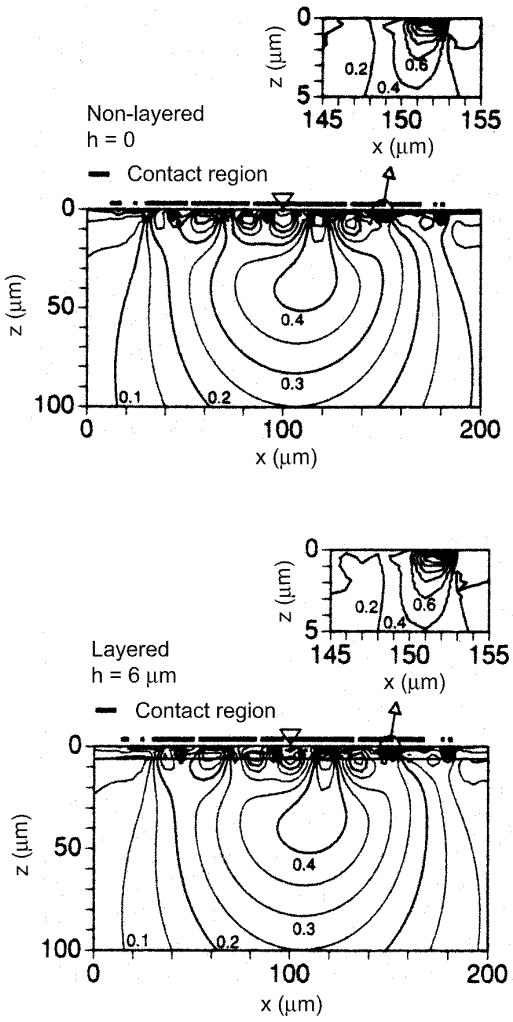

(b)

2.1.3. Contact of multilayered rough flat surfaces

A schematic of multiple asperity contact of a rough, multilayered rough surface in contact with another surface is shown in Fig. 2.4a. Top view of contact regions is shown schematically in Fig. 2.4b. Based on the variational principle, an algorithm is developed to find the minimum value of the total complementary potential energy of the multilayered rough elastic and elastic-perfectly plastic layered solid surfaces in contact. The influence coefficients matrix which describes the applied pressure-displacement and applied pressure-stress relations in a layered solid is derived and substituted into the total complementary potential energy equation, and the minimum value problem is solved in terms of contact pressure. The real area of contact is the sum of all areas with positive contact pressure.

The model focuses on thin layers with thicknesses comparable with or less than the radius of contact. The real area of contact is considered a small fraction of the surface areas of the contacting solids. Therefore, it is assumed that the asperity contacts occur on an elastic half space. The radius of individual contact is assumed much smaller than the radii of curvature of contacting asperities. This makes use of the linear theory of elasticity as well as the approximation of the plane surface around the real area of contact feasible. The applied forces are assumed to act normally to the surfaces. The layers are fully bonded without slipping or partial lifting. The adhesive forces are assumed to be negligible, no tension is allowed in the contact domain, and the pressure is positive in the contact domain. The two contacting rough surfaces are considered as a composite surface. The height of the composite rough surface is the sum of the heights of the two original surfaces, which reduces the contact of two rough surfaces to a smooth flat surface in contact with a composite rough surface (Bhushan and Peng, 2002).

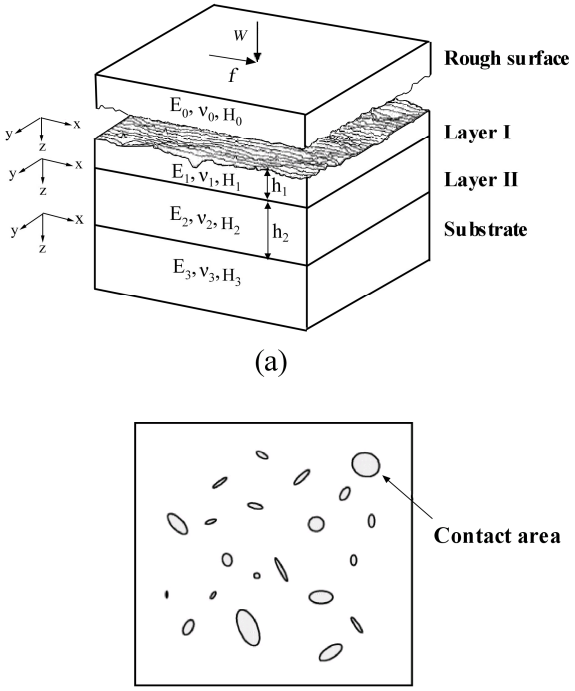

Figure 2.4. Schematics of (a) 3D profiles of two rough surfaces in contact with one with two layers, and (b) top view of contact regions.

2.1.3.1. Modeling of elastic contact

The multilayered rough contact model involves two parts of numerical modeling, namely, layered structure and rough surface generation. For a solid with multiple layers, the contact pressure on the surface is solved by using variational principle with boundary element method (BEM), and the stresses on the surface and subsurface are derived using Papkovich–Neuber potentials. The rough surfaces used in this study are generated using random representative and two-dimensional digital filter techniques.

2.1.3.1.1 Variational principle

Variational methods have been applied to non-Hertzian contact problems for two reasons: to establish conditions that determine the shape and size of the real area of contact and the contact stresses uniquely and to enable well developed techniques of optimization, such as quadratic programming, to be used in numerical solutions (Johnson, 1985; Tian and Bhushan, 1996; Peng and Bhushan, 2001). Two minimum energy principles – minimum total elastic energy and the minimum total complementary potential energy principles – can be used to formulate the elastic contact problems (Richards, 1997). The minimum total complementary potential energy principle is used in this paper since it is more convenient to work in terms of the contact pressure (Kalker and van Randen, 1972). It states that, of all possible equilibrium stress fields for a solid subjected to prescribed loadings and boundary displacements, the true stress field corresponds to a compatible strain field which renders the total complementary energy stationary. For a rough surface contact, when the pressure distribution and the real area of contact are unknown, the problem then becomes to find the minimum value of an integral that equals the total complementary potential energy of the contacting system. For a contact problem of two elastic rough surfaces, the total complementary potential energy V^* is given by (Richards, 1997)

$$V^* = U_E^* - \int_\Omega p\left(u_{z0}^* + u_{z1}^*\right)d\Omega = U_E^* - \int_\Omega p u_z^* d\Omega\,, \tag{2.5}$$

where U_E^* is the internal complementary energy of the two stressed solids, Ω is the assumed domain of the contact surface on which the contact pressures act, p is the contact pressure, u_{zi}^* (i = 0, 1) is the prescribed displacements of the two contacting solids, and u_z^* is the total prescribed displacement of the two contacting solids inside the assumed contact zone. The displacement can be determined by the geometrical interference. Since no tension force is allowed in the contact zone, the real area of contact will lie within in the assumed contact zone.

The definitions of strain energy and complementary energy are shown in Fig. 6a. For linear elastic materials, the internal complementary energy U_E* is numerically equal to the elastic strain energy U_E (as shown in Fig. 6b) which is expressed as

$$U_E = \frac{1}{2}\int_\Omega p(u_{z0} + u_{z1})d\Omega = \int_\Omega p\bar{u}_z d\Omega, \tag{2.6}$$

where $\bar{u}_z$ is the composite surface displacement inside the contact zone, which equals to the total contact deformation of two contacting solids. The complementary potential energy then is given by

$$V^* = \frac{1}{2}\int_\Omega p\bar{u}_z d\Omega - \int_\Omega p\bar{u}_z^* d\Omega. \tag{2.7}$$

In order to perform numerical analysis, the contacting surfaces must be discretized. The simplest representation of multiple asperity contact is an array of concentrated point contacts. The difficulty with this approximation is that the infinite surface displacement occurs at the point of application of a concentrated force. This difficulty is avoided if multiple asperity contact is represented by an array of contacts of squares (patches) of equal size with uniform pressure distributions, which gives rise to a stepwise distribution and the surface displacements being finite everywhere. In the present model, the continuous contact is replaced by a discrete set of patch elements as

shown in Fig. 2.6a. Inside each patch, a piecewise-linear contact pressure distribution may be built up by the superposition of overlapping triangular pressure elements, which produce smooth and continuous surface displacements (Johnson, 1985). However, the multiple asperity contact can be simulated by the patch contact if the patch size is small enough, which makes the superposition unnecessary. Comparison of the current sampling schema with and without piecewise-linear interpolation shows little difference in the result. The contact is then replaced by a discrete set of patch contacts with the boundary conditions satisfied at a finite number of patch centers — the ‘‘matching points.’’ Eq. (2.7) is then discretized to

$$V^* = \frac{1}{2}\sum_{k=1}^{M} p_k \bar{u}_{zk} - \sum_{k=1}^{M} p_k \bar{u}^*_{zk} , \tag{2.8}$$

where the index k represents the surface displacement location, and $\bar{u}_{zk}$ denotes the corresponding surface displacement. The determination of the total prescribed displacement of the two contacting solids u_z^* is shown in Fig. 2.7. Fig. 2.7a shows the geometrical interference area and real area of contact in the normal contact of two identical spheres, and Fig. 2.7b shows the determination of the total prescribed z direction surface displacement u_z^* from geometrical interference. In Eq. (2.8), M is the total number of initial assumed contact points and $M \in N^2$.

To relate $\bar{u}_{zk}$ to the pressures p_l (l=1,2, . . . ,M), the influence coefficient C_{lk} is required and developed in the following section, which expresses the displacement at point k due to uniform pressure centered at a general point l as shown in Fig. 2.6a. The total displacement at k is then expressed by

$$\bar{u}_{zk} = \sum_{k=1}^{M} C_{lk} p_l . \tag{2.9}$$

Substituting $\overline{u}_{zk}$ in Eq. (2.8), the contact problem of finding a minimum value of the total complementary potential energy now reduces to solving the minimum value problem of the integral in terms of contact pressure as follows:

$$V^* = \frac{1}{2}\sum_{k=1}^{M} p_k \sum_{l}^{M} C_{kl}^{u_z} p_l - \sum_{k=1}^{M} p_k \overline{u}_{zk}^* \,. \tag{2.10}$$

The total prescribed displacement of the two contacting solids $\overline{u}_{zk}^*$ in Eq. (2.10) can be determined using the following geometrical interference criteria:

$$\begin{aligned} &\overline{u}_{zk}^* + f_z(x_k, y_k) - \delta^{'} = 0\,, \text{ (within real area of contact)} \\ &\overline{u}_{zk}^* + f_z(x_k, y_k) - \delta^{'} > 0\,, \text{ (outside real area of contact)} \end{aligned} \tag{2.11}$$

where $\delta^{'}$ is the rigid solid movement under applied load and $f_z(x_k, y_k)$ is the initial separation of the two contact surfaces at k,

$$f_z(x_k, y_k) = \left| z_0(x_k, y_k) - z_1(x_k, y_k) \right|. \tag{2,12}$$

Here we assume there is no contact between the two surfaces at the initial position, i.e., $z_0(x_k, y_k) \geq z_1(x_k, y_k)$; thus within the real area of contact, the total prescribed displacement of the two contacting solids will be

$$\overline{u}_{zk}^* = \delta^{'} - \left[z_0(x_k, y_k) - z_1(x_k, y_k) \right]. \tag{2.13}$$

An example is shown in Fig. 2.7 for two identical spheres in contact.

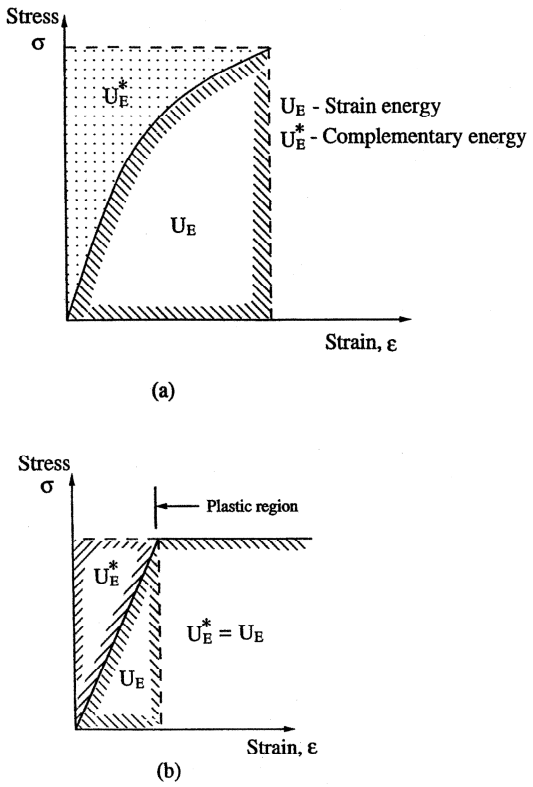

Figure 2.5. (a) Definition of strain energy and complementary energy, (b) relationship between elastic strain energy and internal complementary energy for a linear elastic or a linear elastic-perfectly plastic material.

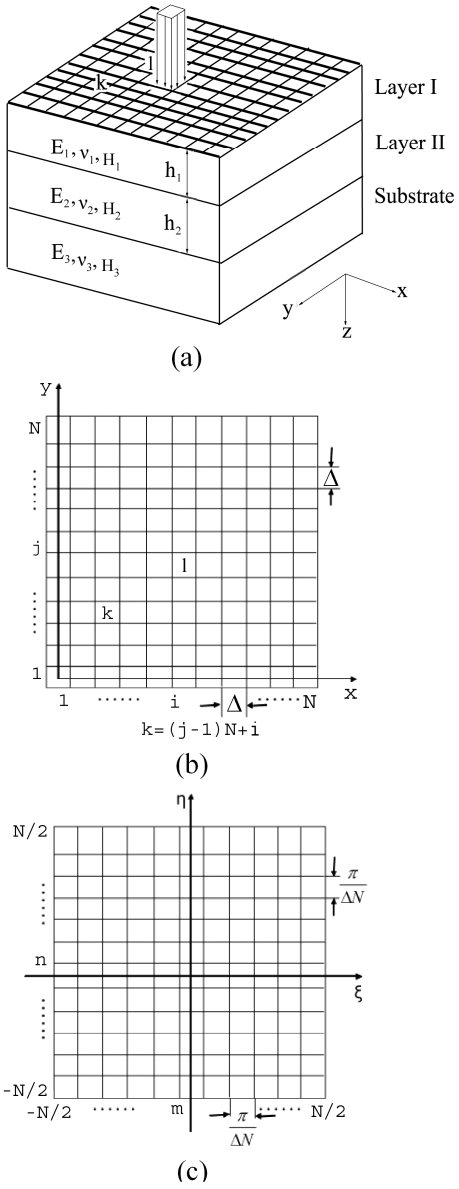

Figure 2.6. Schematics of surface discretization at the contact interface, 3D view (a) in space domain, (b) in space domain, and (c) in frequency domain.

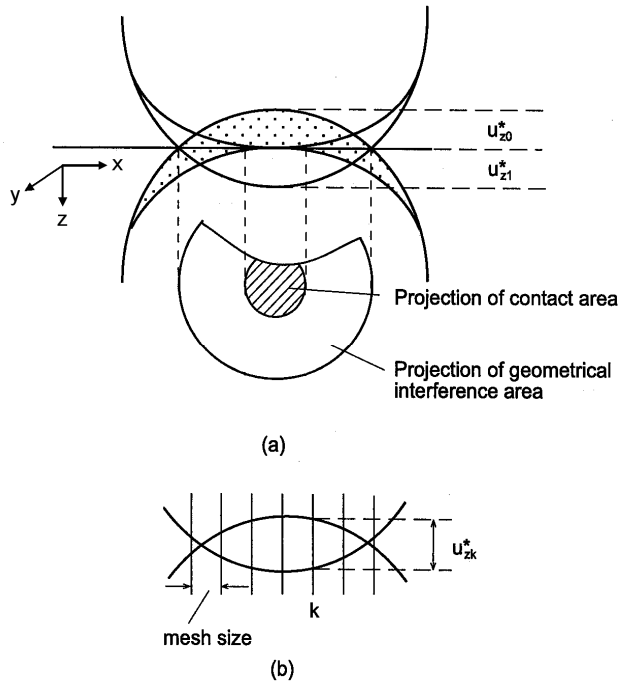

Figure 2.7. (a) Geometrical interference area and real area of contact in the normal contact of two identical spheres, and (b) determination of the total prescribed z-direction surface displacement from geometrical interference.

2.1.3.1.2. Influence coefficients for multilayered solid

Influence coefficient matrices describe the applied pressure-displacement and applied pressure-stress relationships in a layered solid under a unit pressure at one single point. The influence coefficient matrix relating to displacement is needed for solving the pressure using the variational approach described earlier. The matrix relating to stresses is needed to calculate surface and subsurface stress. Given that all the contact pressures p_l *(l = 1…M)* are known, the stresses and displacements at any point k (x_k, y_k, z_k) are expressed as (Bhushan and Peng, 2002)

$$\begin{bmatrix} \sigma_k \\ u_k \end{bmatrix} = \begin{bmatrix} \sum_{l=1}^{M} C_{lk}^{\sigma} p_l \\ \sum_{l=1}^{M} C_{lk}^{u} p_l \end{bmatrix} = \sum_{l=1}^{M} C_{lk} p_l \tag{2.14}$$

where σ and u denote stress and displacement, the influence coefficient matrix C_{lk}^{σ} represents the stresses, and C_{lk}^{u} represents the displacements at point k (x_k, y_k, z_k) induced by a uniform unit pressure enforced at point l (x_l, y_l, 0). C_{lk} represents the combination of C_{lk}^{σ} and C_{lk}^{u}. As shown in Fig. 2.6b, the surface is discretized into small patches with dimension $N \times N$. Here, multiple asperity contact is represented by an array of contacts patches of equal size with uniform normal pressure, which give rise to a stepwise distribution and the surface displacements are finite everywhere. By performing the Fourier transform, matrix products in the space domain (Fig. 2.6b) reduce to simple point-to-point products in the frequency domain (Fig. 2.6c). In order to reduce the computation time, the influence matrix is derived and calculated in the frequency domain and then transformed to the space domain. The discretized form of influence coefficients resulting from the normal contact pressure in the frequency domain is (Bhushan and Peng, 2002)

$$\tilde{C}(\xi,\eta,z)=\Delta^2\sum_{i=0}^{N}\sum_{j=0}^{N}e^{i\left(\xi\ x_i+\eta\ y_j\right)}C\left(x_i,y_j,z\right) \tag{2.15}$$

and the corresponding form in the space domain is obtained by inverting its Fourier transform

$$C(x,y,z)=\frac{1}{\Delta^2N^2}\sum_{m=-\frac{N}{2}+1}^{N/2}\sum_{n=-\frac{N}{2}+1}^{N/2}e^{-i(\xi_m x+\eta_n y)}\tilde{C}(\xi_m,\eta_n,z) \tag{2.16}$$

where "~" indicates Fourier transformation of the expression and Δ is the mesh size in the space domain (Fig. 2.6b).

For a solid with multiple layers, the influence coefficients are developed by using Papkovich–Neuber potentials φ and $\psi(\psi_1,\psi_2,\psi_3)$. These potentials are harmonic functions of *x*, *y*, and *z* for zero body force in space domain. The number of independent 3D harmonic functions can be reduced to three by arbitrarily choosing one of ψ_1,ψ_2,ψ_3 to zero (Malvern, 1969), which is feasible here and does not lose generality (Sokolnikoff, 1956). In order to speed up the computational efficiency, fast Fourier transform (FFT) is applied. In terms of these harmonic functions, the stresses and displacement expressions with FFT for a multilayered solid can be defined as (Peng and Bhushan, 2001, Cai and Bhushan, 2005)

$$\begin{cases}\tilde{u}_i^{(k)}=F\left\{\dfrac{1}{2G}\left[\varphi_{,i}^{(k)}+x\psi_{1,i}^{(k)}+z\psi_{3,i}^{(k)}-\left(3-4\nu\right)\psi_i^{(k)}\right]\right\}\\ \tilde{\sigma}_{ij}^{(k)}=F\left\{\varphi_{,ij}^{(k)}-2\nu\left(\psi_{1,1}^{(k)}+\psi_{3,3}^{(k)}\right)\delta_{ij}^{'}-\left(1-2\nu\right)\left(\psi_{i,j}^{(k)}-\psi_{j,i}^{(k)}\right)+x\psi_{1,ij}^{(k)}+z\psi_{3,ij}^{(k)}\right\}\end{cases} \tag{2.17}$$

where the operator *F* denotes fast Fourier transform, *G* is the shear modulus, the indices *i* and j range over 1,2,3 corresponding to the coordinates *x, y* and *z* in the frequency

domain, k is the layer indices, and $\delta_{ij}^{'}$ is the Kronecker delta. The potentials in Eq. (2.17) in the frequency domain are given by

$$\begin{aligned}
\tilde{\varphi}^{(k)} &= A^{(k)} e^{-\alpha z_k} + \overline{A}^{(k)} e^{\alpha z_k} \\
\tilde{\psi}_1{}^{(k)} &= B^{(k)} e^{-\alpha z_k} + \overline{B}^{(k)} e^{\alpha z_k} \\
\tilde{\psi}_3{}^{(k)} &= C^{(k)} e^{-\alpha z_k} + \overline{C}^{(k)} e^{\alpha z_k}
\end{aligned} \tag{2.18}$$

where α is the distance of a point to the center of the patch where the load is applied in the frequency domain. The influence coefficient matrices $\tilde{C}_{lk}^{\sigma}$ and $\tilde{C}_{lk}^{u}$ are constructed with $\tilde{u}_i^{(k)}$ and $\tilde{\sigma}_{ij}^{(k)}$, respectively. A, B, and C are coefficients of the harmonic functions. The influence coefficients can be obtained by substituting Eq. (2.18) into Eq. (2.17) and performing FFT. For a solid with multiple layers, the displacements in the normal direction are (Cai and Bhushan, 2005)

$$\begin{aligned}
\tilde{u}_{\xi\xi}^{(k)} = \frac{1}{2G_k}\Big[& i\xi\left(A^{(k)}e^{-\alpha z} + \overline{A}^{(k)}e^{\alpha z}\right) - 4(1-\nu_k)\left(B^{(k)}e^{-\alpha z} + \overline{B}^{(k)}e^{\alpha z}\right) + \xi^2 z\alpha^{-1}\left(B^{(k)}e^{-\alpha z} - \overline{B}^{(k)}e^{\alpha z}\right) \\
& + iz\xi\left(C^{(k)}e^{-\alpha z} + \overline{C}^{(k)}e^{\alpha z}\right) - \xi\left(B_{,1}^{(k)}e^{-\alpha z} + \overline{B}_{,1}^{(k)}e^{\alpha z}\right)\Big]
\end{aligned}$$

$$\begin{aligned}
\tilde{u}_{\eta\eta}^{(k)} = \frac{1}{2G_k}\Big[& i\eta\left(A^{(k)}e^{-\alpha z} + \overline{A}^{(k)}e^{\alpha z}\right) - \xi\eta z\alpha^{-1}\left(B^{(k)}e^{-\alpha z} - \overline{B}^{(k)}e^{\alpha z}\right) + i\eta z\left(C^{(k)}e^{-\alpha z} + \overline{C}^{(k)}e^{\alpha z}\right) \\
& - \eta\left(B_{,1}^{(k)}e^{-\alpha z} + \overline{B}_{,1}^{(k)}e^{\alpha z}\right)\Big]
\end{aligned}$$

$$\begin{aligned}
\tilde{u}_{zz}^{(k)} = \frac{1}{2G_k}\Big[& -\alpha\left(A^{(k)}e^{-\alpha z} - \overline{A}^{(k)}e^{\alpha z}\right) - iz\xi\left(B^{(k)}e^{-\alpha z} + \overline{B}^{(k)}e^{\alpha z}\right) - i\xi\alpha^{-1}\left(B^{(k)}e^{-\alpha z} - \overline{B}^{(k)}e^{\alpha z}\right) \\
& - (3-4\nu_k)\left(C^{(k)}e^{-\alpha z} + \overline{C}^{(k)}e^{\alpha z}\right) - z\alpha\left(C^{(k)}e^{-\alpha z} - \overline{C}^{(k)}e^{\alpha z}\right) + i\alpha\left(-B_{,1}^{(k)}e^{-\alpha z} + \overline{B}_{,1}^{(k)}e^{\alpha z}\right)\Big]
\end{aligned} \tag{2.19}$$

and the stresses are

$$\tilde{\sigma}_{\xi\xi}^{(k)} = -\xi^2\left(A^{(k)}e^{-\alpha z} + \overline{A}^{(k)}e^{\alpha z}\right) - i2\left(\nu_k - 2\right)\xi\left(B^{(k)}e^{-\alpha z} + \overline{B}^{(k)}e^{\alpha z}\right) + i\xi^3 z\alpha^{-1}\left(B^{(k)}e^{-\alpha z} - \overline{B}^{(k)}e^{\alpha z}\right)$$
$$+ 2\alpha\nu_k\left(C^{(k)}e^{-\alpha z} - \overline{C}^{(k)}e^{\alpha z}\right) - z\xi^2\left(C^{(k)}e^{-\alpha z} + \overline{C}^{(k)}e^{\alpha z}\right) - i\xi^2\left(B_{,1}^{(k)}e^{-\alpha z} + \overline{B}_{,1}^{(k)}e^{\alpha z}\right)$$

$$\tilde{\sigma}_{\eta\eta}^{(k)} = -\eta^2\left(A^{(k)}e^{-\alpha z} + \overline{A}^{(k)}e^{\alpha z}\right) - i2\nu_k\xi\left(B^{(k)}e^{-\alpha z} + \overline{B}^{(k)}e^{\alpha z}\right) + iz\eta^3\xi\alpha^{-1}\left(B^{(k)}e^{-\alpha z} - \overline{B}^{(k)}e^{\alpha z}\right)$$
$$+ \left(2\alpha\nu_k - z\eta^2\right)C^{(k)}e^{-\alpha z} - \left(2\alpha\nu_k + z\eta^2\right)\overline{C}^{(k)}e^{\alpha z} - i\eta^2\left(B_{,1}^{(k)}e^{-\alpha z} + \overline{B}_{,1}^{(k)}e^{\alpha z}\right)$$

$$\tilde{\sigma}_{zz}^{(k)} = \alpha^2\left(A^{(k)}e^{-\alpha z} + \overline{A}^{(k)}e^{\alpha z}\right) + i2\left(1-\nu_k\right)\xi\left(B^{(k)}e^{-\alpha z} + \overline{B}^{(k)}e^{\alpha z}\right) - iz\alpha\xi\left(B^{(k)}e^{-\alpha z} - \overline{B}^{(k)}e^{\alpha z}\right)$$
$$+ z\alpha^2\left(C^{(k)}e^{-\alpha z} + \overline{C}^{(k)}e^{\alpha z}\right) + 2\left(1-\nu_k\right)\alpha\left(C^{(k)}e^{-\alpha z} - \overline{C}^{(k)}e^{\alpha z}\right) - i\alpha^2\left(B_{,1}^{(k)}e^{-\alpha z} + \overline{B}_{,1}^{(k)}e^{\alpha z}\right)$$

$$\tilde{\sigma}_{\xi\eta}^{(k)} = -\xi\eta\left(A^{(k)}e^{-\alpha z} + \overline{A}^{(k)}e^{\alpha z}\right) - i2\eta\left(1-\nu_k\right)\xi\left(B^{(k)}e^{-\alpha z} + \overline{B}^{(k)}e^{\alpha z}\right) + i\xi^2\eta z\alpha^{-1}\left(B^{(k)}e^{-\alpha z} - \overline{B}^{(k)}e^{\alpha z}\right)$$
$$- z\xi\eta\left(C^{(k)}e^{-\alpha z} + \overline{C}^{(k)}e^{\alpha z}\right) - i\xi\eta\left(B_{,1}^{(k)}e^{-\alpha z} + \overline{B}_{,1}^{(k)}e^{\alpha z}\right)$$

$$\tilde{\sigma}_{z\eta}^{(k)} = -\alpha\eta\left(A^{(k)}e^{-\alpha z} - \overline{A}^{(k)}e^{\alpha z}\right) + \left(\alpha^{-1} - z\right)\xi\eta B^{(k)}e^{-\alpha z} - \left(\alpha^{-1} + z\right)\xi\eta\overline{B}^{(k)}e^{\alpha z}$$
$$- i\eta\left(1-2\nu_k\right)\left(C^{(k)}e^{-\alpha z} + \overline{C}^{(k)}e^{\alpha z}\right) - iz\alpha\eta\left(C^{(k)}e^{-\alpha z} - \overline{C}^{(k)}e^{\alpha z}\right) + \alpha\eta\left(B_{,1}^{(k)}e^{-\alpha z} - \overline{B}_{,1}^{(k)}e^{\alpha z}\right)$$

$$\tilde{\sigma}_{z\xi}^{(k)} = -\alpha\xi\left(A^{(k)}e^{-\alpha z} - \overline{A}^{(k)}e^{\alpha z}\right) - \xi^2 z\left(B^{(k)}e^{-\alpha z} + \overline{B}^{(k)}e^{\alpha z}\right) + \left[2\alpha\left(1-\nu_k\right) + \xi^2\alpha^{-1}\right]$$
$$\left(B^{(k)}e^{-\alpha z} - \overline{B}^{(k)}e^{\alpha z}\right) - i\xi\left(1-2\nu_k\right)\left(C^{(k)}e^{-\alpha z} + \overline{C}^{(k)}e^{\alpha z}\right) - iz\alpha\xi\left(C^{(k)}e^{-\alpha z} - \overline{C}^{(k)}e^{\alpha z}\right)$$
$$+ \alpha\xi\left(B_{,1}^{(k)}e^{-\alpha z} - \overline{B}_{,1}^{(k)}e^{\alpha z}\right)$$

(2.20)

where G_k and ν_k are the shear modulus and Poison ratio for the k^{th} layer. For a given Young's modulus E_k

$$G_k = \frac{E_k}{2(1+\nu_k)} \tag{2.21}$$

There are unknown coefficients A, B and C, $6k+3$ in total, in Eq. (2.19) and (2.20) that need to be further calculated for a solid with k layers. For a two-layered, frictionless contact model, the coefficients B are zeros and thus the total number of unknown coefficients is 10, the number of unknowns is 15 for frictional model. These coefficients can be calculated by applying the boundary conditions as shown below.

Given that the normal pressure is a delta function (δ), the friction force is $\mu\delta$. Here, the coefficient of friction is a static coefficient of friction since there is no real relative motion. For a two-layered solid, indices k in Eq. (2.19) and (2.20) range from 1 to 3. 1 and 2 refer to the first and second layer, and 3 refers to the substrate. The boundary conditions on the surface are given by

$$\sigma_{zz}^{(1)}(x, y, 0) = p_n(x, y, 0) = \delta$$

$$\sigma_{xz}^{(1)}(x, y, 0) = \mu\delta$$

$$\sigma_{yz}^{(1)}(x, y, 0) = 0 \tag{2.22}$$

since the interfaces between layers (or the layer and the substrate) have continuous displacements and stresses. At the interfaces of the layers, the boundary conditions are given by

$$
\begin{aligned}
u_{xx}^{(k)}(x, y, h_k) &= u_{xx}^{(k+1)}(x, y, 0) \\
u_{yy}^{(k)}(x, y, h_k) &= u_{yy}^{(k+1)}(x, y, 0) \\
u_{zz}^{(k)}(x, y, h_k) &= u_{zz}^{(k+1)}(x, y, 0) \\
\sigma_{xz}^{(k)}(x, y, h_k) &= \sigma_{xz}^{(k+1)}(x, y, 0) \\
\sigma_{yz}^{(k)}(x, y, h_k) &= \sigma_{yz}^{(k+1)}(x, y, 0) \\
\sigma_{zz}^{(k)}(x, y, h_k) &= \sigma_{zz}^{(k+1)}(x, y, 0)
\end{aligned}
\tag{2.23}
$$

where the superscript *k* refers to layers. The subscripts *xx*, *yy* and *zz* denote the normal directions, and *xy*, *xz* and *yz* represent shear directions in the Cartesian coordinate system (Cai and Bhushan, 2005 and 2007a).

The 15 unknown potential coefficients A, B, and C in Eq. (2.19) and (2.20) can be calculated by applying these boundary conditions. We notice the potential coefficients $B^{(1)}, \overline{B}^{(1)}, B^{(2)}, \overline{B}^{(2)}$ and $B^{(3)}$ are all zero for a frictionless contact model but nonzero for a frictional contact model. The Bs need to be calculated and substituted into the equations with boundary conditions to further calculate A and C. The five B can be determined by

$$
\begin{bmatrix}
2\alpha(1-\nu_1) & 2\alpha(\nu_1-1) & 0 & 0 & 0 \\
-4(1-\nu_1)e^{-\alpha h_1}/G_1 & -4(1-\nu_1)e^{\alpha h_1}/G_1 & 4(1-\nu_2)/G_2 & 4(1-\nu_2)/G_2 & 0 \\
2\alpha(1-\nu_1)e^{-\alpha h_1} & -2\alpha(1-\nu_1)e^{-\alpha h_1} & -2\alpha(1-\nu_2) & 2\alpha(1-\nu_2) & 0 \\
0 & 0 & -4(1-\nu_2)e^{-\alpha h_2}/G_2 & -4(1-\nu_2)e^{\alpha h_2}/G_2 & 4(1-\nu_2)/G_3 \\
0 & 0 & 2\alpha(1-\nu_2)e^{-\alpha h_2} & -2\alpha(1-\nu_2)e^{\alpha h_2} & -2\alpha(1-\nu_3)
\end{bmatrix}
\begin{bmatrix}
B^{(1)} \\ \overline{B}^{(1)} \\ B^{(2)} \\ \overline{B}^{(2)} \\ B^{(3)}
\end{bmatrix}
=
\begin{bmatrix}
\mu\delta \\ 0 \\ 0 \\ 0 \\ 0
\end{bmatrix}
\tag{2.24}
$$

The coefficients $A^{(1)}, \overline{A}^{(1)}, C^{(1)}, \overline{C}^{(1)}$ are determined by

$$
\begin{aligned}
&\alpha A_1 + \alpha\overline{A}_1 + 2(1-\nu_1)C_1 - 2(1-\nu_1)\overline{C}_1 = R_1 \\
&\alpha A_1 - \alpha\overline{A}_1 + (1-\nu_1)C_1 + 2(1-\nu_1)\overline{C}_1 = R_2
\end{aligned}
$$

$$k_{19}A_1 + k_{20}\overline{A}_1 + k_{21}C_1 + k_{22}\overline{C}_1 = R_c$$

$$k_{23}A_1 + k_{24}\overline{A}_1 + k_{25}C_1 + k_{26}\overline{C}_1 = R_d \tag{2.25}$$

And solutions for the other 6 coefficients $A^{(2)}$, $\overline{A}^{(2)}$, $C^{(2)}$, $\overline{C}^{(2)}$, $A^{(3)}$, and $C^{(3)}$ are

$$A_2 = \frac{1}{2}\left[(\frac{1}{G_{12}} + k_5)A_1 e^{-\alpha h_1} + (\frac{1}{G_{12}} - k_5)\overline{A}_1 e^{\alpha h_1} + (\frac{h_1}{G_{12}} + k_6)C_1 e^{-\alpha h_1} + (\frac{h_1}{G_{12}} + k_7)\overline{C}_1 e^{\alpha h_1} - \frac{1}{G_2}R_3 + k_8 \right] \tag{2.26}$$

$$\overline{A}_2 = \frac{1}{2}\left[(\frac{1}{G_{12}} - k_5)A_1 e^{-\alpha h_1} + (\frac{1}{G_{12}} + k_5)\overline{A}_1 e^{\alpha h_1} + (\frac{h_1}{G_{12}} - k_6)C_1 e^{-\alpha h_1} + (\frac{h_1}{G_{12}} - k_7)\overline{C}_1 e^{\alpha h_1} - \frac{1}{G_2}R_3 - k_8 \right] \tag{2.27}$$

$$C_2 = \frac{\alpha}{4(\nu_2 - 1)}\left[2(\frac{1}{G_{12}} - 1)A_1 e^{-\alpha h_1} + (k_1 - k_3)C_1 e^{-\alpha h_1} + (k_2 - k_4)\overline{C}_1 e^{\alpha h_1} - G_2 R_3 + \frac{R_6}{\alpha} - \frac{G_2 R_4 + R_5}{\alpha} \right] \tag{2.28}$$

$$\overline{C}_2 = \frac{\alpha}{4(1 - \nu_2)}\left[2(\frac{1}{G_{12}} - 1)A_1 e^{-\alpha h_1} + (k_1 + k_3)C_1 e^{-\alpha h_1} + (k_2 + k_4)\overline{C}_1 e^{\alpha h_1} - G_2 R_3 + \frac{R_6}{\alpha} + \frac{G_2 R_4 + R_5}{\alpha} \right] \tag{2.29}$$

$$A_3 = \frac{1}{G_{23}}\left[A_2 e^{-\alpha h_2} + \overline{A}_2 e^{\alpha h_{21}} + h_2 (C_2 e^{-\alpha h_2} + \overline{C}_2 e^{\alpha h_2}) \right] - G_3 R_7 \tag{2.30}$$

$$C_3 = k_9 - \frac{2\alpha}{G_{23}(3 - 4\nu_3)}\overline{A}_2 e^{\alpha h_2} + k_{11} C_2 e^{-\alpha h_2} - k_{10}\overline{C}_2 e^{\alpha h_2} \tag{2.31}$$

The intermediate variables *k*s and *R*s are reported in detail in Appendix B.

G_1, G_2, G_3, G_{12}, and G_{23} are

$$G_1 = \frac{E_1}{2(1+\nu_1)}, G_2 = \frac{E_2}{2(1+\nu_2)}, \; G_3 = \frac{E_3}{2(1+\nu_3)} \tag{2.32}$$

$$G_{12} = \frac{G_1}{G_2}, \; G_{23} = \frac{G_2}{G_3} \tag{2.33}$$

where $\alpha = \sqrt{\xi^2 + \eta^2}$, ξ and η are coordinates in the frequency domain, and $\tilde{p}(\xi,\eta,0)$ is the Fourier transformation of $p(x, y,0)$. With the coefficients A, B and C, the displacements in Eq. (2.19) and stresses in Eq. (2.20) are obtained, and $\tilde{C}_{lk}^{\sigma}$ and $\tilde{C}_{lk}^{u}$ can be constructed accordingly. By taking the inverse FFT (IFFT) of $\tilde{C}_{lk}^{\sigma}$ and $\tilde{C}_{lk}^{u}$, the space domain C_{lk}^{σ} and C_{lk}^{u} can be obtained. The influence coefficient matrix C_{lk} in Eq. (2.14) is found by incorporating C_{lk}^{σ} and C_{lk}^{u}.

In order to calculate for the surface contact pressure appearing in those total complementary potential energy formulation equations, the influence coefficient matrix on the surface $\tilde{C}^{u}(\xi_m,\eta_n,0)$ (which represents the surface displacements $u_{zz}(\xi,\eta,0)$ due to uniform pressure centered at each small patch) is needed. The discretized surface influence coefficient matrix can be calculated from Eq. (2.19) by setting $z = 0$ and $k = 1$

$$\tilde{C}^{u}(\xi_m,\eta_n,0) = \frac{1}{2G_1}\left[-\alpha\left(A^{(1)} - \overline{A}^{(1)}\right) - i\xi\alpha^{-1}\left(B^{(1)} - \overline{B}^{(1)}\right) - (3-4\nu_1)\left(C^{(1)} - \overline{C}^{(1)}\right) + i\alpha\left(-B_{,1}^{(1)} + \overline{B}_{,1}^{(1)}\right)\right] \tag{2.34}$$

where $(\xi,\eta,0) \in \Omega$ and the coefficient matrix $\tilde{C}^{u}(\xi_m,\eta_n,0)$ is assumed to be constant except in the neighborhood of the origin where its values changes rapidly. A 64-point Gaussian quadrature integration over the patches near the origin is used to compute the average of $\tilde{C}(\xi_m,\eta_n,0)$ to avoid the singularity.

2.1.3.1.3. Quadratic programming

Eq. (2.10) developed in a previous section can be solved by quadratic programming. Since no tension is allowed at the contact interface, the search for a minimum value of Eq. (2.10) is restricted by

$$p_k \geq 0, \quad k = 1, ..., \mathrm{M}, \tag{2.35}$$

where M is the total number of initially assumed contact points. Before proceeding, it is convenient to write Eq. (2.6) in quadratic form as

$$V^*(\overline{p}) = \frac{1}{2}\overline{p}^T C\overline{p} - \overline{p}^T \overline{u}\,, \tag{2.36}$$

where $\overline{p}^T$ is the transpose vector of contact pressures denoted by

$$\overline{p}^T = (p_1, p_2, ..., p_M), \tag{2.37}$$

and C and $\overline{u}$ are the symmetric influence coefficients matrix and displacement vector, respectively. They are denoted as corresponding to those contact points,

$$C = \begin{bmatrix} C_{11} & C_{12} & \cdots & C_{1M} \\ C_{21} & C_{22} & \cdots & C_{2M} \\ \cdots & \cdots & \cdots & \cdots \\ C_{M1} & C_{M2} & \cdots & C_{MM} \end{bmatrix},$$

and

$$\overline{u}^T = (u^*_{z1}, u^*_{z2}, ...u^*_{zk}, ...u^*_{zM}). \tag{2.38}$$

Now the problem becomes finding the minimum value of Eq. (2.36) — a standard quadratic function of the contact pressure — under the restriction of Eq. (2.35). It can be calculated by a bounded indefinite quadratic programming method, which combines coordinate searches and subspace minimization steps. Many methodologies have been

developed for the homogeneous case. Stanley and Kato (1971) used a simplified steepest descent method to incorporate gradient information to accelerate the minimization procedure. A uniform shift of pressures and truncation of negative pressures was used to satisfy Eq. (2.35) without changing the shape of the pressure distribution. However, the steepest descent method may not, in general, lead to the minimum (Press et al., 1999). Ai and Sawamiphakdi (1999) used the Fletcher–Reeves version of the conjugate gradient method to search for the minimum value and introduced a penalty function to remove the constraints of Eq. (2.35). However, the feasibility of choosing the penalty term was not guaranteed, and an inappropriate choice of the penalty term might produce an incorrect answer. Tian and Bhushan (1996) found the minimum by using Newton's method to search for a zero of the gradient of the quadratic function

$$\nabla V^*(\bar{p}) = C \quad \bar{p}^* - \bar{u} = 0\,, \tag{2.39}$$

which yields $\bar{p}^* = C^{-1}\bar{u}$. The search starts from solving Eq. (2.39) using a Gaussian–Seidel iterative method, and during the iteration, the negative pressures are discarded to satisfy the constraints.

To ensure a solution to move towards a minimum in Newton's method, *C* must be positive definite, which is not generally guaranteed. Also, $\nabla^2 V^*(\bar{p})$ has to be calculated at each iteration. When the dimension of the problem is high and $\nabla^2 V^*(\bar{p})$ is difficult to calculate, the calculation of $\nabla^2 V^*(\bar{p})$ may take considerable computational time. As an extension of Newton's method, Bhushan and Peng (2002) used quasi-Newton's method to obtain the minimum. In quasi-Newton's method, the computation of $\nabla^2 V^*(\bar{p})$ is not needed, and a positive definite, symmetric matrix H_0 to approximate C^{-1} is constructed. A sequence of the approximated matrices H_i are built up in such a way that the matrix remains positive definite and symmetric (Press et al., 1999). Starting from an arbitrary initial point far from the minimum, this method guarantees that the solution always moves in a downhill direction. Close to the minimum, the updating H_i will approach

C^{-1} with the guarantee of quadratic convergence. So, the quasi-Newton's method is also feasible to solve the current multi-asperity and multi-layer contact problem.

It is possible that rounding errors may cause the matrix H_i to become nearly singular or not positive definite. This could be serious because nearly singular H_i tends to give subsequent H_{i+1} that is also nearly singular. A simple test may be performed to check the problem by restarting the algorithm to see if it approaches the claimed minimum point. If it does not, one can use the updated approximate H_i to replace C in Eq. (2.39). Then, instead of solving Eq. (2.39), one solves the set of linear equations in the form

$$H_i \overline{p}^* - \overline{u} = 0. \tag{2.40}$$

A triangular decomposition of H_i is stored instead of H_i itself, and the updating formula can be arranged to guarantee that the matrix remains positive definite and nonsingular, even with finite round off.

2.1.3.2. Modeling of elastic/perfectly plastic contact

In this section, the rough, two-layered surfaces contact model is extended to elastic-plastic contact analysis for the case where an elastic–perfectly plastic deformation occurs at the contacting surfaces. The von Mises yield criterion is generally used to determine the onset of plastic yield. However, the von Mises stresses are the model output and unknown beforehand. An alternative approach applies the theory of indentation hardness and assumes that a contact point deforms plastically once the local contact pressure exceeds the hardness of the softer solid in contact. This assumption generally agrees with the von Mises yield criterion, provided that the contact asperities are very sharp, located far from each other, and therefore strictly independent of each other. This assumption is satisfied for the contact of a nominally flat, rough surface under moderate load. This assumption is invalid for the contact of spherical asperities of large radius. To further simplify the elastic/perfectly-plastic model, the region of plastic

deformation is assumed to be confined within a very small region and therefore does not significantly alter the geometry of the elastically deformed region.

Hardness, which defines the local plastic contact, is needed to conduct elastic-plastic analysis based on the current model. A contact point deforms plastically once the local contact pressure exceeds an effective hardness (H_e). The hardness of the layered solid is known to be independent of the substrate for a maximum displacement (u_{max}) (indentation depth) less than ~ 0.3 of the film thickness, after which the hardness increases or decreases because of the presence of the substrate (Bhushan, 2002). As the indentation depth increases, the effective hardness of the rough, two-layered solid becomes a function of the elastic-plastic properties of layered structure. Based on the application of the contact model, Bhushan and Venkatesan (2005) developed an empirical relationship to calculate the effective hardness of a single layered solid,

$$\frac{H_e}{H_{k+1}} = 1 + \left(\frac{H_k}{H_{k+1}} - 1 \right) \exp\left(- \left(\frac{u_{\max}}{h_k} \right)^m \left(\frac{E_k}{E_{k+1}} \right)^n \left(\frac{H_k}{H_{k+1}} \right)^p \right). \qquad (2.41)$$

Since we deal with a small rectangular patch, we select this analysis of a conical asperity on a flat surface. For a hard layer on a soft substrate, values of *m, n* and *p* are 1.1, -0.5 and 0.1, respectively, and for soft on hard, these are 1.8, -0.9 and 1.0, respectively. *k* is 1 or 2 depending on the criteria described below.

For a solid with two layers, the criteria used for calculating the effective hardness are: (1) the effective hardness is considered to be that of the top layer (H_1) at the maximum displacement $u_{\max} < 0.3h_1$, (2) the effective hardness is calculated based on the hardness of the top layer and the interlayer at the maximum displacement $u_{\max} < 0.3h_2$, and (3) the effective hardness is calculated based on the hardness of the interlayer and the substrate at the maximum displacement $u_{\max} > 0.3h_2$.

2.1.3.3. Validation of the Model

As for the validation of the model, the single asperity contact model for a homogeneous situation was verified by Yu and Bhushan (1996). They first calculated the von Mises stresses for the Hertzian circular contact as well as for a concentrated point load and compared the results with those calculated for loads applied on a patch using their model. It was found that the results are in a good agreement. The single layered model (Peng and Bhushan, 2001) and the multi layered model (Cai and Bhushan, 2005) are the extensions of the homogeneous model. The influence coefficients calculated for the multilayered contact model (Eqs. (19)-(34)) are the same as those calculated by O'Sullivan and King (1988) and Peng and Bhushan (2001) if the number of layers are reduced to a single layer.

2.1.3.4. Rough surface generation

The contact model can handle either measured or computer generated surfaces. The digitized rough surfaces used in the data presented in this thesis to study trends have Gaussian height distributions generated by a computer using random representative and two-dimensional digital filter techniques (Tian and Bhushan, 1996; Bhushan and Peng, 2002). For a Gaussian surface, it is known that a surface can be characterized by standard deviation of surface height σ and correlation length β^* (the measure of how quickly a random event decays) (Bhushan, 1999, 2002). An autocorrelation function (a measure of how well future values of the function can be predicted based on past observations) is used to control the computer generated rough surface. The autocorrelation function for the surface is assumed to be exponential and is given by

$$R_z(k,l) = \sigma^2 \exp\left[-2.3\sqrt{\left(\frac{k}{\beta_x^*}\right)^2 + \left(\frac{l}{\beta_y^*}\right)^2}\right], \tag{2.42}$$

where the correlation lengths of the surface in the x direction and y direction are taken as $\beta_x^* = \beta_y^*$ (isotropic surface). Examples of three rough surfaces simulated are shown in

Fig. 2.8. The parameters for the three surfaces are (1) $\beta^* = \beta_x = \beta_y = 0.5$ μm and surface height deviation σ = 1 nm, (2) $\beta^* = \beta_x = \beta_y = 0.5$ μm and surface height deviation σ = 10 nm, and (3) $\beta^* = \beta_x = \beta_y = 0.05$ μm and surface height deviation σ = 1 nm in a 20 × 20 μm^2 scan window.

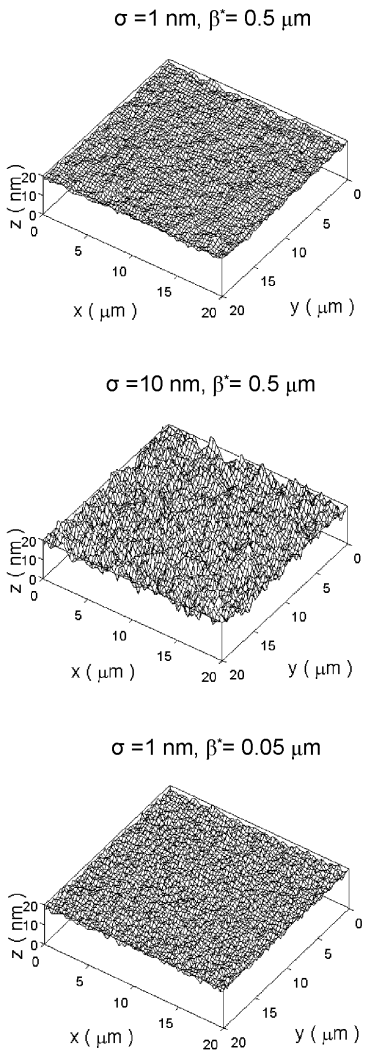

Figure 2.8 Surface height maps of three computer generated rough surfaces [Cai and Bhushan, 2005].

2.1.3.5. Representative results

Two categories of analysis, namely, frictionless and frictional analysis, are reported here (for the purposes of comparison) to show the effect of roughness, stiffness, hardness, layer thickness, load, and coefficient of friction on maximum contact pressure, fractional real area of contact, fractional plastic contact area and maximum displacement. The maximum contact pressure is the maximum one among the local contact pressures acting at the contact points. The real area of contact is the summation of all the contact spots. The plastic contact area is the summation of all the plastic contact spots (a plastic contact spot is the one with local contact pressure equal the hardness at that contact spot). The maximum displacement is the maximum local deformation among all the contact points.

Only normal load is applied for the case of frictionless contact, whereas combined normal load and friction force are applied for the case of frictional contact. In the data presented here to study trends, a rigid surface is brought into contact with rough elastic-perfectly plastic two-layered solid surfaces. Although the model is capable of handling two contacting elastic-plastic surfaces, the upper surface is assumed to be rigid to better interpret the trends in the data. As an example, the physical properties and surface topography statistics for various layers found in a magnetic rigid disk and for a magnetic slider made of Al_2O_3-TiC are listed in Table 2.1. The values selected in the data presented here are representative of head- disk interface. Young's modulus of the substrate E_3 is taken as 100 GPa. The pressure is normalized by E_3. Poisson's ratios are taken as 0.3 for all cases. The hardness of the substrate is taken as $0.05E_3$. The roughness effects are investigated based on three computer generated rough surfaces, (1) $\beta^* = \beta_x = \beta_y = 0.5$ μm and surface height deviation σ = 1 nm, (2) $\beta^* = \beta_x = \beta_y = 0.5$ μm and surface height deviation σ = 10 nm, and (3) $\beta^* = \beta_x = \beta_y = 0.05$ μm and surface height deviation σ = 1 nm in a 20×20 μm^2 scan window as shown in Fig. 2.8. The investigation of stiffness effects are based on various ratios of the Young's moduli of the layers to that of the substrate with fixed hardness. The investigations of hardness effects are based on various ratios of the hardness of the layers to that of the substrate with fixed

Young's modulus. In order to view the effect of layer thickness, two different ratios of the layer thicknesses to the surface height deviation, $h_1 / \sigma = h_2 / \sigma = 1$ and 10, are used. In the study of loading effects, the contact statistics and maximum stresses as a function of applied load is presented. Two specific low and high loads are used as examples to show the stress distributions for elastic contact and elastic-perfectly plastic contact. The load taken is $p_n / E_3 = 4 \times 10^{-6}$ for a pure elastic contact and the high load $p_n / E_3 = 1 \times 10^{-5}$ is used to ensure an elastic/perfectly-plastic contact. The maximum contact pressure, fractional real area of contact, fractional area of plastic contact, and maximum displacement as functions of applied load are also reported. The coefficient of friction μ varies from 0, 0.1, 0.3, to 0.5 for frictional quasi sliding contacts. The calculated stresses are natural log values in kPa.

2.1.3.5.1. Surface roughness effect

Surface roughness affects the maximum contact pressure and real area of contact. Data are also shown in Fig. 2.9 for (1) σ = 1nm, $\beta^* = 0.5$, (2) σ = 10 nm, $\beta^* = 0.5$, and (3) σ = 1 nm, $\beta^* = 0.05$. σ is increased by ten times in the second case, and β^* is decreased by ten times in the third case. It is observed that the number of contact points decreases significantly with surface roughness increase (an increase in σ or decrease in β^*, implying the importance of parameter σ / β^*), while the magnitudes of contact pressures and surface and subsurface stresses grow quickly with surface roughness. The effects of the standard deviation of surface height σ and correlation length β^* on the maximum contact pressure, the fractional real area of contact and the fractional plastic contact area are shown in Fig. 2.10. Fig. 2.10a-c shows the maximum contact pressure, the fractional real area of contact, and the fractional plastic contact area as a function of applied load for three chosen three rough surfaces. The results show that the increase in surface roughness leads to smaller real area of contact with higher local contact pressure. The increase in surface roughness also leads to local plastic contact at the highest asperities at lower load. The increase in the surface height deviation (σ) has greater effect on contact pressure and surface and subsurface stress as compared to the decrease in the

correlation length (β^*). The decrease in β^* results in larger number of contacts with higher real area of contact and lower contact pressure as compared to that of increase in σ. This is because the height difference between the local highest and lowest asperities are much larger for a surface with higher σ, i.e. σ = 10 nm.

The increase of surface roughness leads to a decrease in real area of contact, which is beneficial to minimize friction and stiction. However, the increase in surface roughness causes larger maximum contact pressure, accordingly large surface and subsurface stresses, which are not desirable to improve wear. Also the increase in surface roughness makes local plastic contact occur at a low load which is not desirable for wear since wear is more likely to occur when asperities touch plastically than in pure elastic contact (Bhushan, 2002).

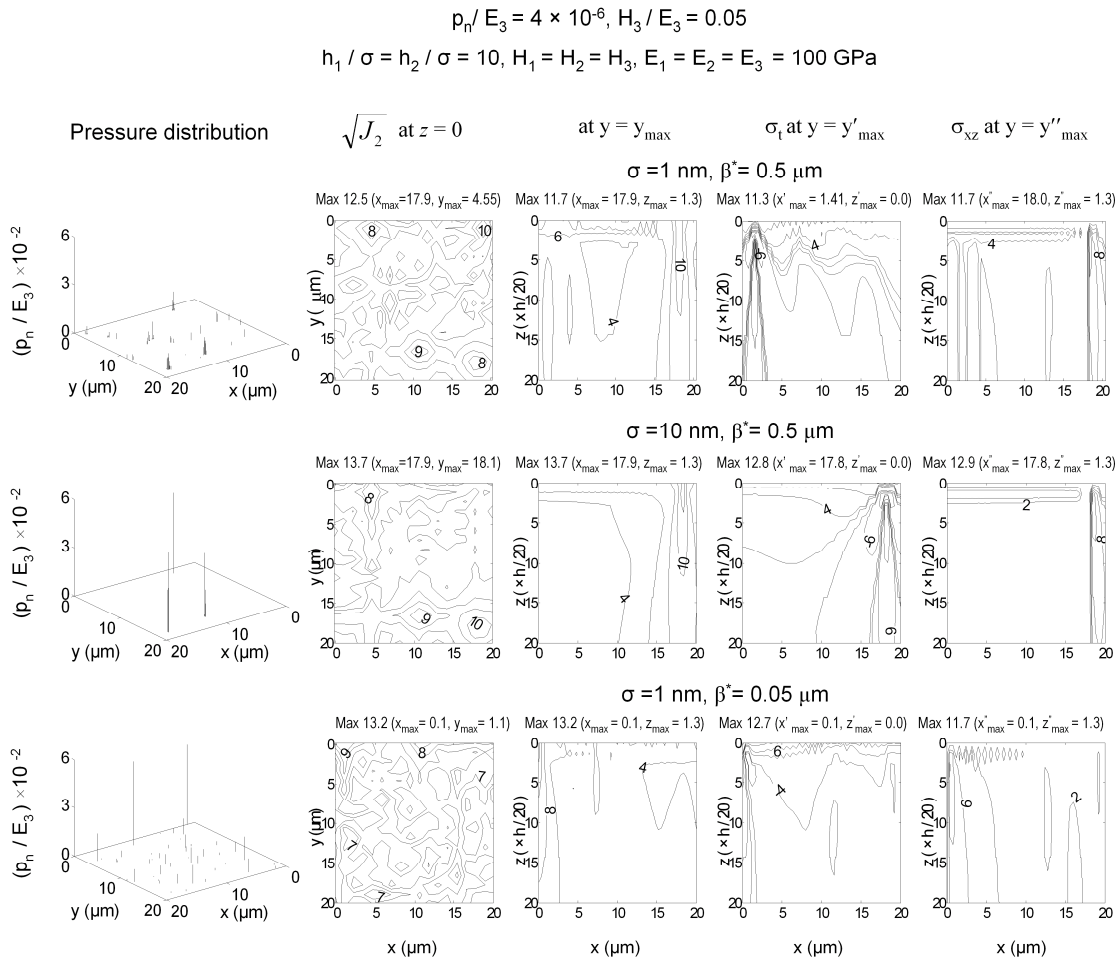

Figure 2.9 Profiles of contact pressures, contours of von Mises stresses on the surface, von Mises stresses on the max $\sqrt{J_2}$ plane, principal tensile stresses on the max σ_t plane and shear stresses on the max σ_{xz} plane with $H_3 / E_3 = 0.05$, $h_1 / \sigma = h_2 / \sigma = 10$, $H_1 = H_2 = H_3$, $E_3 = 100$ GPa, and $\sigma = 1$ nm, $\beta^* = 0.5$ μm; $\sigma = 10$ nm, $\beta^* = 0.5$ μm; and $\sigma = 1$ nm, $\beta^* = 0.05$ μm, $p_n / E_3 = 4 \times 10^{-6}$. The vertical scale representing p_n axis is magnified [Cai and Bhushan, 2005].

2.1.3.5.2. Stiffness effect

For various ratios of the Young's moduli of the layers to that of the substrate, five structures are used to investigate the stiffness effect, I: $E_1 = E_2 = E_3$ (homogeneous solid); II: $E_1 / E_3 = E_2 / E_3 = 0.5$ (single layered solid with a compliant top layer); III: $E_1 / E_3 = E_2 / E_3 = 2$ (single layered solid with a stiff top layer); IV: $E_1 / E_3 = 1$, $E_2 / E_3 = 0.5$ (solid with a compliant interlayer), and V: $E_1 / E_3 = 1$, $E_2 / E_3 = 2$ (solid with a stiff interlayer). Effects of stiffness based on the three different rough surfaces are showed. The rough surface with $\sigma = 1$nm, $\beta^* = 0.5$ is chosen as a example to study the maximum displacement, contact pressure profile and stress distributions for various ratios of the Young's moduli of the layers to that of the substrate.

Figure 2.10a-c shows the maximum contact pressure, the fractional real area of contact, and the fractional plastic contact area as a function of applied load for three chosen rough surfaces. The influence of the layer properties on the stress distribution, maximum contact pressure, fractional real area of contact and fractional plastic contact area can be clearly observed. For the case of $E_1 = E_2 = E_3$ (homogeneous), the trends of real area of contact and pressure change are consistent with that of Peng and Bhushan (2001) for $E_1 = E_2$ of a single layered model. As compared to the homogeneous rough surface case, a rough layered solid with compliant top layers (II) exhibits lower magnitudes of the maximum contact pressure and surface and subsurface stresses but increased number of contact points (real area of contact). A rough layered solid with stiff top layers (III) exhibits higher magnitudes of the maximum contact pressure and surface and subsurface stresses but decreased number of contact points (real area of contact). These observations agree with common engineering experience and those presented by Bhushan and Peng (2002) for a rough, single layered solid surfaces contact model with $E_1 / E_2 = 0.5$ and $E_1 / E_2 = 2$. Given that the top layer and the substrate here have the same mechanical properties and all contacts are elastic, the maximum contact pressure, surface and subsurface stresses decrease, and the real area of contact remains roughly the same when a compliant interlayer (IV) is used, whereas the contact pressure and stresses increase and the real area of contact decreased with a stiff interlayer (V). However, the decrease or increase in magnitude becomes more moderate as compared to the

corresponding single layered model with compliant or stiff layer on the top. The maximum contact pressure, stresses and the real area of contact all decrease with a compliant/stiff interlayer as compared to that of the single layered solid with stiff top layer. It is also observed that plastic contacts are less likely to occur for a solid with compliant top layers, while plastic contacts are likely to occur for a solid with stiff top layers, given the hardness is the same. This occurs because the local maximum contact pressure and surface and subsurface stress are relatively lower for a solid with compliant top layers, but higher for a solid with stiff top layers.

Figure 2.11 shows that the stiffness of the layers and the substrate affects the maximum displacement (local deformation) as well. In the elastic deformation regime, compliant top layers ($E_1 / E_3 = E_2 / E_3 = 0.5$) result in larger maximum local deformation as compared to the other cases, and stiffer top layers ($E_1 / E_3 = E_2 / E_3 = 2$) lead to smaller maximum local deformation as compared to the other cases; the maximum local deformation is a little larger for a compliant interlayer and a little smaller for a stiffer interlayer as compared to the homogeneous case. Since large local deformation may cause local asperities with less height to come in contact, this provides part of the reason why a solid with a compliant top layer has a relatively larger real area of contact and lower contact pressure. The opposite is true for a solid with stiffer top layers.

Figures 2.12a and b show examples of the pressure and stress distributions for various ratios of the Young's moduli of the layers to that of the substrate for the same surface at two different specific loads. As compared to Fig. 13a, Fig. 13b has a larger applied load. The smaller load is for elastic contact, and the larger load is used to ensure elastic/perfectly plastic contact. It is observed that a stiffer top layer or interlayer leads to an increased in maximum stresses, whereas a compliant top layer or interlayer leads to a decrease in maximum stresses. These trends are the same as that observed in Fig. 2.10.

Figure 2.13a shows the pressure and stress distributions for various ratios of the Young's moduli of the layers to that of the substrate. Fig. 2.13b shows the maximum contact pressure, fractional contact area and fractional plastic contact area as functions of applied loads. As compared to Fig. 2.12, a smaller thickness is used in Fig. 2.13 to ensure composite hardness plays a role. The results show a compliant top layer (II) decreases the

maximum local contact pressure and the maximum stresses as compared to a homogeneous solid (I), whereas a stiff top layer (III) has the opposite effects. The maximum contact pressure, and surface/subsurface stresses decrease with a compliant interlayer (IV) as compared to a homogeneous solid (I), whereas the difference in the maximum contact pressure and stresses between using a stiffer interlayer or not is not significant. We also notice the maximum stresses for a solid with compliant interlayer (IV) are comparable to those of the solid with a compliant top layer. Since wear is closely related to the maximum surface/subsurface stresses, a compliant interlayer (IV) has high potential to decrease wear, whereas a stiff interlayer (V) might not have the benefit as compared to the homogeneous solid (I). A solid with a compliant top layer (II) is not advisable to be used. Though it has relatively low maximum contact pressure and stresses as compared to the other solids, it results in a significant increase in the real area of contact which associates with possible high friction. The results show a solid with a compliant interlayer is the most preferable structure to obtain low wear.

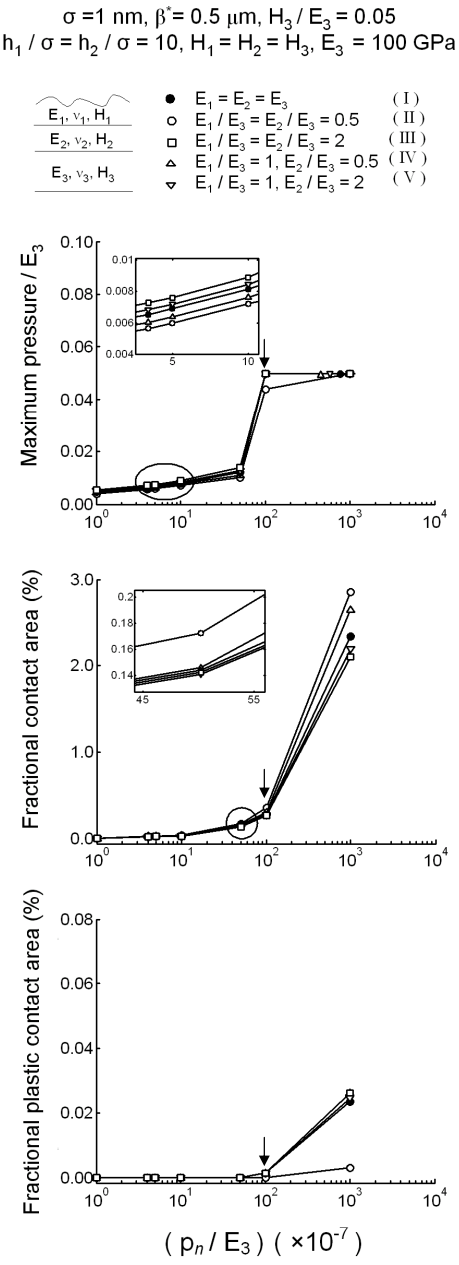

(a)

Figure 2.10 Variation of maximum pressure, and fractional real area of contact with normal pressure p_n for different values of E_1 / E_3, E_2 / E_3, $H_3 / E_3 = 0.05$, $h_1 / \sigma = h_2 / \sigma = 10$, $H_1 = H_2 = H_3$, $E_3 = 100$ GPa, and (a) $\sigma = 1$ nm, $\beta^* = 0.5$ μm, (b) $\sigma = 10$

nm, $\beta^* = 0.5$ μm, and (c) $\sigma = 1$ nm, $\beta^* = 0.05$ μm [Cai and Bhushan, 2005]. The arrows indicate the transition from elastic to elastic-perfectly plastic deformation.

Figure 2.10 (continued)

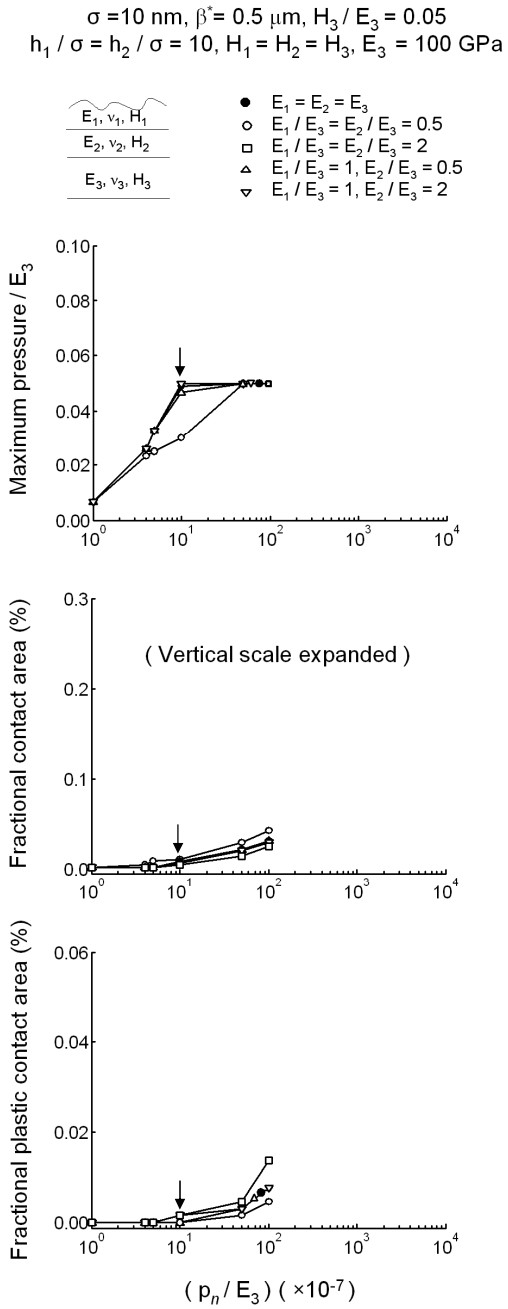

(b)

Figure 2.10 (continued)

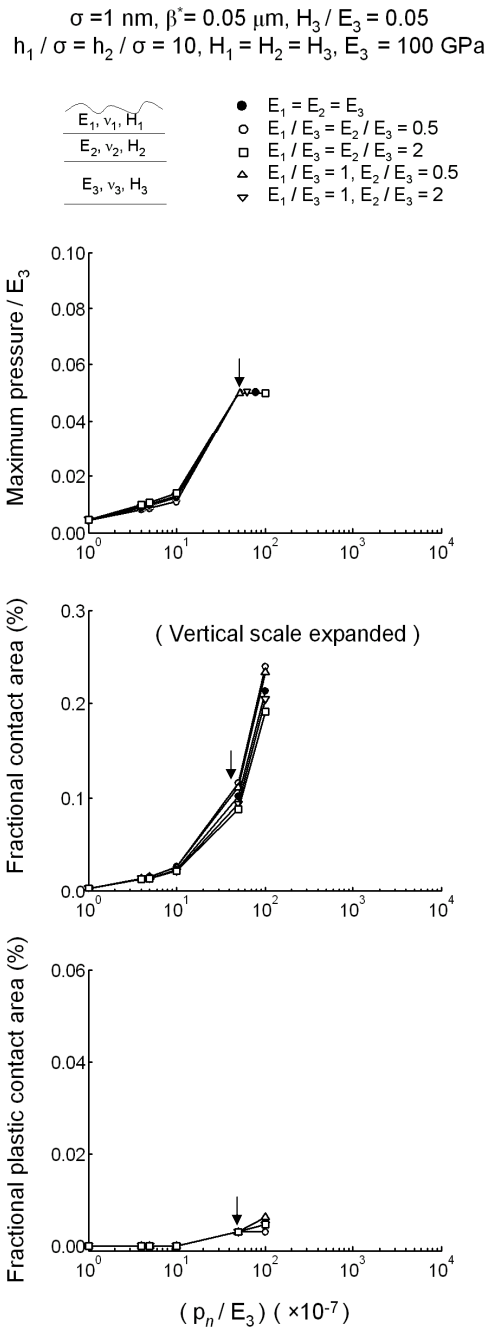

(c)

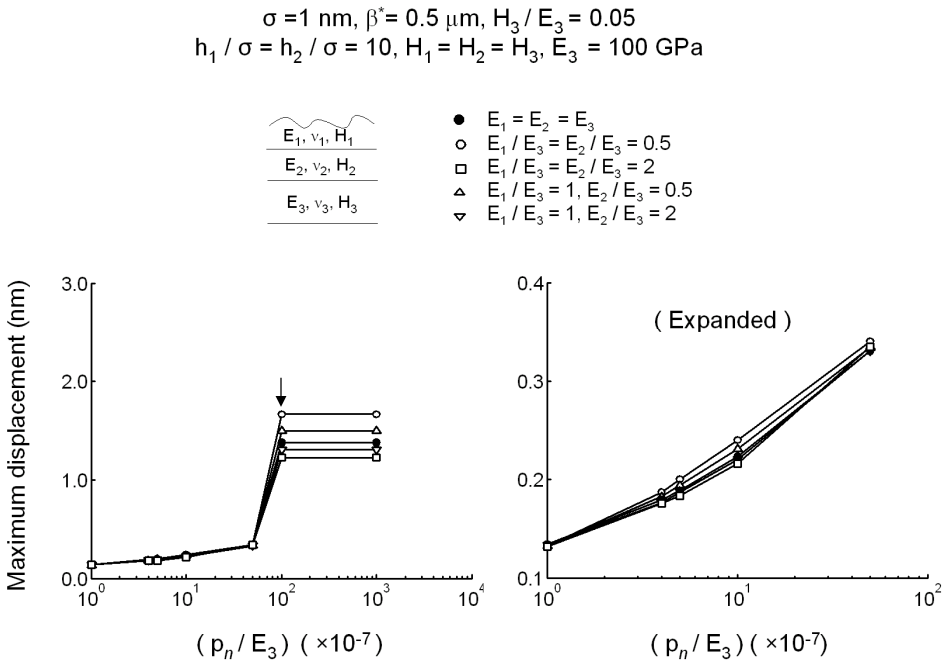

Figure 2.11. Variation of maximum displacement with normal pressure p_n for different values of E_1 / E_3, E_2 / E_3, $\sigma = 1$ nm, $\beta^* = 0.5$ μm, $H_3 / E_3 = 0.05$, $h_1 / \sigma = h_2 / \sigma = 10$, and $H_1 = H_2 = H_3$, $E_3 = 100$ GPa [Cai and Bhushan, 2005]. The arrow in the figure indicates the transition from elastic to elastic-perfectly plastic deformation.

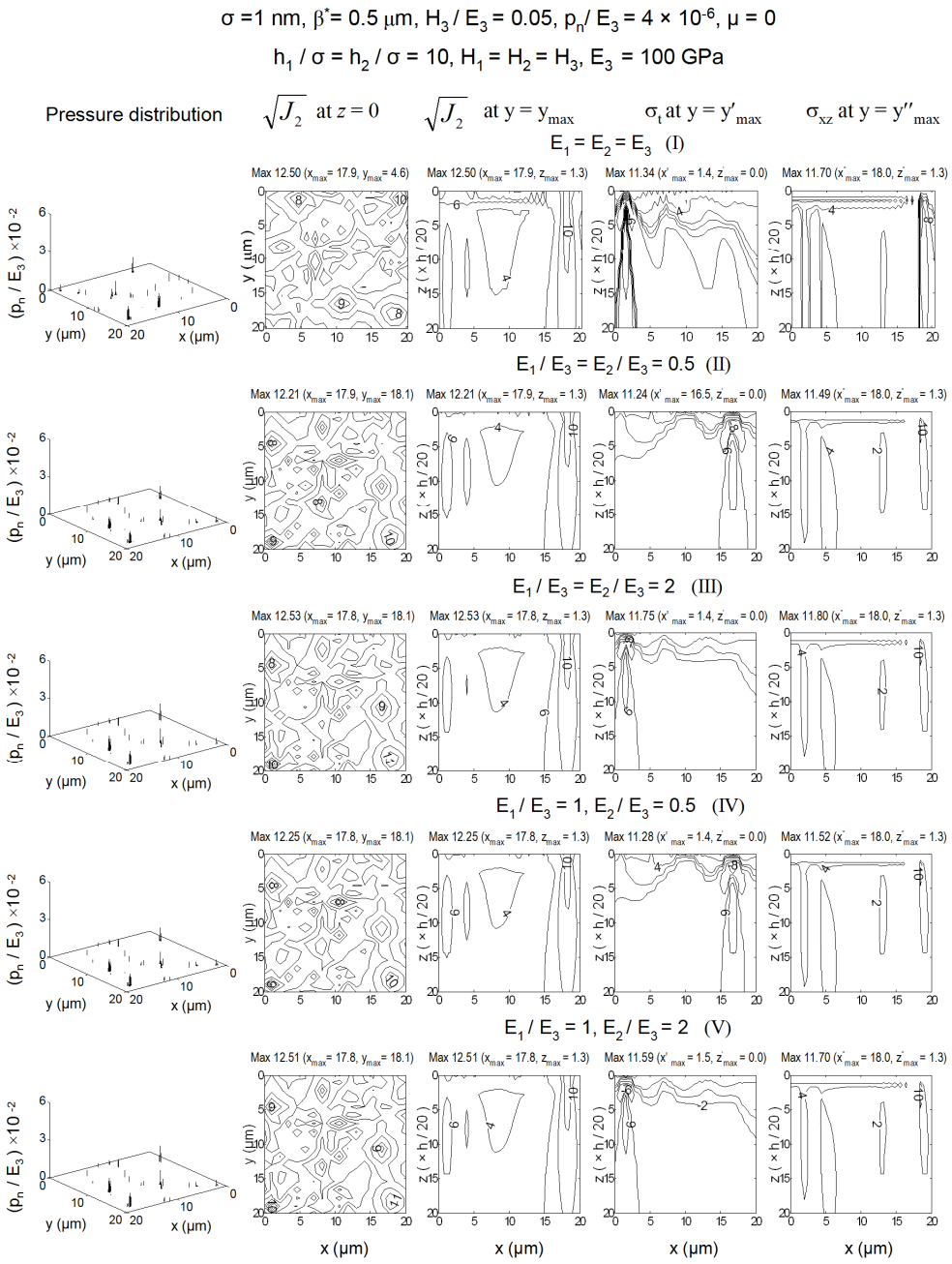

(a)

Figure 2.12. At different values of E_1 / E_3, E_2 / E_3, $\sigma = 1$ nm, $\beta^* = 0.5$ μm, $H_3 / E_3 = 0.05$, $h_1 / \sigma = h_2 / \sigma = 10$, $H_1 = H_2 = H_3$, $E_3 = 100$ GPa, and $\mu = 0$, profiles of contact pressures, contours of von Mises stresses on the surface, von Mises stresses on the max $\sqrt{J_2}$ plane, principal tensile stresses on the max σ_t plane and shear stresses

on the max σ_{xz} plane for (a) $p_n / E_3 = 4\times10^{-6}$, and (b) $p_n / E_3 = 4\times10^{-5}$ [Cai and Bhushan, 2006, 2007a].

Figure 2.12 (continued)

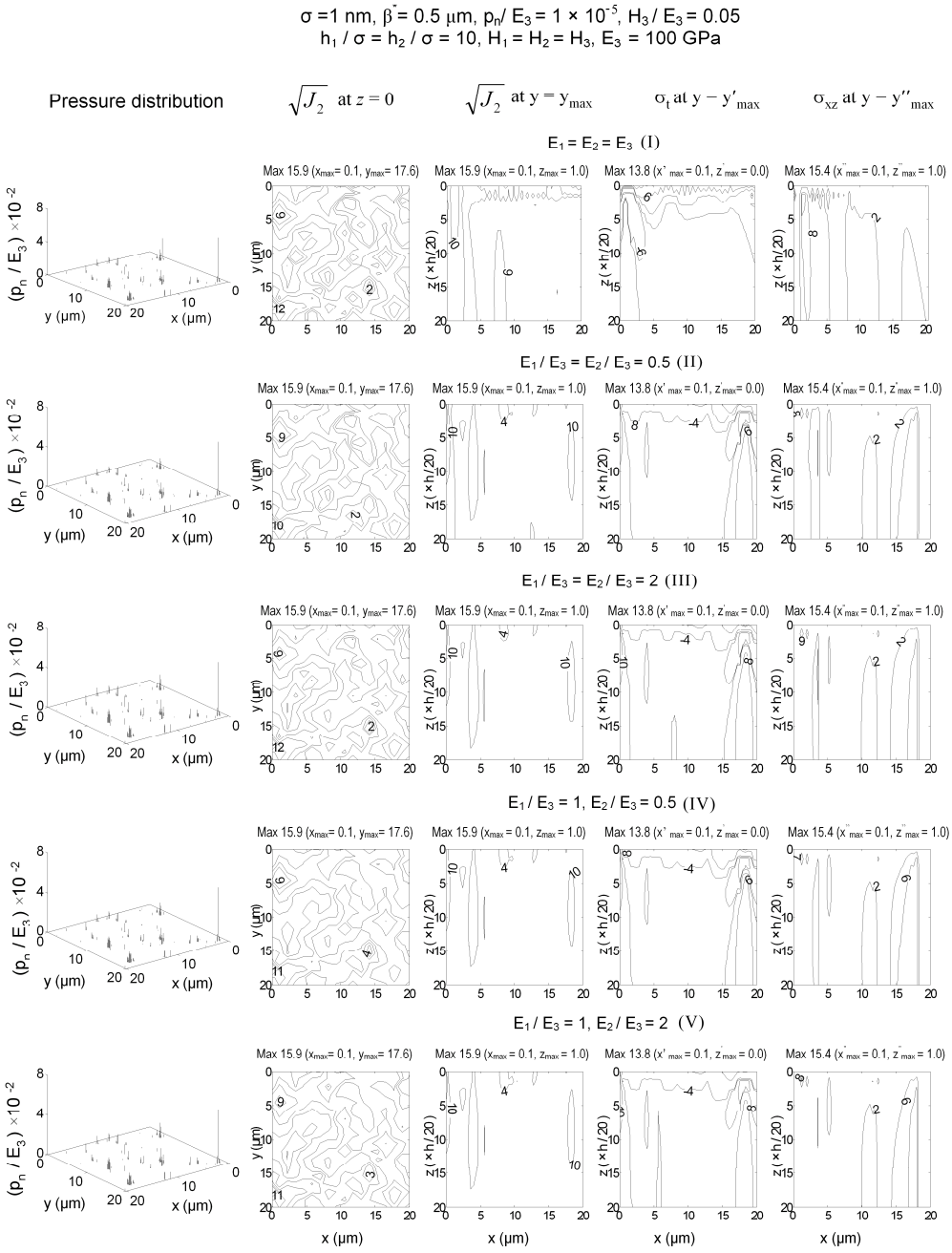

(b)

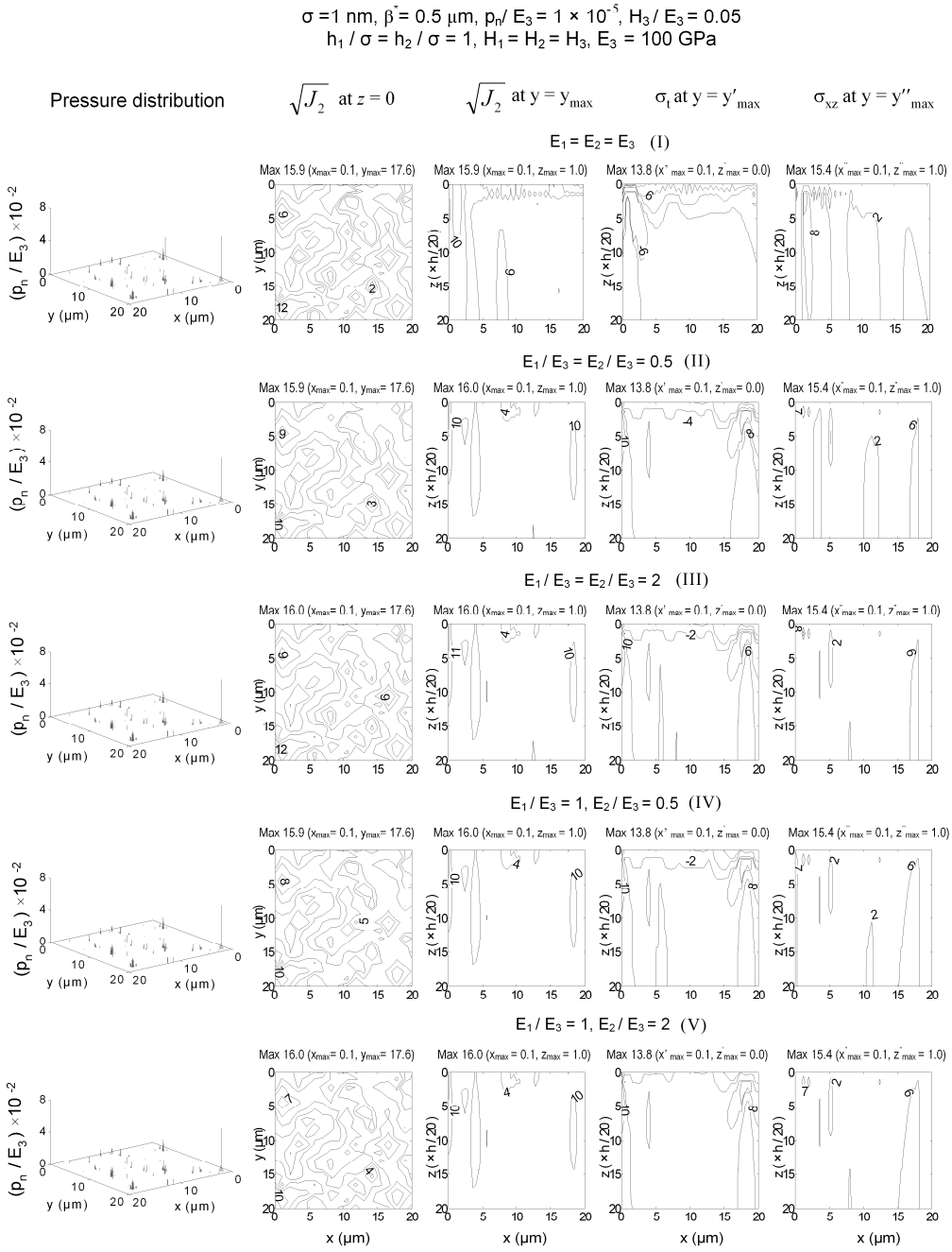

(a)

Figure 2.13. At different values of E_1 / E_3, E_2 / E_3, $\sigma = 1$ nm, $\beta^* = 0.5$ μm, $H_3 / E_3 = 0.05$, $h_1 / \sigma = h_2 / \sigma = 1$, $H_1 = H_2 = H_3$, $E_3 = 100$ GPa, (a) profiles of contact pressures, contours of von Mises stresses on the surface, von Mises stresses on the max $\sqrt{J_2}$ plane, principal tensile stresses on the max σ_t plane, and shear stresses on the

max σ_{xz} plane with $p_n / E_3 = 1\times10^{-5}$, and (b) variation of maximum pressure, fractional real area of contact, and fractional plastic area of contact with normal pressure p_n [Cai and Bhushan, 2006]. The arrows in (b) indicate the transition from elastic to elastic-perfectly plastic deformation.

Figure 2.13 (continued)

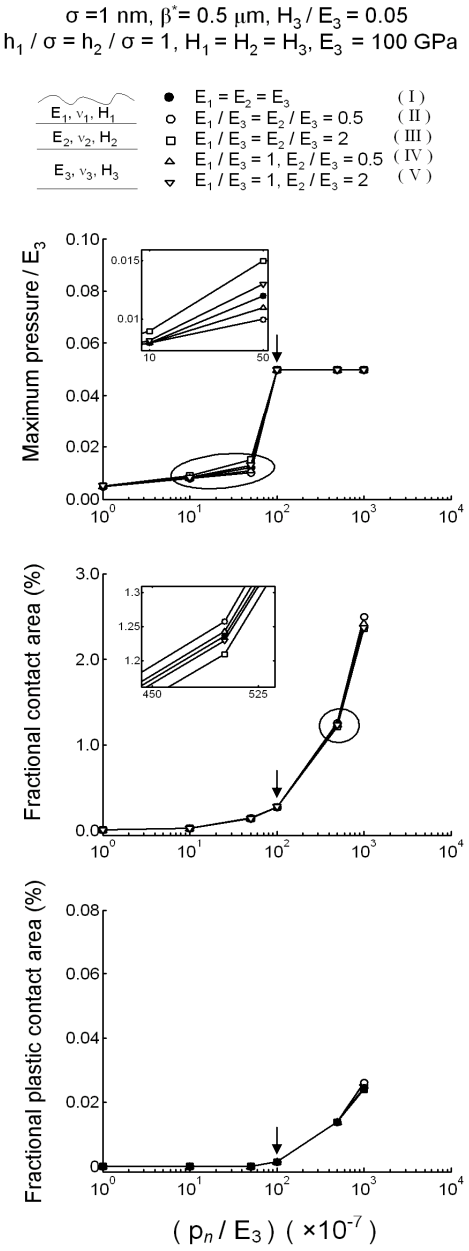

(b)

2.1.3.5.3 Hardness effect

For elastic-perfectly plastic contact, a plastic contact occurs at the point the local contact pressure exceeds the hardness of the softer solid in contact. The hardness affects on contact statistics and stresses after local plastic contact occurs (Cai and Bhushan, 2006). An effective hardness (H_e) defined in section 2.1.3.2 is calculated and used to check the possible occurrence of plastic contact at each local contact point at every iteration of the simulation in the multilayer multi-asperity contact model. The analyses for homogeneous and layered solids with layer thickness $h_1 / \sigma = h_2 / \sigma = 1$ is reported here to investigate the hardness effect. All the layered solids involve five structures, I': $H_1 = H_2 = H_3$ (homogeneous solid); II': $H_1 / H_3 = H_2 / H_3 = 0.5$ (single layered solid with a softer top layer); III': $H_1 / H_3 = H_2 / H_3 = 2$ (single layered solid with a harder top layer); IV': $H_1 / H_3 = 1$, $H_2 / H_3 = 0.5$ (solid with a soft interlayer), and V': $H_1 / H_3 = 1$, $H_2 / H_3 = 2$ (solid with a hard interlayer).

Figure 2.14a shows the pressure and stress distributions, and Fig. 2.14b shows the maximum contact pressure, fractional real area of contact and fractional plastic contact area as a function of applied load for three homogeneous solids, $H_1/ E_3 = H_2 / E_3 = H_3 / E_3 = 0.05$, 0.025 and 0.1. It is observed that the critical contact pressure (transition to plastic contact) increases with hardness. The hardness plays a role when local plastic contact occurs. The surface with lower hardness reaches plastic deformation at lower loads, and the spread (increase) of plastic contact area is much faster.

The hardness of the layered solid is known to be independent of the substrate for an indentation depth of less than 0.3 of the film thickness, after which the hardness increases or decreases because of the presence of the substrate (Bhushan, 2002). An effective hardness (H_e) begins to play a role (elastic-plastic regime) when the criteria discussed in section 2.3.1.2 are met. A smaller thickness $h_1 / \sigma = h_2 / \sigma = 1$ is used to further investigate the effective hardness effect for multilayered solids. The effective hardness plays a role in the elastic-plastic regime.

Figure 2.15a shows the maximum displacement as a function of applied load. Fig. 2.15b shows the pressure profile and stress distributions. Fig. 2.15c shows the maximum contact pressure, fractional real area of contact and fractional plastic contact area as a

function of applied load for the five structures. The hardness of the layers and the substrate affect maximum local deformation, as shown in Fig. 2.15a. In the elastic-perfectly plastic regime, a soft top layer (II') results in smaller maximum local deformation as compared to the other structures, and a hard top layer (III') leads to larger maximum local deformation; the maximum local deformation is smaller for a soft interlayer (IV') as compared to the homogeneous solid (I'), and vice versa. For these five structures, the maximum contact pressure differs from each other when the local displacement meets a certain criterion, whereas the differences between the real areas of contact for these structures are small since the plastic contact area is only a small portion as compared to the total area of contact. In the elastic-plastic regime, the maximum contact pressure can be higher, lower or equal to the top layer's hardness for elastic-perfectly plastic contact. Its magnitude depends on the layer properties. A rough layered solid with softer top layers (II') exhibits a lower magnitude of the maximum contact pressure and surface/subsurface stresses but increases the number of contact points (real area of contact) as compared to a homogeneous solid (I'), and vice versa. The maximum contact pressure, and surface/subsurface stresses decrease and the real area of contact increases with a softer interlayer (IV') as compared to a homogeneous solid (I'). Opposite effects are observed for a solid with a harder interlayer (V'). Plastic contact occurs when the local contact pressure is larger than the corresponding effective hardness. It is observed that plastic contacts are less likely to occur for a solid with a harder top layer (III') than a homogeneous solid (I'). Opposite effects are observed for structure (II'). This happens because low effective hardness is easier to surmount for a solid with softer top layers, but harder to surmount for a solid with harder top layers.

The trends are similar to those of the stiffness effects. Plastic contact occurs when the local contact pressure is larger than the corresponding effective hardness. A soft top layer (II') decreases the maximum contact pressure, and surface/subsurface stresses but increases the real area of contact, and vice versa. This occurs because more numbers of contact points are needed for a solid with a smaller effective hardness to balance the external applied load. Plastic contacts are likely to occur for a solid with a soft top layer (II'

) at low loads. This may increase wear and, therefore, is not desirable. A higher hardness may be chosen in order to improve wear properties.

The important findings of the stiffness and hardness are summarized in Table 2.2. The suggestions are made based on the comparison of the layered solid to the homogeneous solid. The stiffness effect shows that a more compliant interlayer leads to lower maximum contact pressure, and surface/subsurface stresses which are preferable to decrease wear. A solid with a more compliant top layer is not advisable since it results in a significant increase in real area of contact which associates with high friction. The hardness effects exhibit similar trends as the stiffness effects. The effective hardness plays a role in the elastic-plastic regime. The maximum contact pressure can be higher, lower or equal to the top layer's hardness for elastic-perfectly plastic contact. Its magnitude depends on the layer properties. It is not advisable to use a softer top layer since plastic contact is easier to occur (with the increase of applied load) which leads high wear. It is observed that no plastic contact occurs for a solid with a harder top layer. A higher hardness may be chosen in order to increase the resistance to wear.

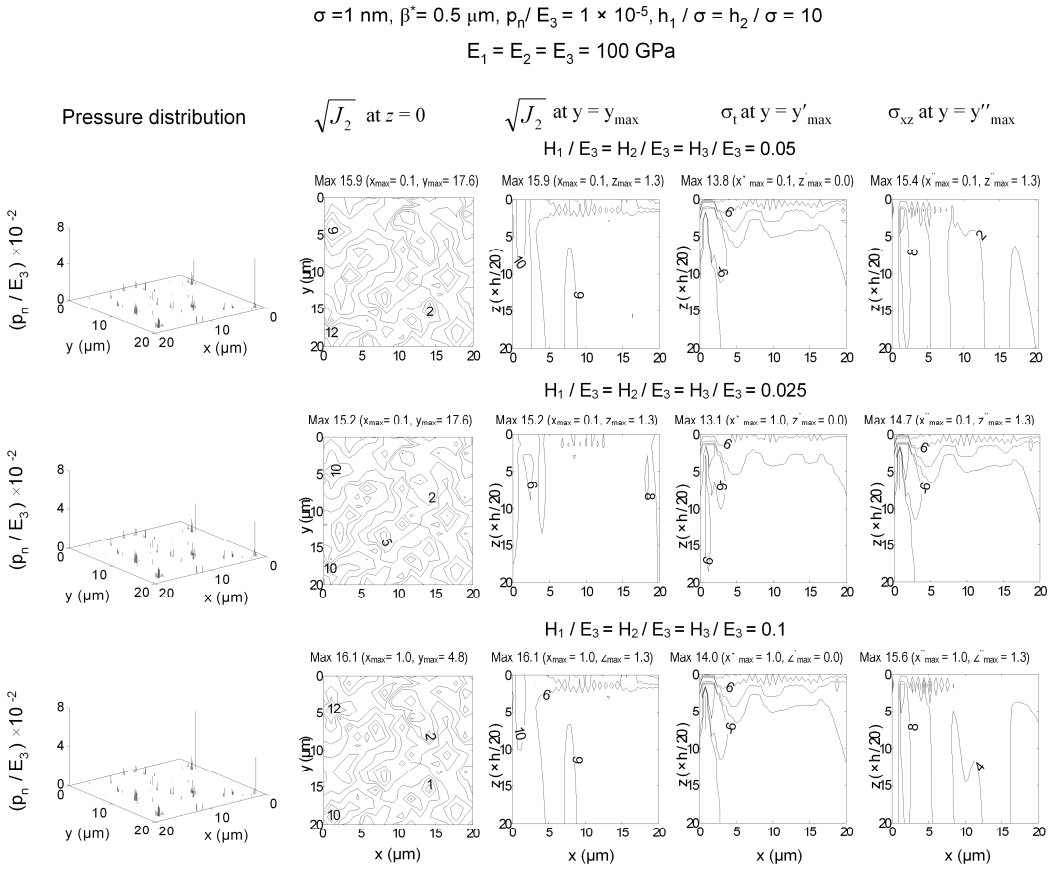

(a)

Figure 2.14. Three homogeneous cases with σ = 1 nm, β^* = 0.5 μm, and $E_1 = E_2 = E_3$ = 100 GPa, with different values of hardness. (a) Profiles of contact pressures, contours of von Mises stresses on the surface, von Mises stresses on the max $\sqrt{J_2}$ plane, principal tensile stresses on the max σ_t plane, and shear stresses on the max σ_{xz} plane with $p_n / E_3 = 1\times10^{-5}$, and (b) Variation of maximum pressure, fractional real area of contact, and fractional plastic real area of contact with normal pressure p_n for different values of $H_1 / E_3 = H_2 / E_3 = H_3 / E_3$ [Cai and Bhushan, 2006]. The arrows in (b) indicate the transition from elastic to elastic-perfectly plastic deformation.

Figure 2.14 (continued)

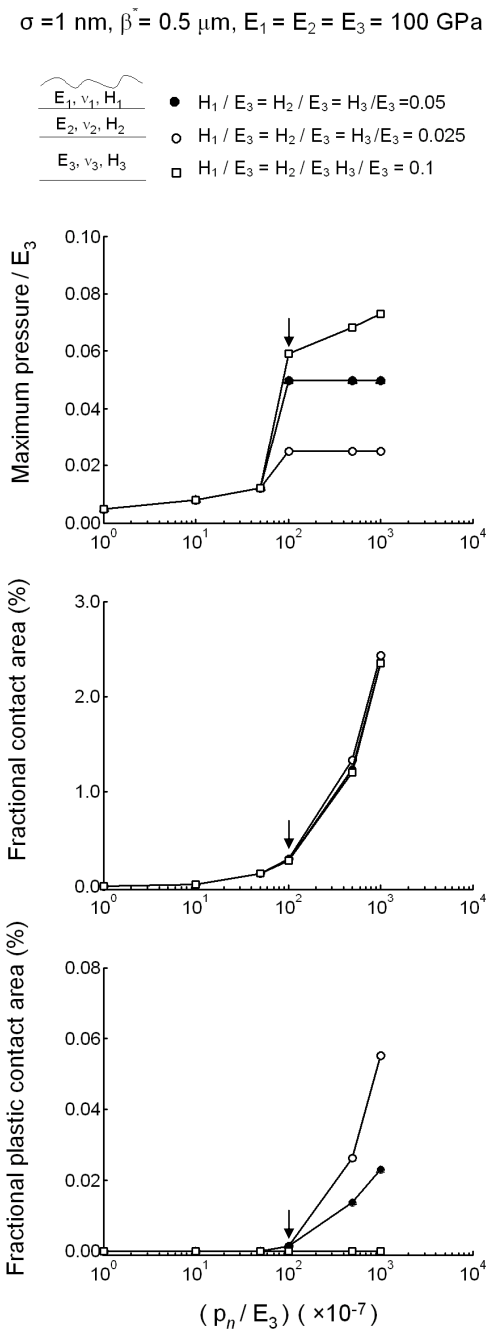

.(b)

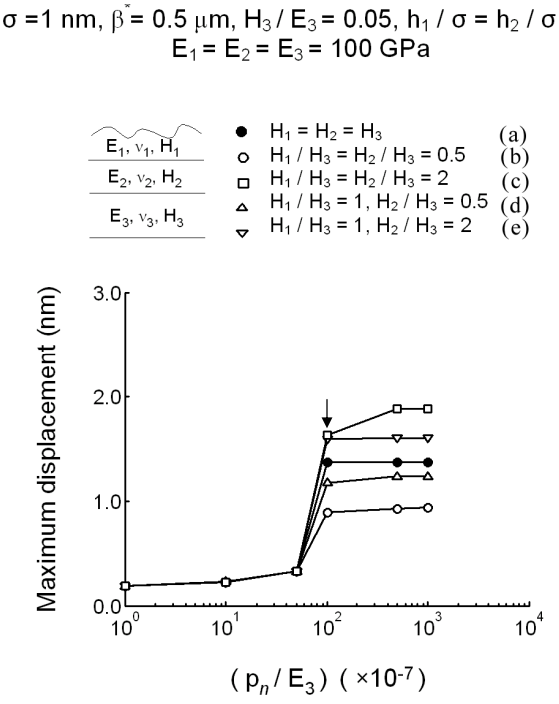

(a)

Figure 2.15. At different values of H_1 / H_3, H_2 / H_3, $\sigma = 1$ nm, $\beta^* = 0.5$ μm, $H_3 / E_3 = 0.05$, $h_1 / \sigma = h_2 / \sigma = 1$, and $E_1 = E_2 = E_3 = 100$ GPa, (a) variation of maximum displacement with normal pressure p_n, (b) profiles of contact pressures, contours of von Mises stresses on the surface, von Mises stresses on the max $\sqrt{J_2}$ plane, principal tensile stresses on the max σ_t plane and shear stresses on the max σ_{xz} plane with $p_n / E_3 = 1\times10^{-5}$, and (c) variation of maximum pressure, fractional real area of contact, and fractional plastic real area of contact with normal pressure p_n [Cai and Bhushan, 2006]. The arrows in (a) and (c) indicate the transition from elastic to elastic-perfectly plastic deformation.

Figure 2.15 (continued)

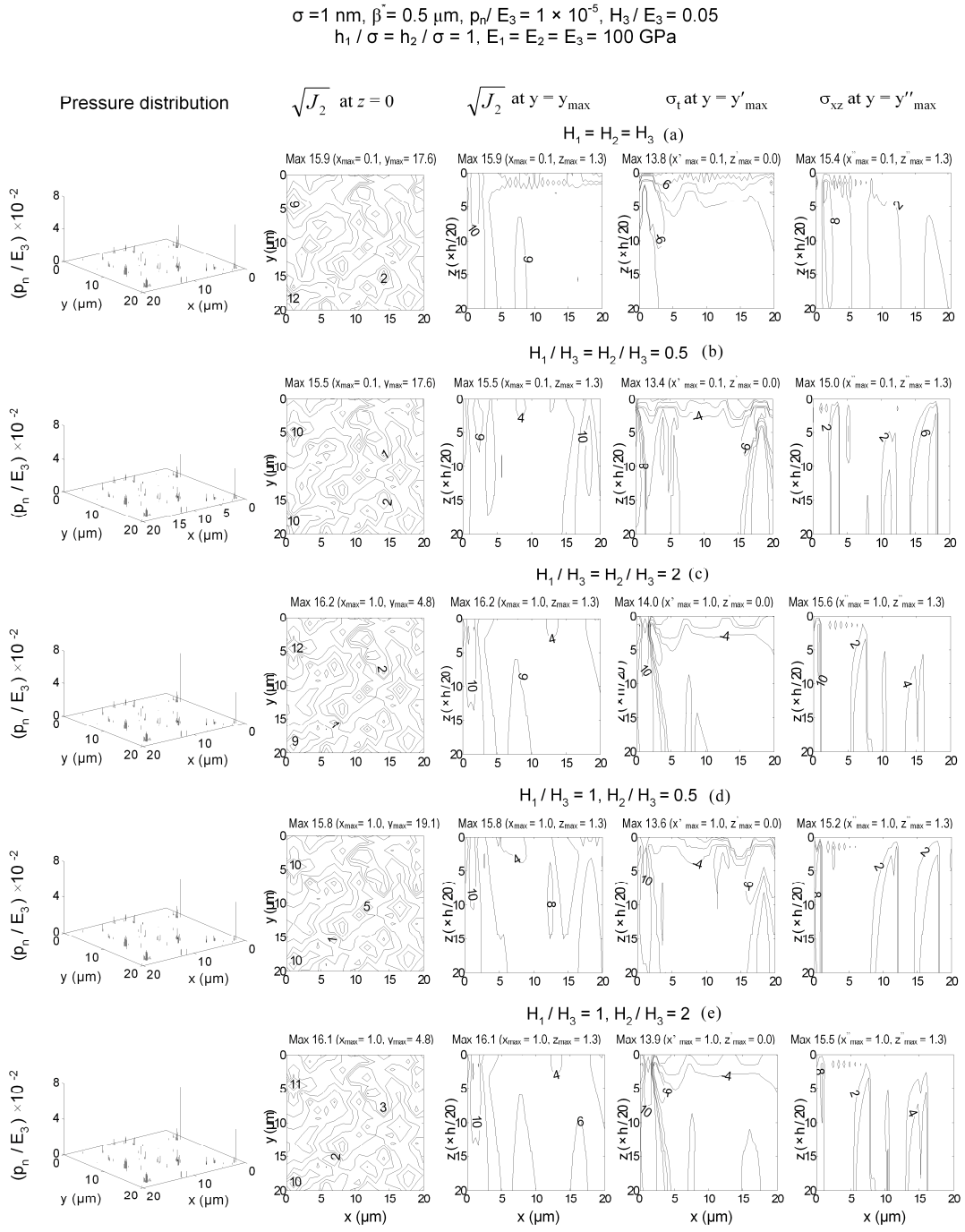

(b)

Figure 2.15 (continued)

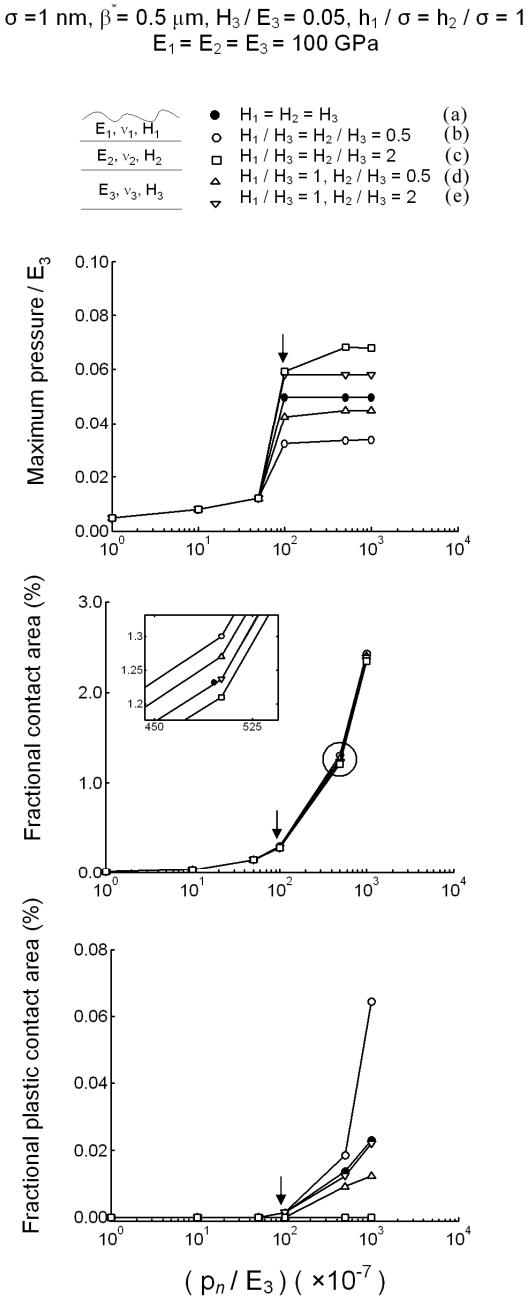

(c)

2.1.3.5.4 Layer thickness effect

The layer thickness effect can be obtained by examine two different layer thickness ($h_1 / \sigma = h_2 / \sigma = 10$ and $h_1 / \sigma = h_2 / \sigma = 1$) cases presented previously. The data generated based on $h_1 / \sigma = h_2 / \sigma = 10$ is presented in Figs. 2.10-12, and the data generated based on $h_1 / \sigma = h_2 / \sigma = 1$ is presented in Fig. 2.13. For the convenient of discussion while not losing generalization, Fig. 2.10 and 2.13 are used as example to study the layer thickness effect. Fig. 2.10 shows the contact statistics and maximum stresses as a function of applied load for various ratios of the Young's moduli of the layers to that of the substrate for $h_1 / \sigma = h_2 / \sigma = 10$, and Fig. 2.13 shows the same data but at $h_1 / \sigma = h_2 / \sigma = 1$. It is observed that the maximum contact pressure decreases but the real area of contact increases with the increase in layer thickness for a single layered solid with a more compliant top layer or a solid with a more compliant interlayer, and vice versa. The maximum contact pressure decrease with the increase in layer thickness for a single layered solid with a more compliant top layer or a solid with a more compliant interlayer, and vice versa. It is also noticed that the differences between these values (for various ratios of the Young's moduli of the layers to that of the substrate) became larger for $h_1 / \sigma = h_2 / \sigma = 10$ as compared to $h_1 / \sigma = h_2 / \sigma = 1$. This indicates that a proper increase in layer thickness can enhance the effect of the layers. A properly increased layer thickness can be used to maintain the layer effect to obtain low maximum pressure for low wear.

2.1.3.5.5. Loading effect

The effect of applied load for various Young's moduli is presented in Figs. 2.10-13. Fig. 2.10 shows the maximum contact pressure, the fractional real area of contact, and the fractional plastic contact area as a function of applied load for three chosen rough surfaces for these five structures with various ratios of the Young's moduli of the layers to that of the substrate. It is observed that the maximum contact pressure and real area of contact increase with the increase in applied load in the elastic contact regime. This is because the increased load brings the two contacting surfaces closer. Fig. 2.11 shows the maximum displacement as a function of applied load. It is observed the maximum

displacement increase with the increase in applied load. Fig. 2.12a and b show the pressure distribution on the surface and stress distributions on the surface and in the subsurface with maximum values of stresses for two different loads. The smaller load is for elastic contact, and the larger load is used to ensure elastic/perfectly plastic contact. It is observed that the pressure and stress distributions differ from each other. The maximum contact pressure and stresses are smaller for a lower load (Fig. 2.12a) as compared to a higher load (Fig. 2.12b). It is also noted that the number of contact points is smaller for a lower load, whereas they increase with the increase of an applied load. Fig. 2.13a shows the pressure and stress distributions for various ratios of the Young's moduli of the layers to that of the substrate, and Fig. 2.13b shows the maximum contact pressure, fractional contact area and fractional plastic contact area as functions of applied loads with a smaller layer thickness (as compared to Fig. 2.12). The results show that the trends are consistent with those observed in Fig. 2.10 and 2.12.

The effect of applied load on contact pressure profile, maximum displacement, maximum stresses, and real area of contact for different hardness is presented in Figs. 2.14 and 15. Fig. 2.14a shows the pressure and stress distributions; and Fig. 2.14b shows the maximum contact pressure, fractional real area of contact and fractional plastic contact area as a function of applied load for three homogeneous solids. Fig. 2.15a shows the maximum displacement as a function of applied load; Fig. 2.15b shows the pressure profile and stress distributions; Fig. 2.15c shows the maximum contact pressure, fractional real area of contact and fractional plastic contact area as a function of applied load for the chosen five structures. The results show that the maximum local deformation increases with the increase in applied load in the elastic deformation regime. This is expected due to the application of the theory of elasticity. However, the local deformation does not necessarily increase linearly with the increase in applied load due to the roughness effect. The magnitude of deformation does not change after plastic contact occurs. This is because of the assumption of elastic-perfectly plastic contact used in the analysis. The increases in magnitude of local contact pressure and real area of contact are moderate at the beginning, but these increasing become significant when a partial plastic contact occurs. The maximum contact pressure increases with the increase in the normal

load until it reaches the effective hardness. After that, plastic contact occurs and the maximum pressure remains constant.

2.1.3.5.6. Coefficient of friction effect

Effect of coefficient of friction for various ratios of the Young's moduli and hardness of the layers to that of the substrate at two different loads and two different layer thicknesses are used as example to perform the analysis. The lower load is used for elastic contact and the larger load is used to ensure elastic/perfectly plastic contact. The corresponding results the lower applied load are shown in Figs. 2.16-18 and the results for the larger load are shown in Figs. 2.19-21.

Figure 16 shows the pressure distributions and stress distributions for a coefficient of friction $\mu = 0.5$ for $h_1 / \sigma = h_2 / \sigma = 1$ for various Young's moduli and the hardness. It is observed that the locations of the maximum stresses are all moved to surface at $\mu = 0.5$. Fig.17 shows the maximum contact stresses ((a) von Mises stress, (b) tensile stress and (c) shear stress) as a function of coefficient of friction for various ratios of the Young's moduli of the layers to that of the substrate under the applied lower load. Fig.18 shows the maximum contact stresses ((a) von Mises stress, (b) tensile stress and (c) shear stress) as a function of coefficient of friction for various ratios of the hardness of the layers to that of the substrate the same applied lower load, but a larger layer thicknesses. The results show that the increase in coefficient of friction leads to a quick increase in the maximum stresses. The increases in maximum von Mises and shear stresses are not significant at low friction; however, these stress values increase rapidly as the coefficient of friction increases. The effect of stiffness and hardness on the contact statistics and the maximum stresses are the same as observed in the frictionless analysis. A stiff or hard top layer leads to higher stresses and a compliant or soft top layer, or a compliant or soft interlayer leads to lower stresses. By comparing Figs. 17 and 18, the layer effect on maximum stresses tends to decrease with increased friction for the case of $h_1 / \sigma = h_2 / \sigma = 1$, and friction dominates the magnitude changes of these stresses. But this trend changes for $h_1 / \sigma = h_2 / \sigma = 10$. A properly increased layer thickness may be used to maintain the layer effect to obtain low maximum stresses for low wear.

Figures 19-21 show the same corresponding data as compared to Figs. 16-18 but at a larger applied load. Again, the larger load is used to ensure elastic-perfectly plastic contact. It is observed that the increase in coefficient of friction leads to a quick increase in the maximum stresses. As compared to the elastic contact (Figs. 16-18), the elastic-perfectly plastic contact (Figs. 19-21) does not change this trend. But, in the elastic-perfectly-plastic contact domain, the increase in maximum von Mises and shear stresses are significant from the low to high friction range (as shown in Figs. 20 and 21).

These results show that introducing friction plays a major role in the increase in maximum surface/subsurface stresses and the movement of the locations of those stresses to the surface. These observations indicate that a compliant or soft interlayer with a proper layer thickness can be used to reduce the maximum stresses, and thus reduce the potential wear.

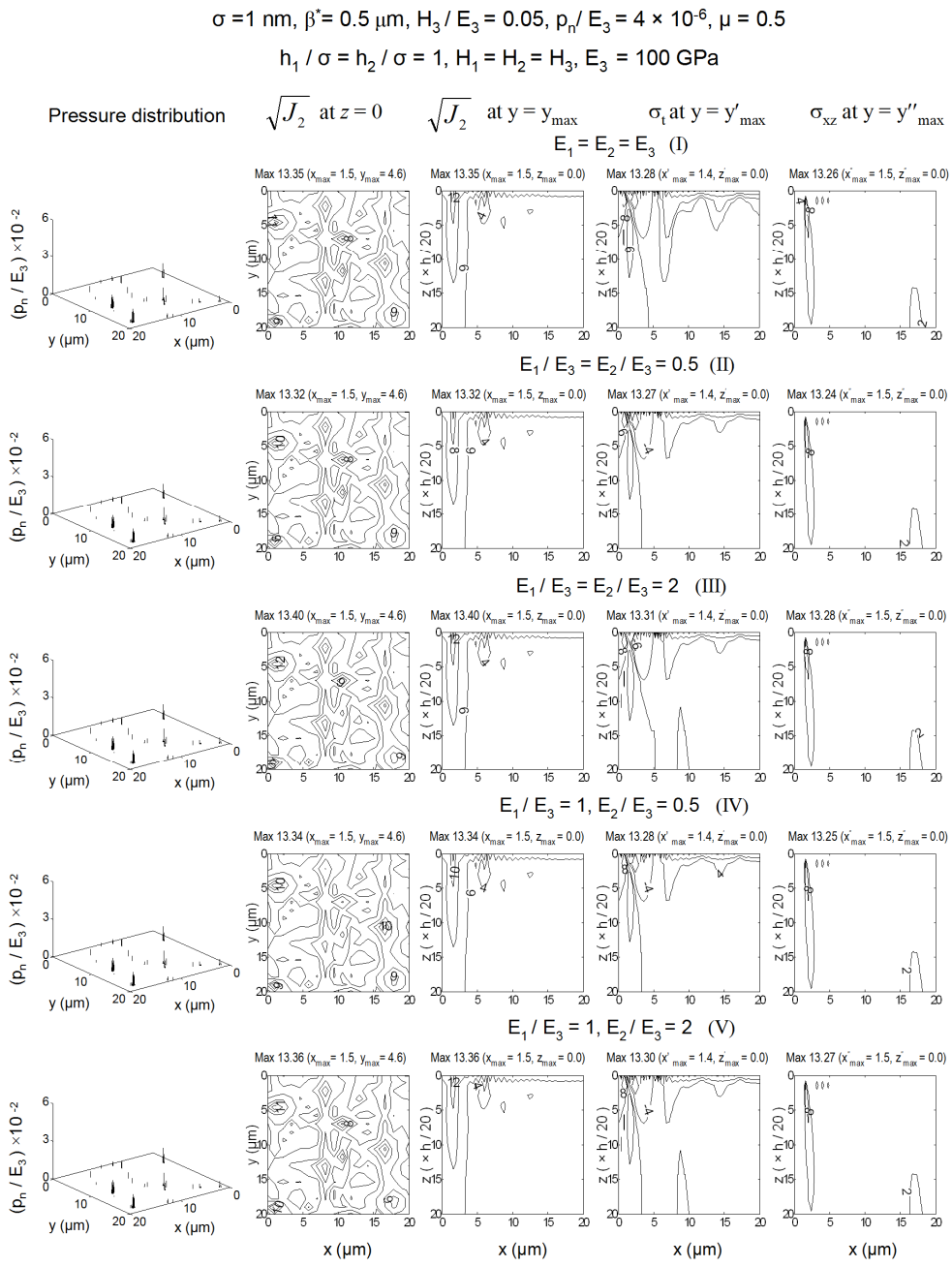

Figure 2. 16. At different values of E_1 / E_3, E_2 / E_3, $\sigma = 1$ nm, $\beta^* = 0.5$ μm, $H_3 / E_3 = 0.05$, $p_n / E_3 = 4\times10^{-6}$, $h_1 / \sigma = h_2 / \sigma = 1$, $H_1 = H_2 = H_3$, $E_3 = 100$ GPa, and $\mu = 0.5$, profiles of contact pressures, contours of von Mises stresses on the surface, von Mises stresses on the max $\sqrt{J_2}$ plane, principal tensile stresses on the max σ_t plane and shear stresses on the max σ_{xz} plane [Cai and Bhushan, 2007a]

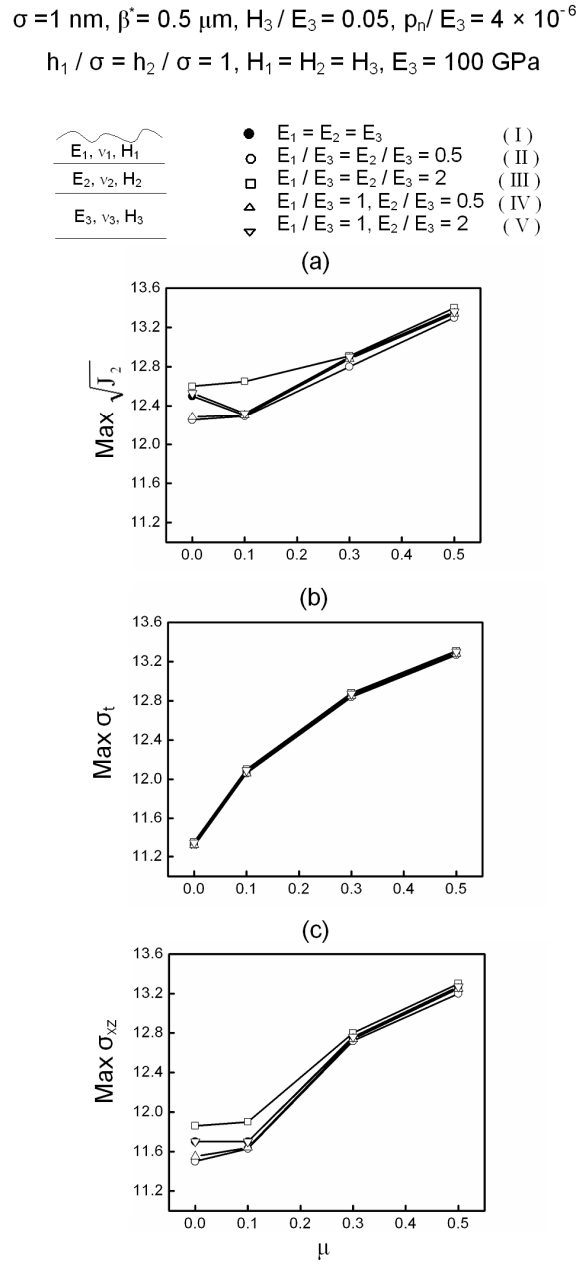

Figure 2. 17. At different values of E_1 / E_3, E_2 / E_3, $\sigma = 1$ nm, $\beta^* = 0.5$ μm, $H_3 / E_3 = 0.05$, $p_n / E_3 = 4\times10^{-6}$, $h_1 / \sigma = h_2 / \sigma = 1$, $H_1 = H_2 = H_3$, $E_3 = 100$ GPa, variation of maximum stresses with coefficient of friction, (a) von Mises stress, (b) tensile stress, and (c) shear stress [Cai and Bhushan, 2007a].

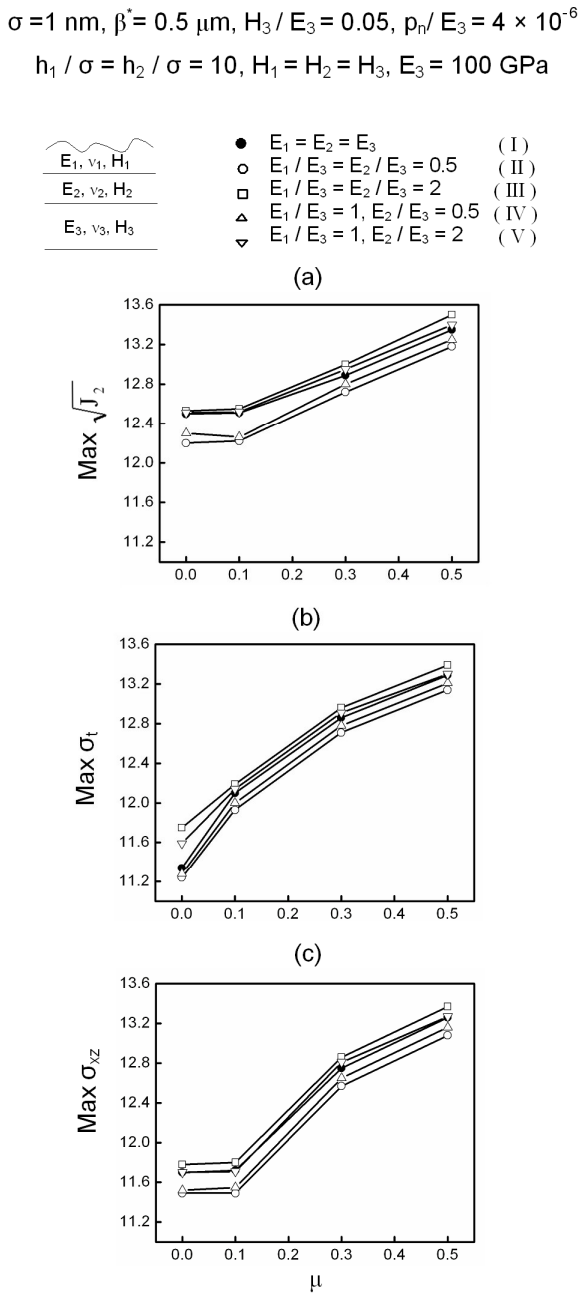

Figure 2.18. At different values of E_1 / E_3, E_2 / E_3, $\sigma = 1$ nm, $\beta^* = 0.5$ μm, $H_3 / E_3 = 0.05$, $p_n / E_3 = 4\times10^{-6}$, $h_1 / \sigma = h_2 / \sigma = 10$, $H_1 = H_2 = H_3$, $E_3 = 100$ GPa, variation of maximum stresses with coefficient of friction, (a) von Mises stress, (b) tensile stress, and (c) shear stress [Cai and Bhushan, 2007a].

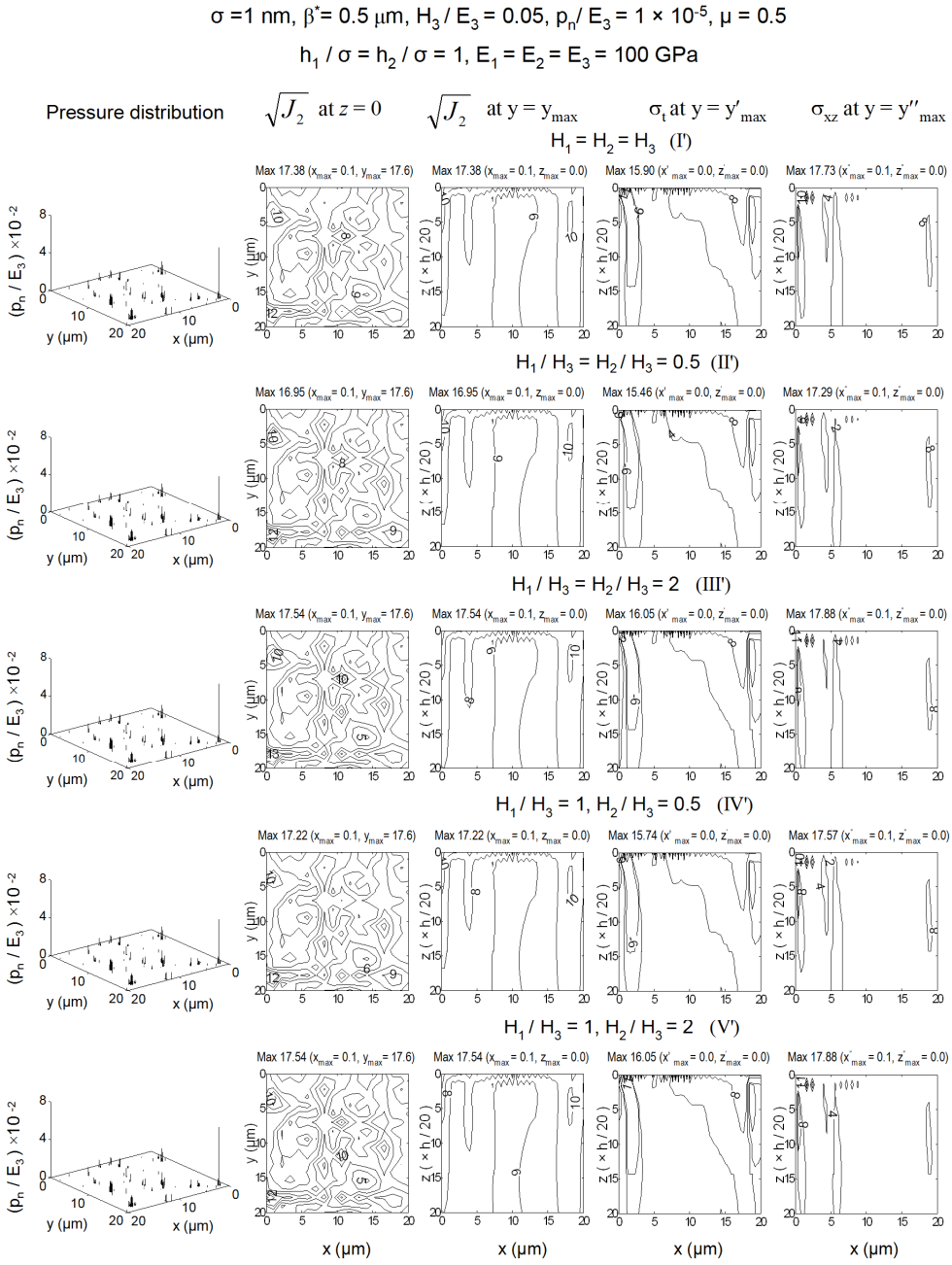

Figure 2. 19. At different values of H_1 / H_3, H_2 / H_3, $\sigma = 1$ nm, $\beta^* = 0.5$ μm, $H_3 / E_3 = 0.05$, $p_n / E_3 = 1\times10^{-5}$, $h_1 / \sigma = h_2 / \sigma = 1$, $E_1 = E_2 = E_3 = 100$ GPa, $\mu = 0.5$, profiles of contact pressures, contours of von Mises stresses on the surface, von Mises stresses on the max $\sqrt{J_2}$ plane, principal tensile stresses on the max σ_t plane and shear stresses on the max σ_{xz} plane [Cai and Bhushan, 2007a].

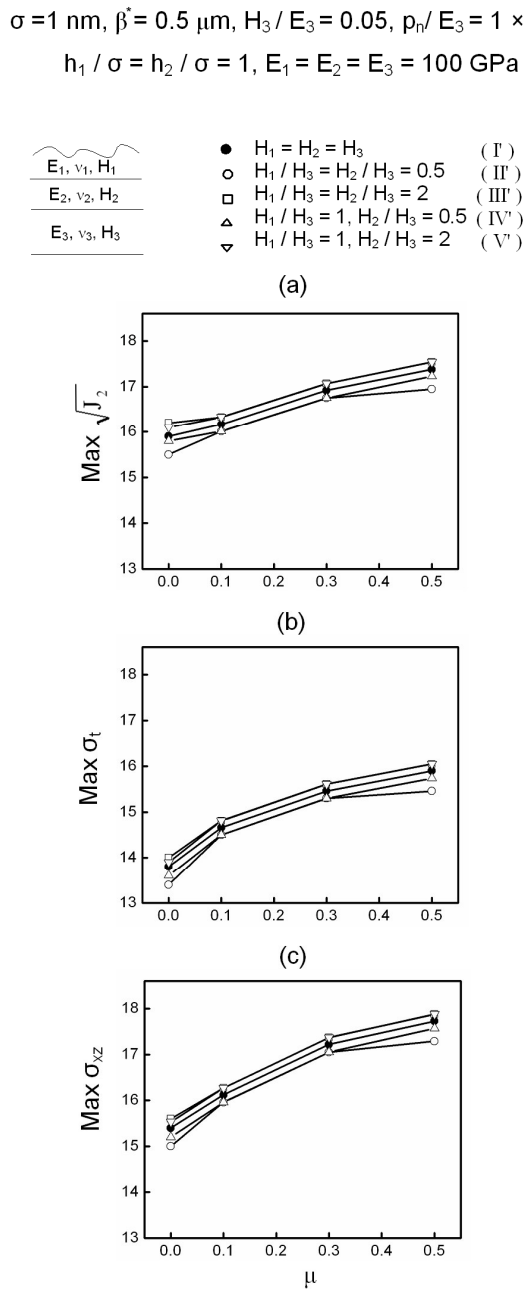

Figure 2.20. At different values of H_1 / H_3, H_2 / H_3, $\sigma = 1$ nm, $\beta^* = 0.5$ μm, $H_3 / E_3 = 0.05$, $p_n / E_3 = 1 \times 10^{-5}$, $h_1 / \sigma = h_2 / \sigma = 1$, $E_1 = E_2 = E_3 = 100$ GPa, variation of maximum stresses with coefficient of friction, (a) von Mises stress, (b) tensile stress, and (c) shear stress [Cai and Bhushan, 2007a].

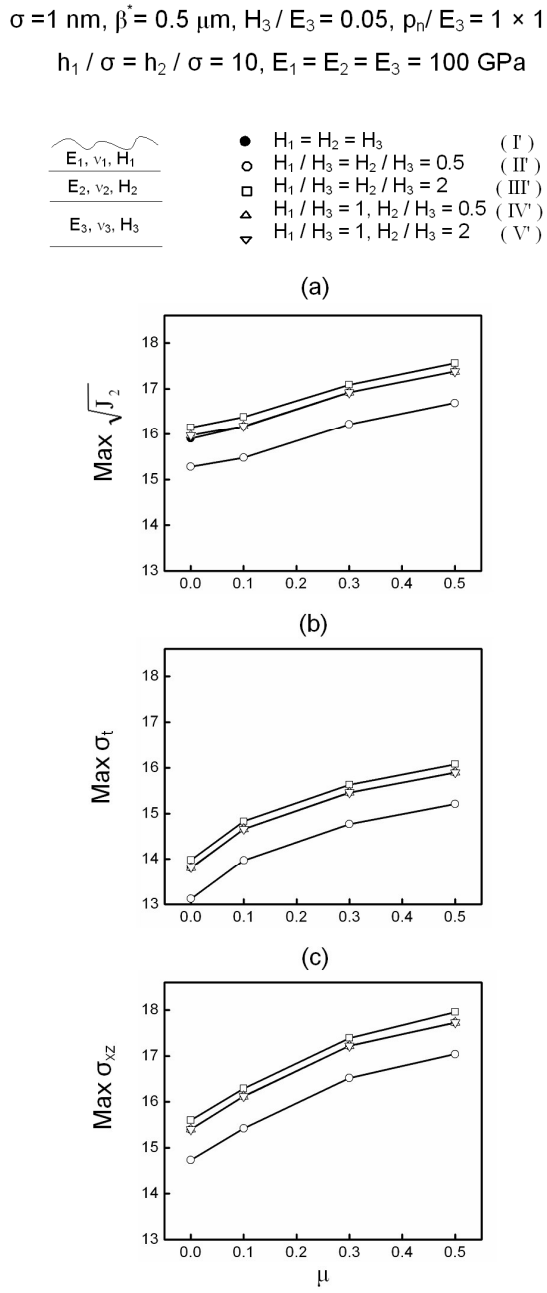

Figure 2.21 At different values of H_1 / H_3, H_2 / H_3, $\sigma = 1$ nm, $\beta^* = 0.5$ μm, $H_3 / E_3 = 0.05$, $p_n / E_3 = 1 \times 10^{-5}$, $h_1 / \sigma = h_2 / \sigma = 10$, $E_1 = E_2 = E_3 = 100$ GPa, variation of maximum stresses with coefficient of friction, (a) von Mises stress, (b) tensile stress, and (c) shear stress [Cai and Bhushan, 2007a].

2.2. Wet contact of multilayered rough flat surfaces

Menisci form around the contacting and near contacting asperities due to surface energy effects (Adamson, 1990; Israelachvili, 1992; Bhushan, 1999b, 2002, 2003, 2005) with the presence of a thin liquid film between two contacting surfaces. As shown in Fig. 2.22, a meniscus forms wherever an asperity touches the film. Meniscus rings are formed on contacting asperities, and meniscus bridges are formed on non-contacting asperities. The lower pressure inside the meniscus, i.e., negative Laplace pressure, results in an additional pulling force, meniscus force, acting on the contact interface. It can result in undesirable adhesion and friction at the interface and causes stiction.

For contact in wet conditions, Bowden and Tabor (1950) were among the first few who analyzed the effects of meniscus forces between two contacting bodies with the presence of a liquid film. They studied a smooth ball against a smooth plate. An increase in adhesion force was generally observed when a thin film of liquid was introduced at the contact interface either through adsorption or by deposition. For rough surface contact, the increase in liquid film thickness results in more menisci forming around the asperities, which in turn leads to an increase in adhesive force. Tian and Bhushan (1996) studied the micro-meniscus effect based on a multiasperity contact model for homogeneous solids. They found that the micro-meniscus effect on static friction at the interface depends on surface roughness and waviness, liquid film thickness and its mobility, material's Young's modulus and the applied load. The numerical model developed by Tian and Bhushan (1996) modified the classical meniscus theory of single spherical asperity contact to include the effect of multiple asperity contact. Meniscus effects were studied for an ultra thin liquid film present at the contact interface. Wetted areas are determined by selecting the area where asperities of both contacting surfaces touch the liquid, and the total projected meniscus area is determined by selecting the cross-sectional area at a given meniscus height which overlap the wetted area. The film thickness is assumed to be uniform everywhere on the flat surface. The meniscus force is then calculated using the extended first principle of the micro meniscus theory with the following equation:

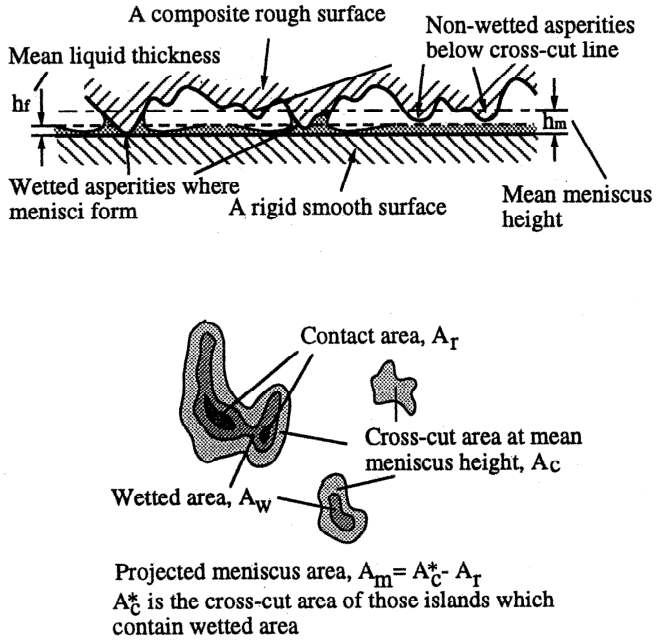

Figure 2.22. Schematic of a rough surface in contact with a smooth surface in the presence of a liquid film.

$$F_m = \frac{\gamma(\cos\theta_1 + \cos\theta_2)A_m}{h_m} \tag{2.43}$$

where γ is the surface tension of the liquid, θ_1 and θ_2 are the contact angles of the liquid on the two solid surfaces, A_m is the total meniscus area, and h_m is the mean meniscus height. Peng and Bhushan (2002) applied this model to a single-layer model to study the layer effect. This model is further extended by Cai and Bhushan (2006) to two-layered solids with rough surfaces to better understand the phenomena and to identify the optimal parameters to achieve low friction/stiction.

The analysis carried out here by Cai and Bhushan (2006) is based on a rigid surface in contact with a rough elastic-perfectly plastic two-layered solid surface. Young's modulus of the substrate E_3 is taken as 100 GPa. The pressure is normalized by E_3. Poisson's ratios are taken as 0.3 for all the cases. The hardness of the substrate is taken as $0.05E_3$. The rough surface has a correlation length $\beta^* = \beta_x = \beta_y = 0.5$ μm and a surface height deviation σ = 1 nm. The ratio of the layer thickness to the surface height deviation is taken as $h_1 / \sigma = h_2 / \sigma = 10$ and 1 for various ratios of the Young's moduli of the layers to that of the substrate with fixed hardness. Effect of various ratios of the hardness of the layers to that of the substrate for a fixed Young's modulus is reported for a homogeneous case and $h_1 / \sigma = h_2 / \sigma = 1$. Only the smaller layer thickness is used here to ensure the composite hardness plays a role. In the wet contact simulation, the liquid thin film is taken as water, the surface tension γ=7.275×10^{-2} N/m, the contact angles θ are all $\pi/3$, and the film thickness and meniscus height have the same value of σ.

Figure 2.23 shows the normalized meniscus force (relative meniscus force F_m / W, where W is the externally applied load) as a function of applied load for various ratios of the stiffness of the layers to that of the substrate. Accompanied with Fig. 2.13b, the results indicate that the meniscus force changes with the real area of contact. The increase in real area of contact is accompanied by an increase in the absolute value of the meniscus force, whereas the relative meniscus force decreases. This trend is consistent with that observed by Bhushan and Peng (2002). The relative meniscus force decreases

nonlinearly with the increase in load even though the absolute value of the meniscus force increases. It is observed that the meniscus force is much more sensitive in a purely elastic contact regime than in an elastic-plastic contact regime. This trend differs from that of the real area of contact, which is more sensitive to the applied load in the elastic-plastic contact regime. For a given externally applied load, the meniscus force is lower for stiff top layers, since fewer asperities can touch the liquid and form menisci, which is beneficial in reducing friction and stiction; whereas, compliant top layers have the opposite effects, and thus are more likely to cause stiction and higher friction. This agrees with common engineering experience and the results presented by Bhushan and Peng (2002) for a single-layered model. A compliant interlayer (IV) leads to a larger decrease in relative meniscus force as compared to that of a compliant top layer (II), and a stiff interlayer (V) leads only to a small increase in relative meniscus force as compared to that of a stiff top layer (III). It is also observed that the decrease or increase in the magnitude of the relative meniscus force with the presence of an interlayer (stiff or compliant) is small compared to a homogeneous solid (I). The relative meniscus force is observed to be sensitive to layer thickness. This can be easily identified in Fig. 2.23 at $h_1 / \sigma = h_2 / \sigma = 10$ and $h_1 / \sigma = h_2 / \sigma = 1$. The changing of meniscus force is small at a given load between each structure as layer thicknesses are $h_1 / \sigma = h_2 / \sigma = 1$.

Figure 2.24 shows the normalized meniscus force as a function of applied load for various ratios of the hardness of the layers to that of the substrate. It is observed that the meniscus force varies with a change in the hardness ratios only in the elastic-plastic contact regime since the contact area remains in the elastic regime. The arrows in the figures indicate the transition from elastic to elastic-perfectly plastic deformation. Also, the trends are similar to that in Fig. 2.23, whereas a soft interlayer (IV') leads to a significant decrease in meniscus force as compared to a soft top layer (II'), and a hard interlayer (V') leads to only a trivial increase in meniscus forces as compared to a hard top layer (III'). Combined with the observations, the results of the wet contact further show that the use of an interlayer is an effective way to minimize friction/stiction.

The roughness effect on meniscus forces has been performed for three rough surfaces, with $\sigma = 1$ nm and $\beta^* = 0.5$ and 0.05 μm, and $\sigma = 10$ nm and $\beta^* = 0.05$ μm. Fig.

2.25 shows the relationship between relative meniscus force and roughness for various ratios of the stiffness of the layers to that of the substrate. The results show that an increase in roughness (increase in standard deviation of surface height σ or decrease in correlation length β^*) leads to a decrease in relative meniscus force. As compared to decrease in β^*, the relative meniscus force are more sensitive to the increase in σ. The increase in σ leads to a large decrease in relative meniscus force.

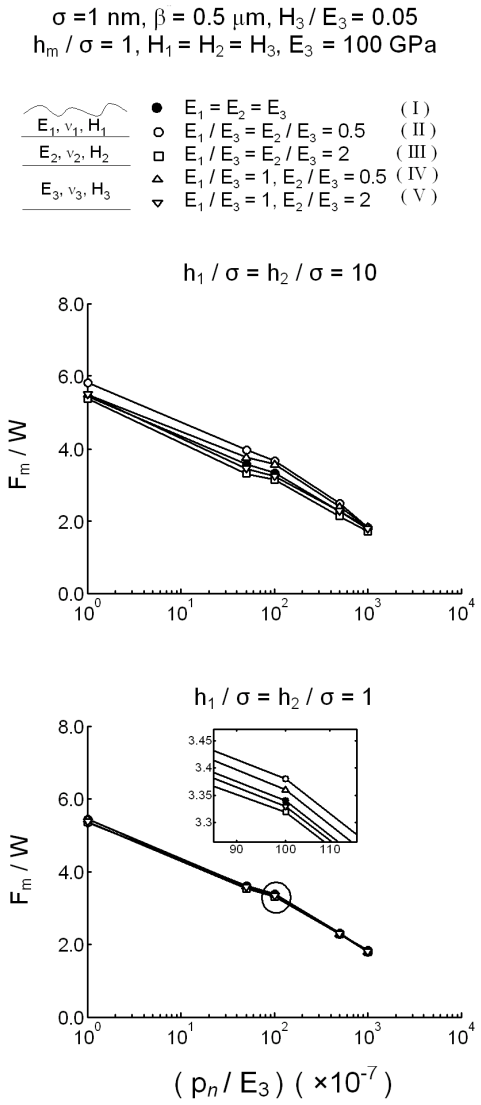

Figure 2.23. Variation of relative meniscus force with normal pressure p_n for $\sigma = 1$ nm, $\beta^* = 0.5$ μm, $H_3 / E_3 = 0.05$ at different values of E_1 / E_3, E_2 / E_3 for $h_1 / \sigma = h_2 / \sigma = 10$ and $h_1 / \sigma = h_2 / \sigma = 1$ with $H_1 = H_2 = H_3$, $E_3 = 100$ GPa [Cai and Bhushan, 2006].

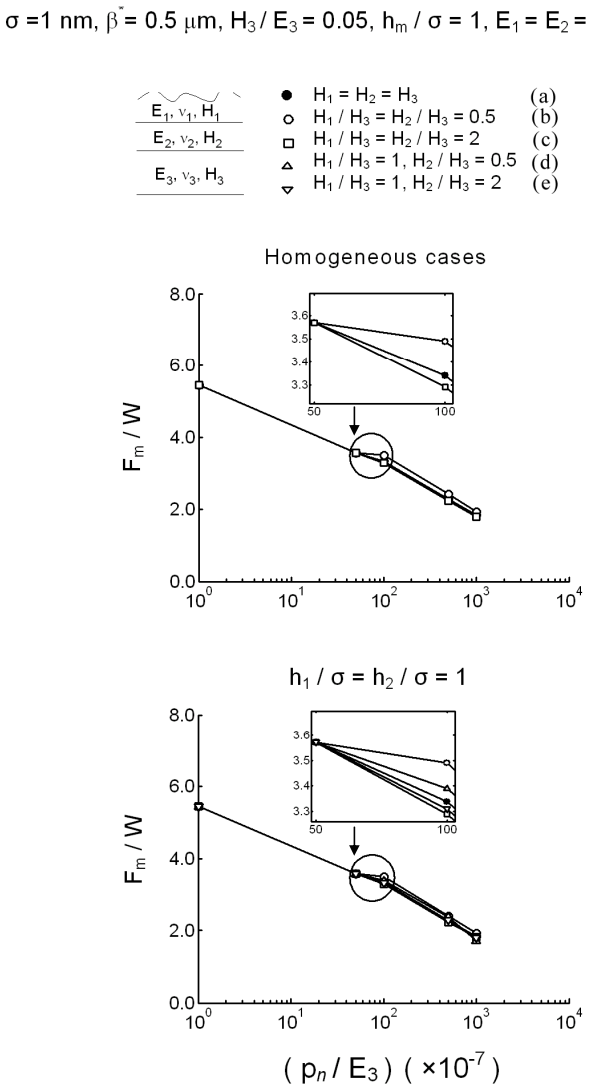

Figure 2.24. Variation of relative meniscus force with normal pressure p_n for σ = 1 nm, β^* = 0.5 μm, $H_3 / E_3 = 0.05$ at different values of H_1 / H_3, H_2 / H_3 for three homogeneous cases and $h_1 / \sigma = h_2 / \sigma = 1$ with $E_1 = E_2 = E_3 = 100$ GPa [Cai and Bhushan, 2006]. The arrows in the figure indicate the transition from elastic to elastic-perfectly plastic deformation. The arrows in the figure indicate the transition from elastic to elastic-perfectly plastic deformation.

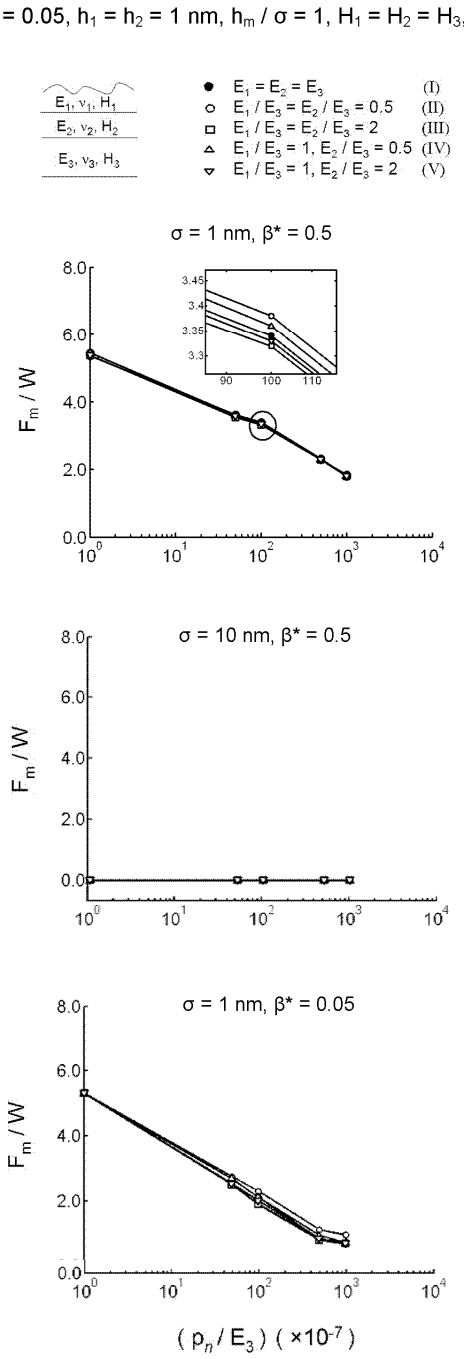

Figure 2.25. Variation of relative meniscus force with normal pressure p_n for $H_3 / E_3 = 0.05$ at different values of E_1 / E_3, E_2 / E_3 with $H_1 = H_2 = H_3$, $E_3 = 100$ GPa and $h_1 = h_2 = 1$ nm for three roughness cases with $\sigma = 1$ nm and $\beta^* = 0.5$ and 0.05, and $\sigma = 10$ nm and $\beta^* = 0.5$ μm.

2.3. Applications

The numerical 3D rough two-layered contact model under combined normal and tangential loading enables one to obtain optimal configurations, i.e. mechanical properties, layers parameters, and surface roughness parameters, for practical design of layered surfaces. Three main uses of the study can easily be identified. First, the model provides the direction to choose candidate materials with ideal mechanical properties when the candidate material for a product is uncertain. Secondly, given that several candidate materials are available, the model can be used to identify the ideal one or a combination from a tribological point of view. Thirdly, given that the combination of materials is known for a certain product/medium, the model is able to provide optimal design parameters, e.g., layer thicknesses and optimal surface roughness parameters for improving the tribological properties, e.g., low friction and wear.

An example of industrial application using the model is head-disk interface in magnetic thin-film rigid disk drives. The multilayered construction of a thin-film rigid disk is shown in Fig. 2.26 (Bhushan, 1996). The physical properties and surface topography statistics of a conventional magnetic thin-film (metal) disk and an Al_2O_3-TiC slider were presented in Table 2.1. Roughness σ of the disk and sliders are on the order of 1 nm. Liquid lubricant is applied to reduce friction; however, it may also lead to stiction due to the formation of micro menisci. A diamond-like carbon coating (DLC) is used as a protection layer against corrosion and wear. The choice of layer thickness is selected based on experience. The read-write operation is performed under steady operating conditions where a load-carrying film is formed to separate the slider from the disk, and only isolated asperity contacts may occur between them. Physical separation in today's drives is about 2 to 5 nm. During the start-stop operations of the disk drive, physical contact occurs, and friction, stiction and wear are major issues. The friction/stiction is associated with real area of contact, and wear is related to maximum stress level. The reduction of the real area of contact and maximum stress level will help to reduce or avoid such problems.

Based on the analysis, the increase in surface roughness (increase in standard deviation of surface height σ or decrease in correlation length β^*) leads to a decrease in

real area of contact but an increase in the contact pressure and maximum stresses. The increase in roughness also leads to a decrease in relative meniscus force especially for the increase in the standard deviation of surface height. The surface roughness needs to be optimized for a lower value of real area of contact, the maximum stresses and meniscus force. As compared to a homogeneous solid, a stiff top layer leads to smaller real area of contact and larger contact pressure and stresses; a more compliant interlayer leads to lower maximum contact pressure and surface/subsurface stresses but a larger real area of contact, whereas, a more stiff interlayer has an opposite trend. An increase in the layer thickness enhances these effects, i.e., a compliant interlayer with a larger thickness leads to an larger real area of contact but a smaller contact pressure and maximum stresses, and vice versa. A stiffer and harder top layer is suggested to be used in the design of these products since a stiffer and harder top layer leads to a smaller real area of contact. Also, the harder top layer can help to avoid or minimize the possible plastic contact and thus reduce the potential high wear. Alternatively, the combination of a hard top layer and a softer interlayer with a proper layer thickness can also help to achieve the goal. With a presence of liquid at the contact interface, meniscus force becomes an important source of adhesion. The meniscus force increases with an increase in number of menisci. An increase in σ or a decrease in β^* leads to a decrease in numbers of menisci, and thus can used to reduce adhesion due to the menisci.

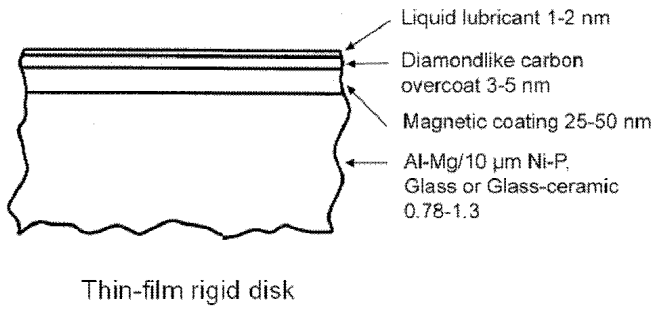

Figure 2.26. Cross-sectional schematic of magnetic storage media: thin-film rigid disk.

Disk materials/slider	E (GPa)	ν	H (GPa)	σ (nm)	β^* (μm)
DLC overcoat	140, 280[1]	0.25[1]	15, 24[1]	2.1,4.6,7.3[2]	36, 3, 4[2]
Co-Cr alloy magnetic coating	190[2]		9[2]		
Ni-P on Al-Mg alloy	130[2]	0.36[3]	7[2]		
Al-Mg alloy	70[2]				
Glass ceramics	150[4]	0.25[5]	13[4]		
Al_2O_3-TiC slider	450[2]	0.23[3]	23[2]	1.5[2]	20[2]

[1][Bhushan, 1999a], [2][Bhushan, 1996a], [3][Chilamakuri and Bhushan, 1998], [4][Bhushan et al., 1996], [5][Poon and Bhushan, 1996]

Table 2.1. Typical physical properties and surface topography statistics of magnetic thin-film disks and.

	Medium	Max pressure	Contact area	Meniscus force	Max stress	Friction	Wear	Suggestion
Stiffness effect	Homogeneous	–	–	–	–	–	–	–
	Single compliant layer	↓↓	↑↑	↑↑	↓↓	↑↑	↓↓	Avoid in design
	Single stiff layer	↑↑	↓	↓↓	↑	↓	↑↑	Good for lower fiction
	Two layers with a compliant interlayer	↓↓	↑	↑	↓↓	↑	↓↓	Ideal for lower wear
	Two layers with a Stiff interlayer	↑	↓	↓	↑	↓	↑	Relative low friction
Hardness effect	Homogeneous	–	–	–	–	–	–	–
	Single soft layer	↓	↑↑	↑↑	↓↓	↑↑	↑↑ (Plastic contact is easy to occur)	Avoid in design
	Single hard layer	↑↑	↓	↓	↑	↓	↓↓ (Plastic contact is hard to occur)	Ideal for lower friction and wear
	Two layers with a soft interlayer	↓↓	↑	↑	↓↓	↑	↓↓	Ideal for lower wear
	Two layers with a hard interlayer	↑	→	↓	↑↑	→	↑	No benefit

Note — For stiffness effect, the hardness is kept the same, and vice versa. All layered structures are compared to a homogeneous solid. The suggestions are made from tribological point of view. The trends for max stresses in the table are based on proper layer thicknesses, and compromise may be needed for both enhanced effects of stiffness and hardness [Cai and Bhushan, 2007].

Table 2.2. Summary of tribological properties of layered solids in contact under normal loading or combined normal loading and friction force.

2.4. Recommendations for future work

It would be instructive to extend the rough multilayered to further investigate the plasticity at the contact. In the current dry contact models, the plastic contact is generally identified based on an onset of plastic deformation assuming material behaves as elastic-perfectly plastic. The new model may employ certain plastic flow models to account for the elastic- plastic flow at the contact spots.

It would be of interest to extend the current rough multilayered contact models to study the stick-slip phenomenon and to examine the friction induced vibration and instability. The new model may include a material model, i.e., a simple spring-damper model in both normal and tangential directions at each of the contact asperities. The new model is expected to be used to perform dynamic analyses to investigate the dynamic forces and motion in elastic contact domain. These studies will provide useful information for control of tribological properties, noise and vibration.

Real sliding is also a topic of interest which can be taken into consideration in the future studies. Though friction forces have been considered in the current models, no real relative motion of the contacting two surfaces is considered. A new model can be developed by considering surface displacement as a function of time. Material may be removed during the real sliding motion of the contacting surfaces. So, a certain wear model at the plastic contact points (whenever applicable) can be applied to take care of the shear of material.

CHAPTER 3

MENISCUS AND VISCOUS FORCES DURING SEPARATION OF HYDROPHILIC AND HYDROPHOBIC SURFACES WITH LIQUID-MEDIATED CONTACTS

3.1. Meniscus forces during static condition with symmetric and asymmetric contact angles

Menisci form around the contacting and near-contacting asperities due to surface energy effects in the presence of a thin liquid film. The following assumptions are commonly used. The two surfaces are assumed to be rigid. The meniscus bridge is assumed to be in equilibrium, and the liquid is incompressible. Thermal effects are considered to be negligible. Body force and inertia of the liquid are neglected, which has been justified, for example, by Cameron and McEttles (1981). The pressure is assumed to be a constant on a vertical cross section plane, whereas it varies along a radial direction through the meniscus bridge in the process of separation. The calculation of meniscus force can be carried out based on the solution of a mean meniscus curvature. The mean meniscus curvature can be solved from the Laplace-Young equation as done by Woodrow et al. (1961) and Orr et al. (1975). The configuration of the meniscus pendular ring or liquid bridge for a general situation of sphere on flat is shown in Fig. 3.1. In the figure, R is the radius of the sphere, D is the distance between the sphere and the flat surface, θ_1 and θ_2 are contact angles on the two surfaces, r_m and r_a are the two radii in two perpendicular planes, and ε is an arbitrary angle. The Bond number $gL^2\Delta\rho/\gamma$ is used to

measure the importance of surface tension force compared to body force. In the expression for the Bond number, g is gravitational acceleration, $\Delta\rho$ is the density difference between the liquids on either side of the interface, γ is the surface tension of the liquid, and L is a characteristic length for the system and is reported to be small (Orr et al., 1975). It is noted that a high Bond number indicates that a given system is relatively unaffected by surface tension effects and vice versa. For a small Bond number for the liquid meniscus, the effect of body force due to gravity is negligible, and the mean curvature is expected to be nearly uniform. If the meniscus is axisymmetric, its mean given as according to Orr et al. (1975)

$$2\overline{\kappa} = \frac{d^2z/dr^2}{[1+(dz/dr)^2]^{3/2}} + \frac{dz/dr}{r[1+(dz/dr)^2]^{1/2}} \qquad (3.1)$$

where $\overline{\kappa}$ is the mean meniscus curvature and r is the radial location. Geometric analysis is used to obtain integral equations to solve for $\overline{\kappa}$ for different shapes of meniscus profiles; for brevity the details for the procedure for calculation of curvature are not presented. Numerical methods also have been used to obtain the meniscus mean curvature as done by Lian et al. (1993), Aveyard et al. (1999), and Willett et al. (2000), who determined the meniscus shape using numerical iterative approaches. This method is relatively complicated, and the gain in accuracy of the maximum magnitude of meniscus force is not significant as compared to the method in which an assumed arc-shaped curve is used.

A concave arc-shaped meniscus for hydrophilic surfaces or a convex arc-shaped meniscus for hydrophobic surfaces is commonly assumed to account for meniscus curvature and is commonly adopted in studies, for example by McFarlane and Tabor (1950), Israelachvili (1992), Tian and Bhushan (1996), Bhushan (1999, 2002, 2003, 2005), Matthewson (1998), Stifter et al. (2000), Bhushan and Peng (2002), and Cai and Bhushan (2006, 2007a,b; 2008a,b). The configuration of arc-shaped meniscus curvature will be discussed in detail in section 3.2.1.4 for a separation of two surfaces from

menisci. For an arc-shaped meniscus curvature, the Kelvin radius r_k (based in Eq. (3.3) to be discussed later) instead of $\overline{\kappa}$ (Eq. (3.1)) is used to find the pressure difference Δp between the inside and outside meniscus. The pressure difference Δp, which is often referred to as capillary pressure or Laplace pressure due to surface tension γ of a formed meniscus, is often estimated using the so-called Laplace–Young equation (Adamson,1990)

$$\Delta p = \gamma\left(\frac{1}{r_1} + \frac{1}{r_2}\right). \tag{3.2}$$

Δp can be negative or positive depending on the surface properties. A hydrophilic surface results in a negative pressure difference, whereas a hydrophobic surface leads to a positive one. In the equation, γ is the surface tension of the liquid and r_1 and r_2 are the meniscus radii in two orthogonal planes; sign is negative for concave-shaped menisci. $(1/r_1 + 1/r_2)^{-1}$ is a so-called Kelvin radius r_k at equilibrium. For the meniscus geometries considered in this paper for flat-on-flat and sphere-on-flat, we assume $|r_2| >> |r_1|$, thus, $r_1 \sim r_k$ and $\Delta p \sim \gamma / r_1$. For an incompressible liquid in equilibrium, the Kelvin radius is related to relative vapor pressure (p/p_0) by the well-known Kelvin equation (Thomson 1870; Adamson, 1990),

$$r_k = \frac{\gamma V}{\Re T \log(p / p_0)}, \tag{3.3}$$

where V is the molar volume of the liquid, $\Re$ is the universal gas constant (8.31 J/molK), T is the absolute temperature, p is the ambient pressure, and p_0 is the saturation vapor pressure at T.

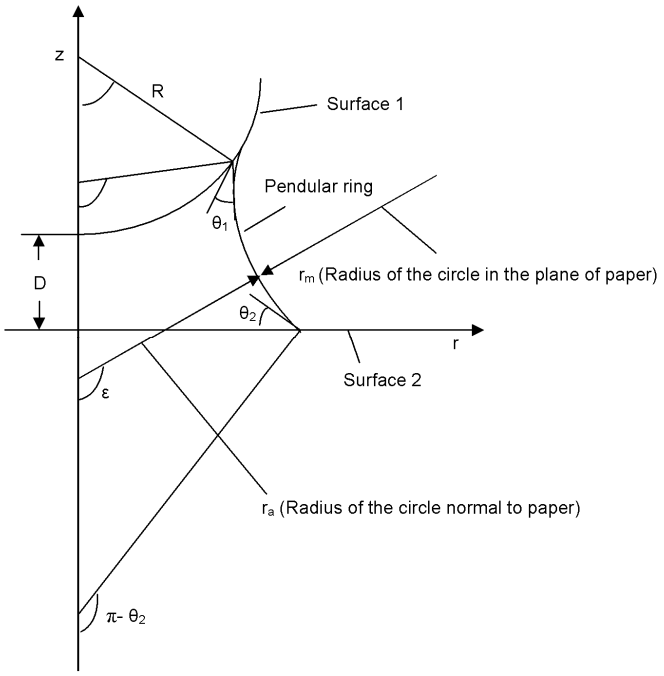

Figure 3.1. The configuration of the meniscus pendular ring geometry for a general situation of sphere on flat [Orr et al., 1975].

3.1.1. Flat-on-flat

The meniscus force due to the formation of a meniscus can be obtained by integrating the Laplace pressure over the meniscus area and adding the surface tension effect acting on the circumference of the interface (Fortes, 1982; Carter, 1988). Figs. 3.2a and 3.2c show the configurations of a meniscus formed two parallel flat hydrophilic surfaces and hydrophobic surfaces, respectively. For two parallel flat surfaces,

$$F_m = F_L + F_T = \iint_{\Omega} \Delta p d\Omega + 2\pi\gamma x_{ni} \sin\theta_{1,2} = \pi x_n^2 \frac{\gamma}{r_k} + 2\pi\gamma x_n \sin\theta_{1,2} \ , \qquad (3.4)$$

where Ω is meniscus area, x_n is the meniscus radius, θ is the contact angle between the liquid and the solid surface, and subscripts 1 and 2 represents the lower and upper surface, respectively. θ_1 or θ_2 in the second expression needs to be used dependent upon the surface being considered for two smooth flat surfaces are shown in Fig. 5a for hydrophilic surfaces, and shown in Fig. 5c for hydrophobic surfaces, to be presented later. The meniscus height h can be calculated, $h = r_k(\cos\theta_1 + \cos\theta_2)$. For a circular meniscus, the Laplace force can be calculated using Eq. (3.4) and the expression for h just presented. The meniscus force is then given as (Cai and Bhushan, 2007a)

$$F_m = \frac{\pi x_n^2 \gamma(\cos\theta_1 + \cos\theta_2)}{h} + 2\pi\gamma x_n \sin\theta_{1,2} . \qquad (3.5)$$

3.1.2. Sphere-on-flat

For a thin liquid film existing between a sphere and a flat surface, three situations are commonly used to calculate meniscus force, namely, a sphere directly sitting on a flat surface without gap (Fig. 3.3a), a sphere close to a flat surface with a gap D (Fig. 3.3b), and a sphere close to a flat surface with continuous liquid film (Fig. 3.3c). The Laplace

force F_L for a sphere with radius R in contact with a plane surface (Fig. 3.3a) is given as (Adamson,1990; Israelachvili, 1992; Bhushan, 1999, 2002)

$$F_L = \iint_\Omega \Delta p \, d\Omega = \pi x_n^2 \frac{\gamma}{r_k} \sim 2\pi R s \frac{\gamma}{r_k} \tag{3.6a}$$

$$\sim 2\pi R r_1 (\cos\theta_1 + \cos\theta_2) \frac{\gamma}{r_k} \tag{3.6b}$$

$$\sim 2\pi R \gamma (\cos\theta_1 + \cos\theta_2) \quad \text{if } r_2 >> r_1 \tag{3.6c}$$

$$\sim 4\pi R \gamma \cos\theta \qquad (\text{if } \theta_1 = \theta_2) \tag{3.6d}$$

This equation has been experimentally verified by McFarlane and Tabor (1950) and Miyoshi et al. (1988). Israelachvili (1992) has reported that this meniscus force expression is valid for water meniscus radii down to 2 nm. For the case of a sphere close to a flat surface with a gap D, $\pi x_n^2 \approx 2\pi R d_0$, $d_0 + D = r_1(\cos\theta_1 + \cos\theta_2)$, and $\phi \approx 0$, where d_0 is the distances (s-D) as shown in Fig. 3.3b. Substituting the two expressions into Eq. (3.6a), the meniscus force for a sphere close to a flat surface can be found (Israelachvili, 1992),

$$F_L = \frac{2\pi R \gamma (\cos\theta_1 + \cos\theta_2)}{1 + (D / d_0)}. \tag{3.7}$$

At D equals 0, maximum attraction occurs, and the situation becomes a sphere-on-flat case without gap, and the equation is the same as Eq. (3.6). For the case of a sphere close to a surface in the presence of a continuous liquid film of thickness h as shown in Fig. 3.3c, the Laplace force can be expressed as

$$F_L = 2\pi R\gamma(1+\cos\theta). \tag{3.8}$$

Another component of the adhesive force arises from the surface tension effect acting on the circumference of the interface. The normal component of the surface tension F_T on the sphere is (Orr, et al., 1975)

$$F_T = 2\pi R\gamma \sin\varphi \sin(\varphi+\theta_2). \tag{3.9}$$

The total meniscus force can be expressed as

$$F_m = F_L + F_T = \Delta p\Omega + 2\pi R\gamma \sin\varphi \sin(\varphi+\theta_2) \tag{3.10}$$

The F_T component is small for small filling angle ϕ as compared to the Laplace pressure contribution. However, F_T can be large for a large contact angle close to 90^o. ϕ is generally small in asperity contacts.

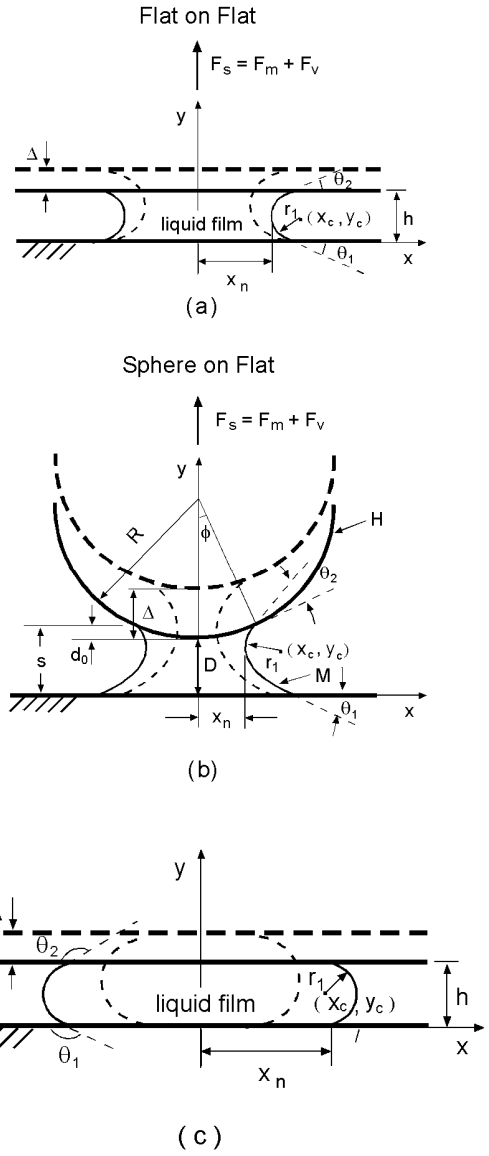

Figure 3.2. Schematic of separation of two smooth surfaces with a meniscus bridge present at the interface, (a) hydrophilic flat on flat surface, (b) hydrophilic sphere on flat surface, and (c) hydrophobic flat on flat surface.

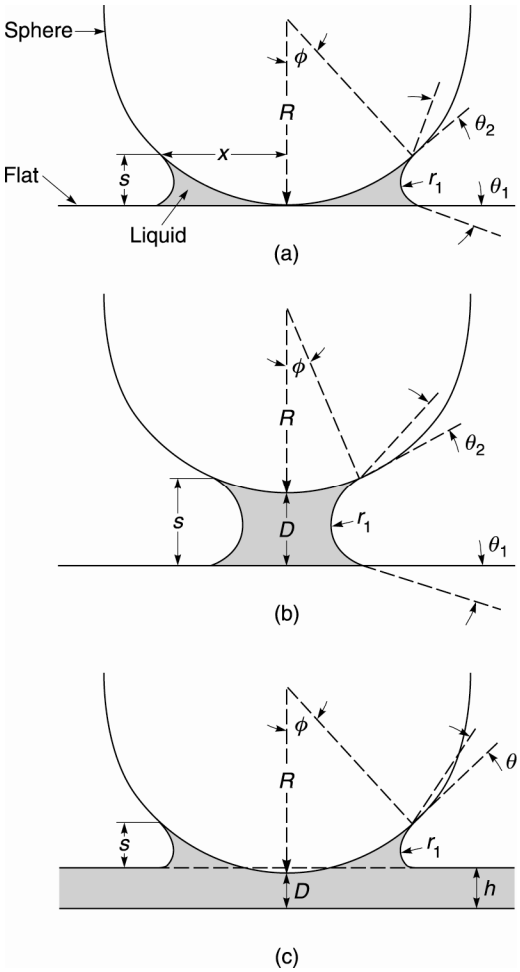

Figure 3.3. Meniscus formation from a liquid condensate at the interface for (a) a sphere in contact with a plane surface, (b) a sphere close to a plane surface, and (c) a sphere close to a plane surface with a continuous film.

3.2. Meniscus and viscous forces during normal separation of meniscus bridges

During the separation of two surfaces, both meniscus and viscous forces operate inside the meniscus. The latter is significant, especially when menisci have a larger size and the separation time is short. Also, asymmetric contact angles and division of meniscus (which are the real cases) can significantly affect the magnitudes and behavior of both meniscus and viscous forces during separation. Fig. 3.4 shows schematically the relationship of meniscus and viscous forces. During separation, the meniscus force continues to decrease with the separation distance because of decrease in the meniscus area, whereas the viscous force continues to increase with the separation distance. Either meniscus or viscous force can be a dominant one during the separation process.
The external force needed to initiate the separation of two surfaces from a liquid film should be larger than the meniscus force. At the break, external force should be larger than combination of meniscus and viscous forces. Dependent upon which of the two forces is larger will affect the break. If the viscous force becomes larger than the meniscus force, the meniscus will eventually break slowly even without an increase in the applied force. However, the time taken to separate the two surfaces would be long. It should be noted that liquids have a limiting shear strength. The viscosity starts to drop above a certain shear stress, and the liquid becomes plastic and can only support a constant stress, known as the limiting shear strength at higher strain rates (Bhushan, 1996b). Therefore viscous force cannot exceed this limiting strength.

In this section, a comprehensive analysis of modeling of the separation of both smooth and rough hydrophilic and hydrophobic surfaces is presented. The effects of separation distance, initial meniscus height, separation time, contact angle, division of menisci, and roughness on both meniscus and viscous forces is reported in detail. The relative roles of these two forces are evaluated during such a process. The assumptions listed in section 3.1 also apply here. Based on these assumptions, Reynolds lubrication theory is applicable during the separation. Since a separation is usually done within a very short time, the evaporation of liquid is assumed to be negligible.

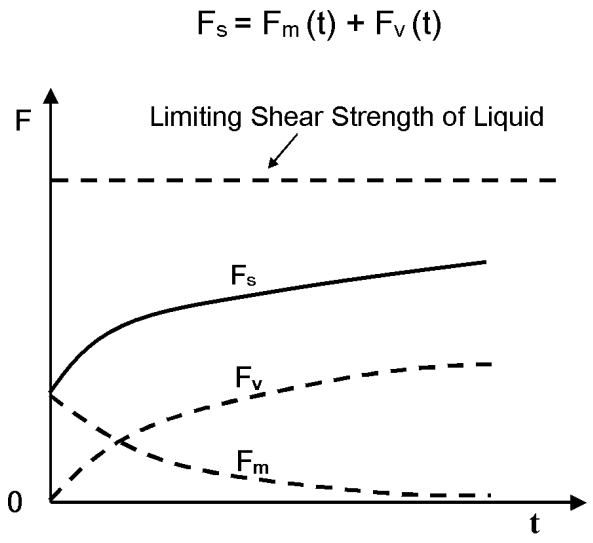

Figure 3.4. Schematic of meniscus and viscous forces contribution to the total adhesive force during separation of two hydrophilic surfaces.

3.2.1. Separation of hydrophilic surfaces

The schematics of separation of two flat surfaces and a sphere and a flat surface with a liquid film in between, is shown in Fig. 3.2. Fig. 3.2a and 3.2b show the configuration of a liquid-solid interface for hydrophilic surfaces, and Fig. 3.2c shows the hydrophobic case. The schematic of menisci formed in between a rough surface and a smooth surface and two smooth surfaces are shown in Fig. 3.5. In the separation of rough surfaces, the surface asperities are assumed to have spherical shapes. Fig. 3.5a shows the distribution of a number of identical spherical asperities N on a flat surface with radius R for each asperity. For the purpose of comparison, the separation of two smooth surfaces with a number of identical menisci is also presented in Fig. 3.5b.

Meniscus and viscous forces are present when separating two surfaces with liquid mediated contacts. Meniscus force F_m is contributed by both Laplace pressure and the surface tension around the circumference, and the force is always attractive for hydrophilic surfaces. The magnitude of the meniscus force depends on liquid and solid properties and the size of the meniscus which relates to the liquid volume and interface geometry. The strength of the viscous force depends on not only the properties of the liquid and solid and the size of the meniscus, but also on the separation time and initial gap between the two bodies.

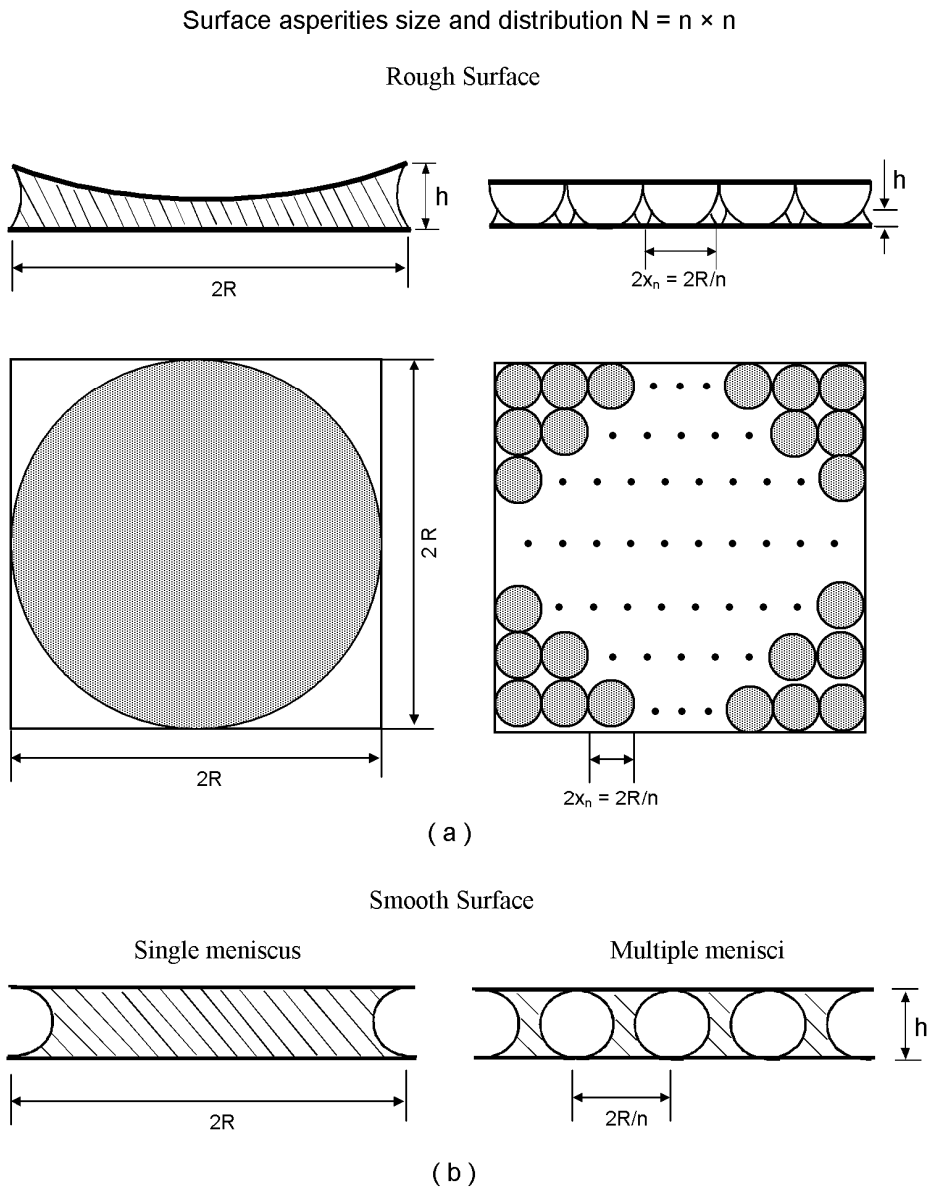

Figure 3.5. Schematics of (a) rough surface asperity distribution for N = 1 × 1 with a single asperity diameter 2R, and N = n × n with a single asperity diameter 2R/n, and (b) a smooth surface with 1 to N = n × n menisci.

3.2.1.1. Meniscus forces

Three situations, namely, flat-on-flat, sphere-on-flat, and rough surfaces, are considered to investigate the meniscus forces.

3.2.1.1.1. Flat-on-flat

The meniscus force due to the formation of a meniscus between two parallel flat surfaces in the normal direction can be obtained by integrating the Laplace pressure over the meniscus area and adding the surface tension effect acting on the circumference of the interface as in Eq. (3.4). For the separation of the two smooth flat surfaces with a circular meniscus and geometry configurations, the meniscus force can be calculated using Eq. (3.5) with the current value of the meniscus radius (Cai and Bhushan, 2007a)

$$F_m = \frac{\pi x_{ni}^2 \gamma (\cos\theta_1 + \cos\theta_2)}{h} + 2\pi\gamma x_{ni} \sin\theta_{1,2} \tag{3.11}$$

where x_{ni} is the meniscus radius at location i during separation. $\theta_{1,2}$ in the second expression in the right hand side corresponds to the contact angle of the liquid on the surfaces being pulled. The consideration for this situation is that the two surfaces are being pulled apart by an external force within a short time; thus the forces on both sides of the liquid bridge can be different during the pull for asymmetric contact angles.

3.2.1.1.2. Sphere-on-flat

The meniscus force on the sphere can be obtained using Eq. (3.10). If $|r_2| >> |r_1|$ does not hold, r_2 may be replaced with the difference between x_c, the center coordinate of the meniscus curve, and r_1. Thus, $r_2 \rightarrow x_c - r_1$ (Stifter et al., 2000),

$$F_m = \pi x_{ni}^2 \gamma \left(\frac{1}{r_{li}} + \frac{1}{x_{ci} - r_{li}} \right) + 2\pi R\gamma \sin\varphi \sin(\varphi + \theta_2) \qquad (3.12)$$

where *i* indicates the calculation step (separation step) in the simulation.

The meniscus force at a given simulation step given in Eq. (3.12) depends on the corresponding instantaneous curvature, which relies on the values of x_{ni}, r_i, and center coordinate x_{ci} of a meniscus instantaneously during separation. These values can be found by using the meniscus profile with given initial conditions and boundary conditions, to be described later. For an arc-shaped meniscus, we apply an approach, to be described in section 3.2.1.4, to obtain the instantaneous curvature during separation.

3.2.1.1.3. Rough surfaces

For the separation of two rough surfaces with N number of identical spherical asperities (Fig. 3.5a) or the separation of two smooth flat surfaces with N number of identical menisci (Fig. 3.5b) arbitrarily distributed on a flat surface without fully occupying the total surface area, one can expect a total meniscus force during initiation of separation, referred to as maximum force, to be

$$(F_m)_{max} = NF_m \ , \qquad (3.13)$$

where F_m is given by Eq. (3.11) for flat smooth surfaces and Eq. (3.12) for rough surfaces with a proper radius x_n or R_n (equals R/n). Here, for instance, for a flat surface with an area 2R×2R, given that the number of asperities is N = n × n (where n is the number of menisci in a row or a column), the radius for each meniscus is R/n for a single asperity (Fig. 3.5a), and x_n/n for flat smooth surface (Fig. 3.5b). The maximum meniscus force is

$$(F_m)_{max} = NF_m(\frac{x_n}{n}) \text{ for smooth surface,}$$

$$(F_m)_{max} = NF_m(\frac{R}{n}) \text{ for rough surface} \quad (3.14)$$

3.2.1.2. Viscous forces

Viscous force occurs due to the viscosity of the liquid when separating two bodies within a short time. One may ignore viscous force for an infinitely long separation time t_s. However, an infinitely long separation time is not practically feasible. Thus, characterization of the relevant viscous force is needed in order to properly estimate the total force needed to separate two surfaces from a liquid mediated contact. In the derivation of the viscous force, Reynolds lubrication theory is assumed to be feasible and is applied to the process of separation (Cai and Bhushan, 2007a). The pressure inside the meniscus bridge consists of horizontal pressure gradients, whereas the pressure is constant in any vertical plane inside a meniscus bridge and at the outside of a meniscus ring $r = x_{ni}$ (liquid-air interfacial boundary, which is exposed in ambient), $p(x_{ni}) = p$, the ambient pressure.

3.2.1.2.1. Flat on flat

For separation of two smooth flat surfaces for a liquid with kinematic viscosity η, the equation for the viscous force for separation of two flat surfaces has been derived by Cai and Bhushan (2007a) by using Reynolds lubrication equation with a cylindrical coordinate system (e.g., Hocking, 1973)

$$\frac{\partial}{\partial r}(rh^3\frac{\partial p}{\partial r}) = 12\eta r\frac{dh}{dt} \quad (3.15)$$

where h is the separation distance and r is an arbitrary distance in the central plane of the meniscus in the direction of separation where separation occurs. Integrating the equation above with r and applying the boundary condition, $p(x_{ni}) = p$, the pressure difference at arbitrary radius *r* within a meniscus can be obtained,

$$\Delta p = \frac{3\eta}{h^3}(r^2 - x_{ni}^2)\frac{dh}{dt} \tag{3.16}$$

The pressure is maximum at the center of a meniscus and it is equal to ambient pressure at the boundary. An average pressure difference is one half of the maximum pressure difference at the center of a meniscus

$$\Delta p_{avg} = -\frac{3\eta}{2h^3} x_{ni}^2 \frac{dh}{dt} \tag{3.17}$$

The viscous force can be calculated by multiplying the average pressure difference based on the above equation with the meniscus area in the central plane in the direction of separation. The viscous force at a given separation distance can be expressed as

$$F_V = \int_0^{x_{ni}} 2\pi \Delta p_{avg} r dr = -\frac{3\pi\eta}{2h^3} x_{ni}^4 \frac{dh}{dt} \tag{3.18}$$

By integrating the above equation during the separation until break, one obtains the viscous force at the break point (Cai and Bhushan, 2007a)

$$F_V = \frac{3\pi\eta x_{ni}^4}{4t_s}\left(\frac{1}{h_s^2} - \frac{1}{h_0^2}\right) \tag{3.19}$$

where t_s is the time to separate two bodies, h_s is the break point. One may take $h_s = \infty$ when separation occurs, however, this may lead to an over estimation of the real viscous force since a meniscus bridge may break very quickly when it is small and the meniscus radius is comparable to its height. Thus, the point of break h_s should be determined to give a reasonable estimate of the viscous force. Here, h_s is the distance corresponding to a zero meniscus neck thickness (for the purpose of simulation) during separation.

3.2.1.2.2. Sphere-on-flat

Similar to the approach in the previous section, for the calculation of viscous forces during separation of a sphere and a flat surface, h in the Reynolds equation Eq. (3.15) is replaced with H(r) (Cai and Bhushan, 2007a)

$$\frac{\partial}{\partial r}\left\{ r[H(r)]^3 \frac{\partial p}{\partial r} \right\} = 12\eta r\dot{D} \tag{3.20}$$

where D is separation distance, and $H(r)$ is the shape of the upper boundary at radius r within x_{ni}, $H(x_{ni}) = x_{ni}^2/(2R) + D$. At the outside boundary x_{ni}, $p(x_{ni}) = p$. Integrating Eq. (3.20) and applying this boundary condition, the pressure difference Δp is obtained,

$$\Delta p = 3\eta R\dot{D}\left(\frac{1}{H^2(r)} - \frac{1}{H^2(x_{ni})}\right) \tag{3.21}$$

The viscous force at a given separation distance can be found by substituting the expression for H(r) and $H(x_{ni})$ and integrating Δp over the meniscus area,

. $$F_V = 6\pi\eta R^2\left[1-\frac{D}{H(x_{ni})}\right]^2\frac{1}{D}\frac{dD}{dt} \tag{3.22}$$

$H(x_{ni})$ changes with separation and needs to be calculated instantaneously. For $R >> x_{ni}$, the volume of the meniscus is

$$V = \int_0^{x_{ni}} 2\pi r H(r)dr = \pi R\left[H(x_{ni}^2) - D^2\right] \tag{3.23}$$

The conservation of volume leads to V_m (i) = V_m (0) (the meniscus volume at the separation step i equals the initial volume), thus, the $H(x_{ni})$ at a given separation distance can be found

$$H^2(x_{ni}) = H^2(x_{n0}) - D_0^2 + D^2 \tag{3.24}$$

where x_{n0} and D_0 are initial meniscus radius and gap, respectively. Substituting Eq. (3.24) into Eq. (3.22) and integrating the equation over time, the viscous force at a given separation distance can be obtained

$$F_V = \frac{1}{t_s}\int_{D_0}^{D_s} 6\pi\eta R^2\left[1-\frac{D}{\sqrt{H^2(x_{n0}) - D_0^2 + D^2}}\right]^2\frac{1}{D}dD \tag{3.25}$$

where D_s is the distance when separation occurs. Separation occurs when a meniscus neck radius equals zero. Further integrating Eq. (3.25) during the separation until break, one obtains the viscous force at the break point (Cai and Bhushan, 2007a)

$$F_V = \frac{6\pi\eta R^2}{t_s} \ln \frac{D_s \left[D_0 + H(x_{n0})\right]^2 \sqrt{H(x_{n0})^2 - D_0^2 + D_s^2}}{D_0 H(x_{n0}) \left[D + \sqrt{H(x_{n0})^2 - D_0^2 + D_s^2}\right]^2} \tag{3.26}$$

When D_s approaches infinite, Eq. (26) is reduced to

$$F_V = \frac{6\pi\eta R^2}{t_s} \ln[\frac{H(x_{n0})}{2D_0}] \tag{3.27}$$

3.2.1.2.3. Rough surface

Similar to the calculation of meniscus force for the rough surface case, for the separation of two smooth flat surfaces with N number of identical menisci, or separation of two rough surfaces with N number of identical spherical asperities arbitrarily distributed on a flat surface without fully occupying the total surface area (Fig. 3.5), one can expect a maximum viscous force

$$(F_v)_{max} = NF_v \tag{3.28}$$

where, F_v is given by Eq. (3.19) for flat smooth surfaces, and by Eq. (3.26) for rough surfaces.

For the case of N number of menisci or the spherical asperities fully occupying the total surface area, the maximum viscous force is (Cai and Bhushan, 2008a)

$$(F_v)_{max} = NF_v\left(\frac{x_{ni}}{n}\right) \quad \text{for flat smooth surface, and}$$

$$(F_v)_{max} = NF_v\left(\frac{R}{n}\right) \quad \text{for rough surface} \tag{3.29}$$

3.2.1.3. Division of menisci

Lee et al. (2002) conducted an experiment and showed that a liquid bridge can be split or merged by using electrowetting on dielectric materials, which indicates the feasibility of division of menisci and its potential application, like micromanipulation. In this section, the effects of division of menisci on both meniscus and viscous forces are presented. Fig. 3.6 shows the division of a big meniscus bridge into N number of meniscus bridges with equal areas. In the model, a large meniscus with a known volume v_0 is first assumed, and then, it is divided into N number of smaller identical menisci. One can expect that the volume of each smaller meniscus is v_0/N. Since for a given physical contact interface and a known liquid volume the contact angles remain the same, for a given meniscus height h with fixed gap between two surfaces, the scaling of volume is equivalent to the scaling of liquid-substrate contact area; thus, each of the smaller menisci will have a meniscus area A_{total}/N. Since originally the meniscus area A_{total} equals πx_{ni}^2, the meniscus area for each of the identical smaller menisci is

$$A_N = \frac{A_{total}}{N} = \pi\left(\frac{x_{ni}}{\sqrt{N}}\right)^2 \tag{3.30}$$

This indicates that when a large meniscus is divided into N identical smaller menisci, the neck radius will decrease by the order of $\sqrt{N}$. The meniscus and viscous forces for each of the smaller menisci can be found by substituting this relationship into Eqs. (3.11) and (3.19)

$$F_{m-N} = \frac{\pi x_{ni}^2 \gamma(\cos\theta_1 + \cos\theta_2)}{hN} + 2\pi\gamma \frac{x_{ni}}{\sqrt{N}} \sin\theta_{1,2} \tag{3.31}$$

$$F_{v-N} = \frac{3\pi\eta x_{ni}^4}{4N^2 t_s}\left(\frac{1}{h_{s-N}^2} - \frac{1}{h_0^2}\right) \tag{3.32}$$

where h_{s-N} represents the break distance for a smaller meniscus.

The total meniscus and viscous forces due to the division can be calculated by multiplying Eqs. (3.31) and (3.32) by the number of divisions N (Cai and Bhushan, 2007b)

$$F_{m-NT} = \frac{\pi x_{ni}^2 \gamma(\cos\theta_1 + \cos\theta_2)}{h} + 2\sqrt{N}\pi\gamma x_{ni} \sin\theta_{1,2} \tag{3.33}$$

$$F_{v-NT} = \frac{3\pi\eta x_{ni}^4}{4Nt_s}\left(\frac{1}{h_{s-N}^2} - \frac{1}{h_0^2}\right) \tag{3.34}$$

"Force scaling" effects can be obtained from the above two equations. Eq. (3.33) indicates the total meniscus force increases with an increase in $\sqrt{N}$ due to the division, given that the meniscus radius is very small.

$$F_{m-NT} \sim \sqrt{N} F_{m-N} \tag{3.35}$$

For the viscous force, Eq. (3.33) shows that the resultant viscous force depends on the break distance also. The break distance can be determined using the procedures described in section 3.2.1.4. However, if we assume the break distance is much larger than the initial meniscus height, then the absolute magnitude of Eq. (3.34) reduces to (Cai and Bhushan, 2007b)

$$F_{v-NT} = \frac{3\pi\eta x_{ni}^4}{4Nt_s}\frac{1}{h_0^2} \sim \frac{F_V}{N} \tag{3.36}$$

Thus, one can expect that the viscous force decreases by an order of inverse the number of division (1/N) due to the division.

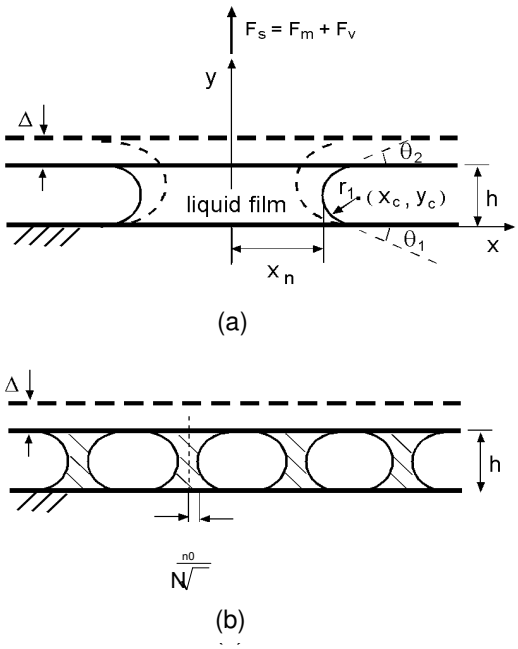

Figure 3.6. Schematic of separation of two smooth surfaces with (a) one meniscus bridge, and (b) n meniscus bridges with equal areas, present at the interface.

3.2.1.4. Meniscus curvature

A meniscus breaks at a certain distance, called the break point, during separation. Numerically, one may consider that point occurs at infinite distance. However, this may lead to an overestimation of the real viscous force since a meniscus bridge may break very quickly when it is small and the meniscus radius is comparable to its height. Thus, the break point should be determined to give a reasonable estimate of the viscous force. For simulation purposes, the break distance can be assumed to be the distance corresponding to a zero meniscus neck thickness during separation. The instantaneous meniscus and viscous forces discussed previously depend on the solving of the break point and meniscus radius x_n, which in turn rely on initial conditions and boundary conditions, and the instantaneous meniscus curvature needs to be calculated during the process of separation. The meniscus profile can be found by solving the Laplace-Young equation as discussed in section 3.1. For simplicity, a concave arc-shaped meniscus is assumed to account for meniscus curve due to hydrophilic surfaces, and a convex arc-shaped curve for hydrophobic surfaces. For a concave arc-shaped meniscus, we have applied a simple approach to effectively capture the curvature during separation and avoid the complexity of handling elliptic integrals (Cai and Bhushan, 2007a). For a hydrophobic surface, one may apply a similar approach with slight modifications to characterize the meniscus curvature.

Let H and M denote the shape functions of the upper boundary and the meniscus as shown in Fig. 3.2b. H and M can be chosen as needed. If the shape of H is spherical, it may be expressed as (Stifter et al., 2000)

$$H : H(r = x) = \frac{x^2}{2R} + D \tag{3.37}$$

and if the meniscus shape is an arc, M may be expressed as

$$M : (x - x_c)^2 + (y_m - y_c)^2 = r_{1i}^2 \tag{3.38}$$

The geometry configurations satisfy a set of boundary conditions

$$M: \quad \left|\frac{dy_m}{dx}\right|_{y_m=0} = \tan\theta_1$$

$$y_c = r_{1i}\cos(\theta_1)$$

$$H \sim M: \quad \frac{dy_m}{dx} = \tan\left[\theta_2 + \arctan\left(\frac{dH(x)}{dx}\right)\right]$$

$$y_m = H(r = x) \tag{3.39}$$

One more condition is needed to fully constrain the problem and uniquely determine the meniscus curvature instantaneously. For incompressible fluid, conservation of volume gives

$$V_i = V_0 \tag{3.40}$$

The volume can be found by integrating the whole area enclosed by H, M and the two coordinate axes, and the magnitude of V_0 can be calculated from initial conditions. The instantaneous values of x_{ni}, r_i, x_{ci}, and y_{ci} can be determined with the boundary conditions and conservation of volume. Correspondingly, the instantaneous meniscus curvature and meniscus force can be calculated. For separation of two parallel flat surfaces, one sets H(x) = h, otherwise, the shape function H(r) should be defined. The case of H(r) = h corresponds to a constant separation speed. It is noted that $x = x_{ni}$ in a separation simulation.

3.2.2. Separation of hydrophobic surfaces

Convex-shaped menisci will be formed between two hydrophobic surfaces with the presence of a liquid film. Due to the positive Kelvin radius, the meniscus force exhibits a repulsive nature in general; however, a slightly attractive property was also observed under certain conditions in separation, to be presented later (Cai and Bhushan, 2008a). The assumptions for the separation of hydrophilic surfaces are applied here for separation of hydrophobic surfaces, except that a convex shape is used for the formed menisci. For simplicity, a convex-shaped arc is used to estimate both meniscus and viscous forces in separation. The formulations of both meniscus and viscous forces are the same as that for hydrophilic surfaces. However, due to the positive Kelvin radius, the center coordinate y_c in Eq. (3.39) needs to be modified when calculating the meniscus force,

$$y_c = r_{1i}\cos(\pi - \theta_1) \tag{3.41}$$

3. 2.3. Validation of the model

It is noted that the equations for calculation of both meniscus and viscous forces during normal separation in this paper are analytically formulated. The equations to calculate meniscus forces are available in the literature, for example used by Orr et al. (1975), Fortes (1982), Carter (1988), Adamson (1990), Israelachvili (1992), and Bhushan (1999, 2002). The equation presented here to calculate the viscous forces during normal separation two flat surfaces is also analytically formulated (Cai and Bhushan, 2007a). It is consistent with that developed by Bowden and Tabor (1950) and Bhushan (1999, 2002) for the case of during break. The equation to calculate the viscous forces during normal separation of a sphere and a flat surface for an arbitrary break distance (Cai and Bhushan, 2007a) is also analytically formulated and has never been reported before. For an assumption of an infinite break distance, it is the same as developed by Matthewson

(1988). The simplest way to verify the numerical procedure to solve analytical equations is to calculate some characteristic values and compare them with the numerical results, which has been done. A more complicated situation is also used here as an example. For instance, the break distances for separation of a sphere and a flat surface with a gap 1 nm for initial meniscus heights 2, 3, 4, 5, 6 nm are 3.9×10^4, 5.8×10^4, 7.3×10^4, 8.7×10^4, and 9.9×10^4 nm, respectively. Substituting these values into Eq. (3.26), the viscous forces can be found to be 0.1976, 0.4826, 0.7487, 0.9861, and 1.1974 nN. These values are the same as the numerical results output from the model and can be read directly from Fig. 3.11b, to be presented later.

3. 2.4. Representative results

Separation of two hydrophilic and hydrophobic surfaces relying on symmetric and asymmetric contact angles with various initial meniscus heights is analyzed with respect to meniscus and viscous forces. The two forces are calculated based on the curvatures during separation. For simulation purposes, a meniscus break at a zero meniscus neck radius is assumed though this is not true practically, and it may break at a certain critical separation distance (Singh et al., 2006), and the forces disappear at the break point. The force needed to overcome a meniscus force is the meniscus force at equilibrium at the beginning, whereas the force needed to overcome a viscous force (due to viscosity) equals the force resulting from the break of a meniscus bridge (which occurs at the break point).

In the analysis for separation of two flat surfaces, the dimensionless meniscus and viscous forces are defined as follows to eliminate effects of the contact angles due to surface property and the liquid surface tension and viscosity for the purpose of comparison.

$$F_m^* = \frac{1}{\pi x_{n0}\gamma(\cos\theta_1 + \cos\theta_2)} F_m \tag{3.42}$$

$$F_v^* = \frac{4t_s h_0^2}{3\pi\eta x_{n0}^4} F_v \tag{3.43}$$

The effects of rough surface based on the numerical models are also presented. In the analysis, liquid bridges formed from water are evaluated. The meniscus curvatures presented as examples are generated based on an initial h_0 = 2 nm for separating two flat surfaces, and initial gap D_0 = 0 and 1 nm for the cases of separating a sphere and a flat surface. An initial meniscus radius of 100 nm is used in the smooth flat-on-flat case, and an asperity radius R of 100 nm for the sphere-on-flat case in the simulations. These values selected here are representative for magnetic rigid disk drives to be discussed later in the Applications section. An initial nominal area of 100 μm by 100 μm with a larger initial meniscus height 100 nm is used in the study of roughness effect. The forces calculated during separation are based on various initial meniscus heights from 2 nm to 6 nm. Contact angles 0^o and 90^o corresponding to 0.001^o and 89.999^o for hydrophilic surface, and 90^o and 180^o corresponding to 90.001^o and 179.999^o for hydrophobic surface, respectively, are used to avoid singularities. The separation time t_s used in the study is 0.1μs owing to the real separation time of a diesel fuel injector to be discussed later in the Application section. Fig. 3.7 shows examples of instantaneous meniscus curvatures during the separation of two liquid mediated surfaces for hydrophilic (Fig. 3.7a) and hydrophobic surfaces (Fig. 3.7b). It is shown that for a given set of contact angles and a given initial meniscus height, asymmetric contact angles lead to a faster break of meniscus for both hydrophilic and hydrophobic surfaces. Hydrophobic surfaces with asymmetric contact angles have the shortest break distance as compared to the corresponding hydrophilic surfaces.

Examples of instantaneous meniscus curvatures during the separation of a sphere and a flat hydrophilic surface are shown in Fig. 3.8. Fig. 3.8a shows the case in which a sphere and the flat surface have no initial gap, whereas, Fig. 3.8b has a 1 nm initial gap. It is easily observed that the one with a gap leads to a quick break of a meniscus bridge. These observed differences will eventually affect the forces, as we can see from the data to be presented later.

Dimensionless (identified with *) and dimensional meniscus and viscous forces versus relative separation Δ (from initial distance h_0 to $h_0 + \Delta$) for separating two parallel surfaces and a sphere and a flat surface from various initial meniscus heights $h_0 = 2 - 6$ nm with symmetric and asymmetric contact angles are reported. The dimensionless figures presented are for the purpose of generalization and for general use since the effects of liquid and surface properties have been eliminated. One can obtain the appropriate force magnitude from these figures for various surfaces and liquids by simply multiplying the surface tension, viscosity, and contact angle effects. Since the dimensionless and dimensional figures show the same trends, the discussion will mainly focus on the dimensional ones for brevity.

3.2.4.1. Effect of separation distance

For separations of both hydrophilic and hydrophobic flat surfaces, the effects of separation on meniscus and viscous forces can be observed in Figs. 3.9 and Fig. 3.10. Fig. 3.9 shows dimensionless and dimensional meniscus forces versus relative separation Δ for separation of two flat surfaces from various initial meniscus heights $h_0 = 2 - 6$ nm. The data with contact angles $\theta_1 = \theta_2 = 60^o$ and $\theta_1 = \theta_2 = 120^o$ is shown in Fig. 3.9a, and the data with contact angles $\theta_1 = 0^o$, $\theta_2 = 60^o$; and $\theta_1 = 180^o$, $\theta_2 = 120^o$ is shown in Fig. 3.9b. Fig. 3.10 shows dimensionless and dimensional viscous forces versus relative separation Δ for separation of two flat surfaces in the same conditions. The dimensionless viscous forces for contact angles $\theta_1 = \theta_2 = 60^o$ and $\theta_1 = 0^o$, $\theta_2 = 60^o$ are shown in Fig. 10a, and the corresponding dimensional data is shown in Fig. 3.10b. Fig. 3.10c and Fig. 3.10d show the same data as compared to Figs. 3.10a and 3.10b, but the contact angles are $\theta_1 = \theta_2 = 120^o$ and $\theta_1 = 180^o$, $\theta_2 = 120^o$, respectively. The results show meniscus force decreases with an increase in separation distance, whereas the viscous force has an opposite trend. These trends show the forces are distance dependent. Attractive and repulsive meniscus forces are observed for hydrophilic and hydrophobic surfaces, respectively. In either case, both types of meniscus forces and viscous forces change rapidly at the beginning. This trend is the same for both the dimensionless and dimensional results. The larger rate of change in the force at the beginning of separation

is due to the larger rate of change in meniscus volume at the beginning and the rate of change becomes gradual thereafter (Fig. 3.7 and 3.8). The larger rate of change in volume leads to a relatively larger decrease in pressure difference during separation at a constant speed.

For the case of separating a sphere and a flat surface with and without initial gap D_0, the force-distance relationship can be observed from Fig. 3.11. Fig. 3.11a and b show the dimensionless meniscus and viscous force for the cases of with and without gap respectively, and Fig. 3.11c and d show the corresponding dimensional meniscus and viscous forces for the two cases. The force-distance relational trends observed in the separation of two flat surfaces are also true here. The effects of D_0 on both forces and break point can be observed. It is easy to identify that a zero D_0 leads to higher meniscus and viscous forces and slower break of a meniscus bridge at the same initial meniscus height s_0 as compared to a nonzero D_0 situation. For different initial meniscus height s_0, it is observed that meniscus force exhibits some differences between with and without D_0. A smaller s_0 leads to a larger meniscus force for zero D_0. It is found that this trend holds for D_0 less than 1 nm; however, for D_0 larger than 1 nm, a smaller s_0 leads to a lower meniscus force. This indicates an initial separation D_0 between the sphere and the flat surface plays an important role in affecting meniscus force.

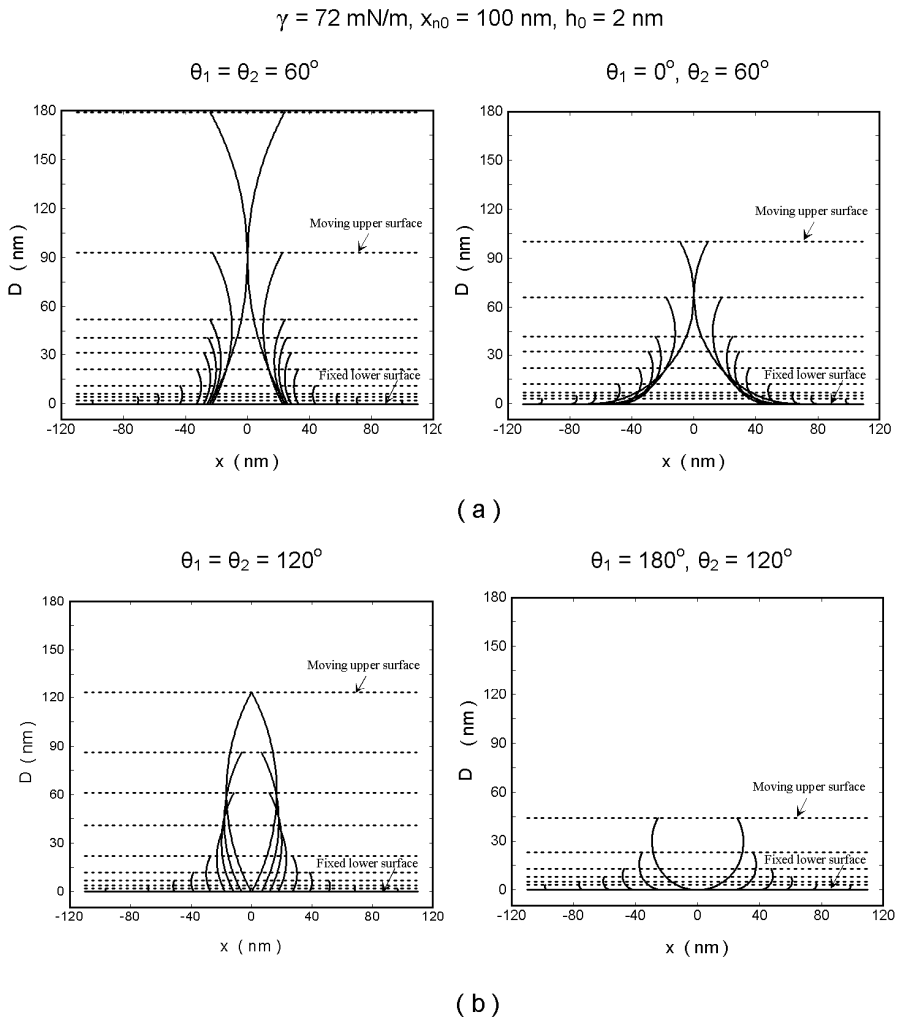

Figure 3.7. Meniscus curvatures when separating two parallel flats with initial meniscus height h_0 = 2 nm, γ = 72 mN/m, x_{n0} = 100 nm, and contact angles, (a) $\theta_1 = \theta_2 = 60^o$ and $\theta_1 = 0^o$, $\theta_2 = 60^o$, and (b) $\theta_1 = \theta_2 = 120^o$ and $\theta_1 = 180^o$, $\theta_2 = 120^o$ [Cai and Bhushan, 2008a].

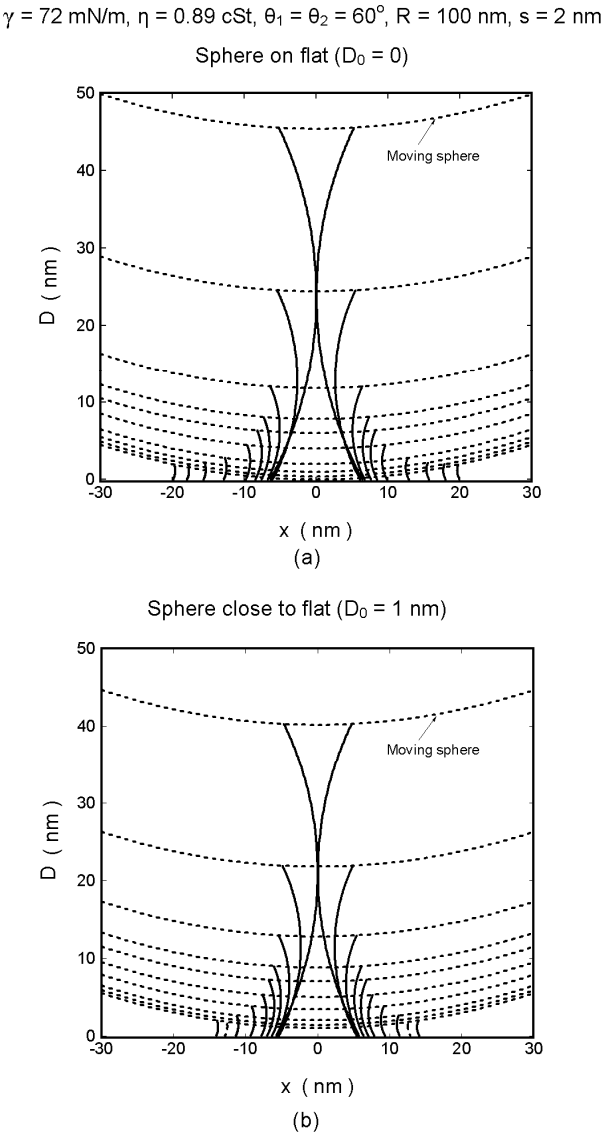

Figure 3.8. Meniscus curvatures when separating a sphere and a flat surface with initial meniscus height s_0 = 2 nm for separation time t_s = 0.1 μs with γ = 72 mN/m, contact angle $\theta_1 = \theta_2 = 60^o$, and two initial sphere to flat surface distances, (a) D_0 = 0, and (b) D_0 = 1 nm [Cai and Bhushan, 2007a].

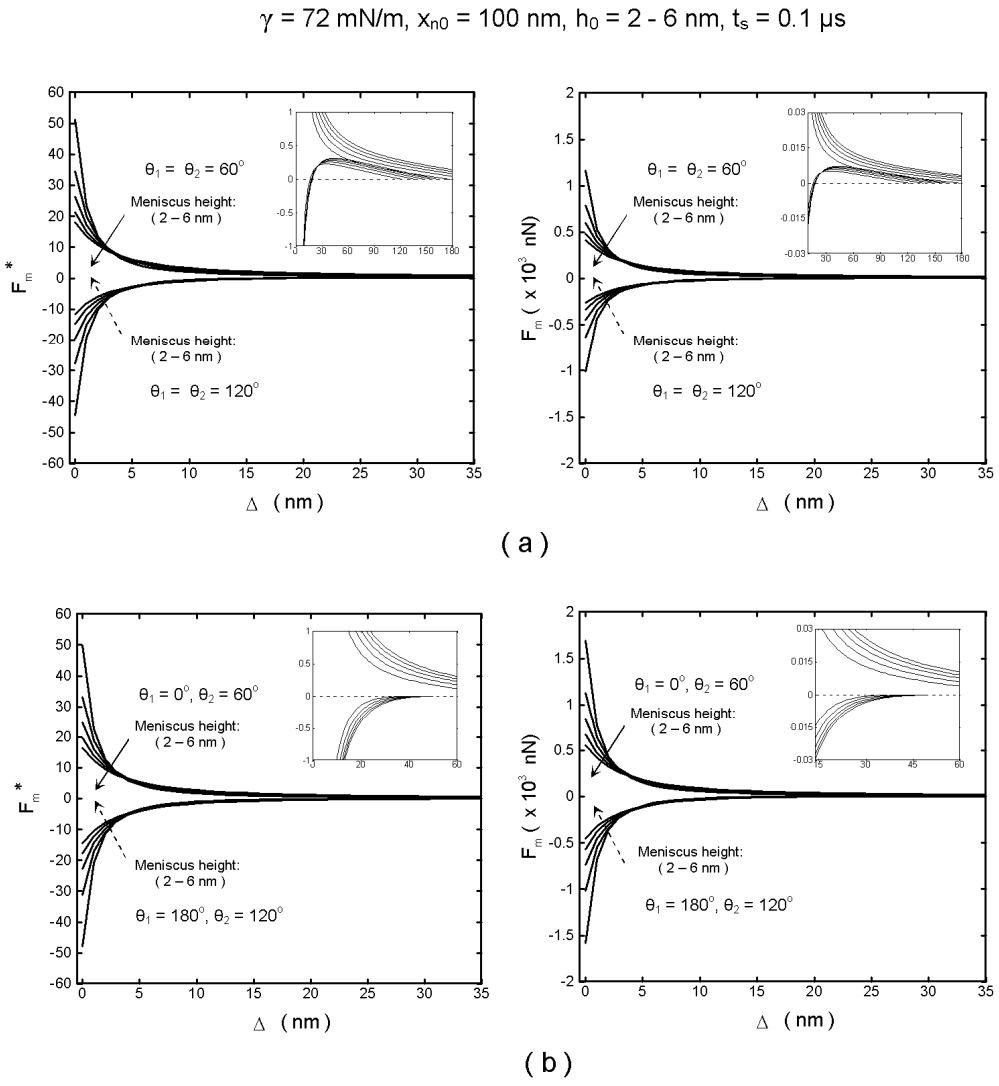

Figure 3.9. Dimensionless and dimensional meniscus forces versus separation distance during separation of two flat surfaces for various initial meniscus heights (h_0) = 2 - 6 nm for a separation time t_s = 0.1 μs with γ = 72 mN/m, x_{n0} = 100 nm, and contact angles (a) $\theta_1 = \theta_2 = 60^o$ and $\theta_1 = \theta_2 = 120^o$, and (b) $\theta_1 = 0^o$, $\theta_2 = 60^o$; and $\theta_1 = 180^o$, $\theta_2 = 120^o$. The small figures are zoomed in figures [Cai and Bhushan, 2008a].

3.2.4.2. Effect of initial meniscus height

Initial meniscus height h_0 affects both meniscus force and viscous force for either hydrophilic or hydrophobic surfaces, which can be observed from Figs. 3.9 to 3.11. For the separation of two flat surfaces, it is shown that a lower meniscus height leads to a larger meniscus force (attractive or repulsive) and viscous force. The increase of h_0 leads to a decrease in the magnitudes of these forces. The dimensionless and dimensional results have the same trend (Figs. 3.9 and 3.10). This is because at a fixed meniscus area, a higher h_0 results in a larger Kelvin radius and lower absolute pressure difference Δp, and thus, lower meniscus force (attractive or repulsive). The trend of decrease in the forces with an increase in h_0 for viscous and meniscus forces is expected since the viscous force is a function of the inverse of the square of the meniscus height as shown in Eq. (3.19), and meniscus force is a function of the inverse of the meniscus height as shown in Eq. (3.11). An increase in initial meniscus height leads to the critical meniscus area moving to a larger value since viscous force decreases much faster than meniscus force with an increase in initial meniscus height. It is observed that h_0 plays a significant role in the theoretical break point. Smaller h_0 leads to a quick break of the meniscus. This is because the meniscus bridge with smaller h_0 has a smaller liquid volume for a given initial meniscus area. Both meniscus and viscous forces disappear at the break point. As compared to hydrophilic surfaces, the effect of initial meniscus height h_0 to the break of meniscus becomes less significant for hydrophobic surfaces (Fig. 3.10). The initial meniscus height affects the critical meniscus area as well. An increase in initial meniscus height leads to an increase in critical meniscus area. This is because viscous force increases faster with the decrease in initial meniscus height than meniscus forces.

For the case of separating a sphere and a flat surface, the two situations, with and without gap, lead to different results for meniscus force as shown in Fig.3.11 (a-b) (dimensionless) and Fig. 3.11 (c-d) (dimensional). It is easy to identify that a smaller initial s_0 has a larger meniscus force for $D_0 = 0$. This is expected because a smaller s_0 corresponds to a smaller Kelvin radius, thus a higher meniscus force. However, a non-zero D_0 situation is the opposite. One explanation is that the positive contribution to meniscus force from increasing free surface energy is larger than the negative effect from

increasing a Kelvin radius when D_0 reaches a certain level. For viscous forces, introducing non-zero D_0 leads to a lower viscous force, which is true for various values of s_0 = 2 - 6 nm. A smaller s_0 corresponds to a lower viscous force as shown in Fig. 3.11. The behavior is expected since for the same s_0, introducing D_0 results in a smaller liquid-solid interaction area, and for the same D_0, a higher s_0 leads to a larger liquid-solid interaction area. It is also observed that both meniscus force and viscous force disappear (break point) sooner with a smaller s_0. This is because the meniscus bridge with smaller s_0 has a smaller liquid volume for a given initial meniscus area.

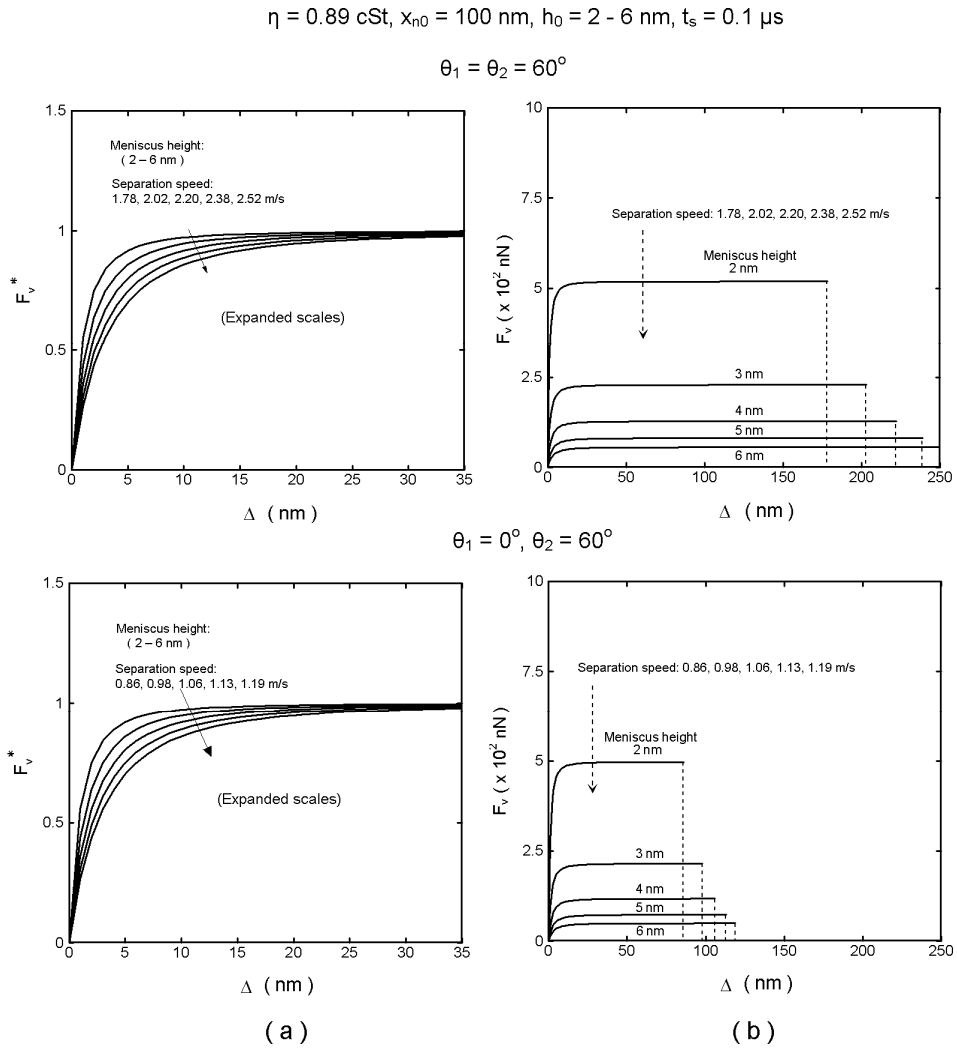

Figure 3.10. Viscous forces during separation of two flat surfaces for various initial meniscus heights (h_0) = 2 - 6 nm for a separation time t_s = 0.1 μs with η = 0.89 cSt, x_{n0} = 100 nm, and contact angles, (a) dimensionless viscous force vs separation for $\theta_1 = \theta_2 = 60^o$ and $\theta_1 = 0$, $\theta_2 = 60^o$, (b) dimensional viscous force vs separation for $\theta_1 = \theta_2 = 60^o$ and $\theta_1 = 0$, $\theta_2 = 60^o$, (c) dimensionless viscous force vs separation for $\theta_1 = \theta_2 = 120^o$ and $\theta_1 = 180^o$, $\theta_2 = 120^o$, (d) dimensional viscous force vs separation for for $\theta_1 = \theta_2 = 120^o$ and $\theta_1 = 180^o$, $\theta_2 = 120^o$ [Cai and Bhushan, 2007a, b; 2008a].

Figure 3. 10. (continued)

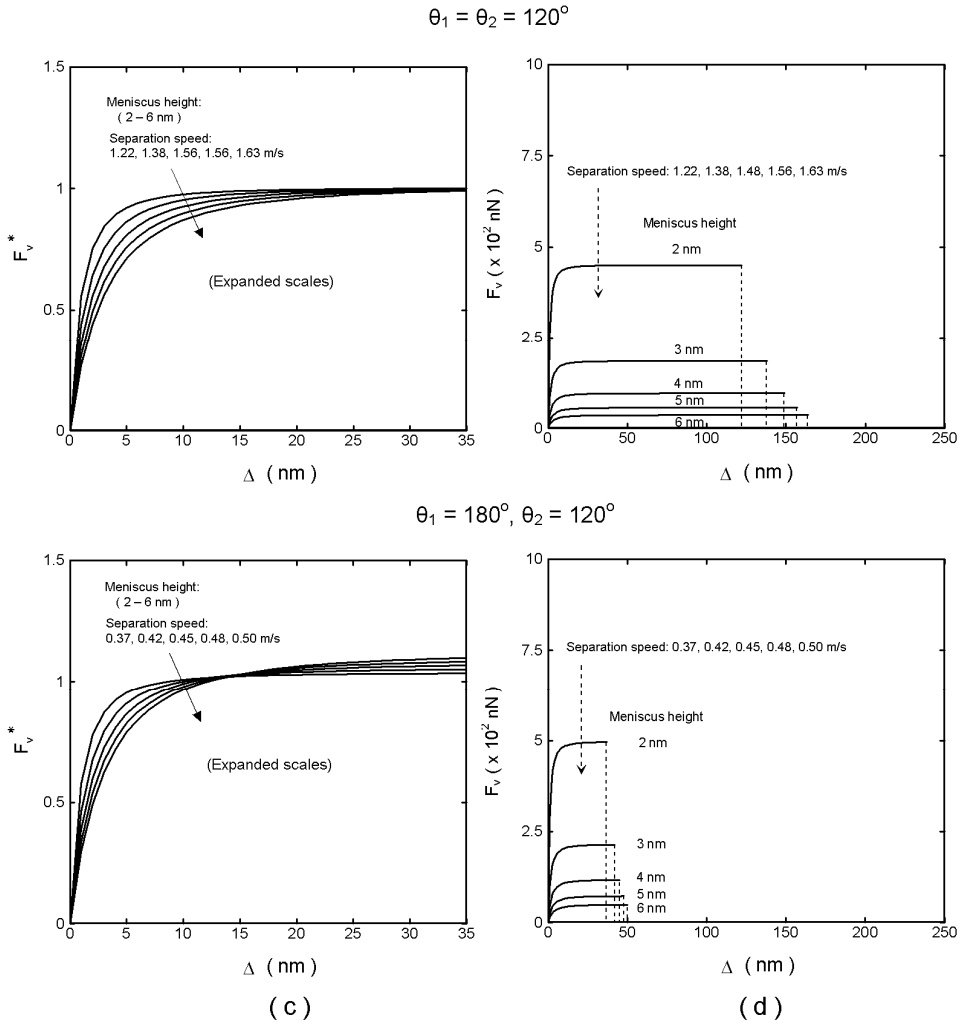

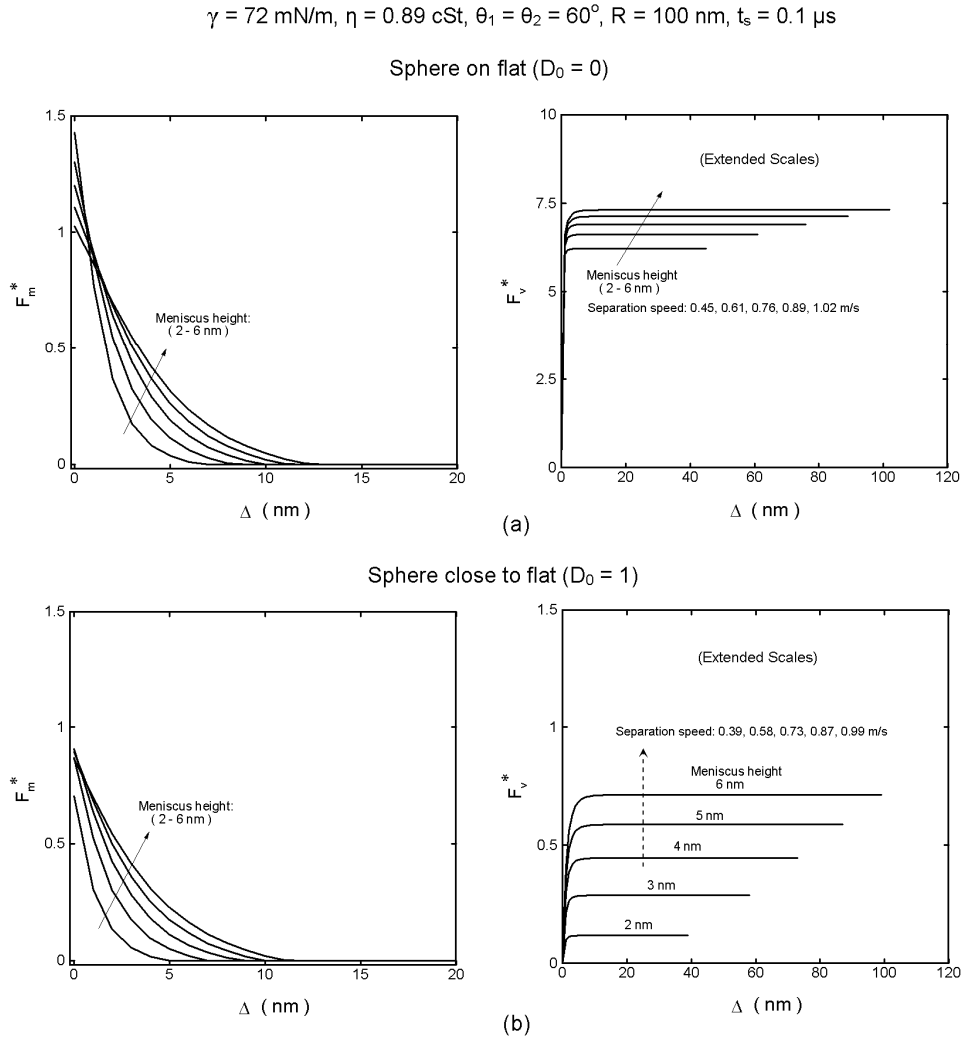

Figure 3.11. Meniscus and viscous forces versus separation distance during separation of a sphere and a flat surface from various initial meniscus heights (s_0) = 2 - 6 nm for separation time t_s = 0.1 μs with γ = 72 mN/m, contact angle $\theta_1 = \theta_2 = 60^o$, and two initial sphere to flat surface distances, (a) dimensionless forces with D_0 = 0, and (b) dimensionless forces with D_0 = 1 nm, (c) dimensional forces with D_0 = 0, and (d) dimensional forces with D_0 = 1 nm [Cai and Bhushan, 2007a].

Figure 3.11. (continued)

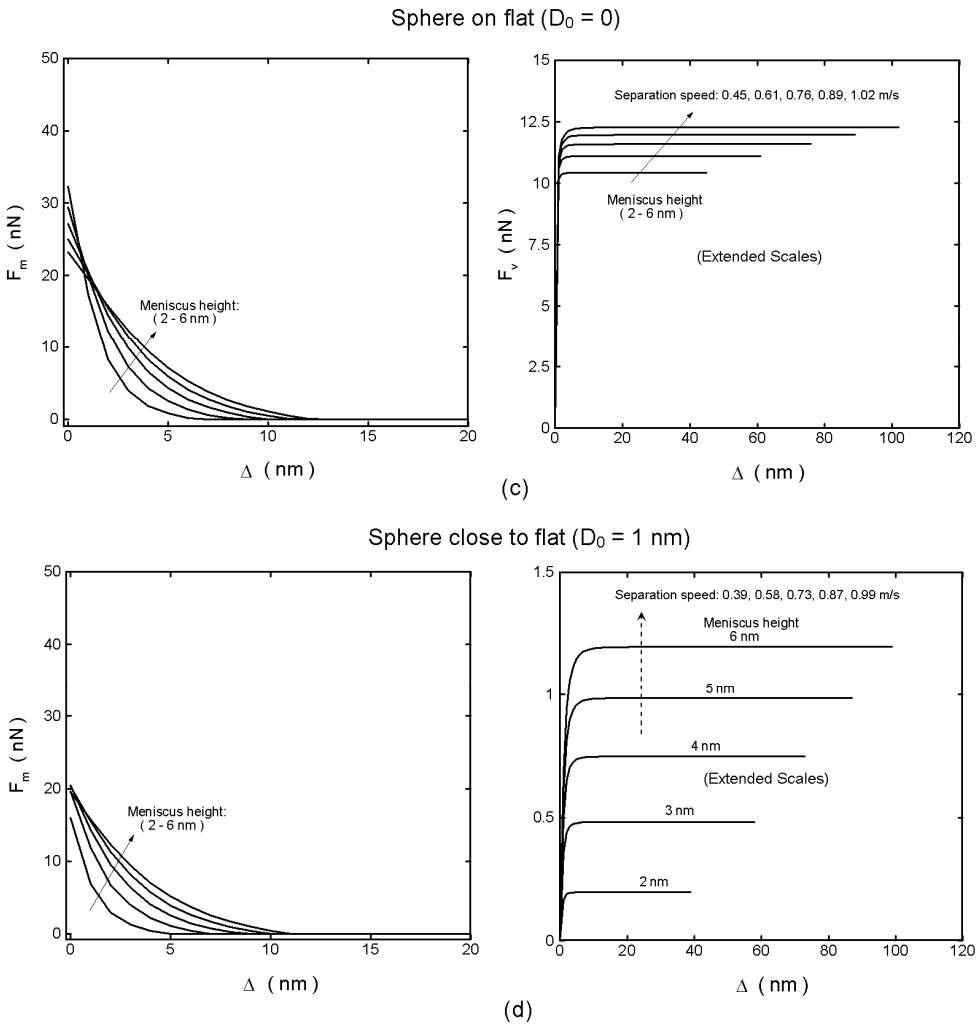

3.2.4.3. Effect of contact angle

For the case of hydrophilic surfaces, the meniscus forces are attractive. The results show that the asymmetric contact angles (one of them kept fixed; here, θ_2 equals 60^o) lead to a larger meniscus force, and the smaller the other contact angle, the larger the meniscus force (Fig. 3.9). It is noted that the asymmetric contact angles play a major role in the quick break of a meniscus. It is observed that for $\theta_1 = 0^o$ and $\theta_2 = 60^o$, there is a smaller break distance as compared to the case $\theta_1 = \theta_2 = 60^o$. For a given set of asymmetric contact angles, the effect of initial meniscus height h_0 on the break distance Δ is insignificant as shown in Fig. 3.10. For the case of hydrophobic surfaces, repulsive meniscus forces are observed in general as shown in Fig. 3.9. A slight attractive force is observed at the later stage of separation. However, the magnitude is small. The attractive effect disappears if one of the contact angles equals 180^o (zoomed figures in Fig. 3.9). This is believed to be the effect of the second term of Eq. (3.11) on the right side, the force due to surface tension of the liquid on the circumference of the solid-liquid interface. The results show that the asymmetric contact angles (one of them kept fixed; here, θ_2 equals 120^o) lead to a larger value of the absolute meniscus force in magnitude, and the larger the other contact angle, the larger the meniscus force (Fig. 3.9), which is different from the hydrophilic situation. Again, it is observed that the asymmetric contact angles play a major role in the quick break of a meniscus. $\theta_1 = 180^o$ has a much smaller break distance as compared to the other case. Also, the effects of a given set of asymmetric contact angles on the break distance are more significant than an initial meniscus height h_0, which has the same trend as for hydrophilic surfaces (Fig. 3.10). An intersection is observed for $\theta_1 = 180^o$ and $\theta_2 = 120^o$. This is due to the multiplication factors varying with various initial meniscus heights. These observations may be useful for the design of travel distance of two surfaces to achieve the optimal size of a device. For both hydrophilic and hydrophobic surfaces, the effect of contact angle on viscous force is insignificant as shown in Fig. 3.10. Separation of a sphere and a flat surface with and without gap at fixed equal contact angles is shown in Fig.3.11. The details have been reported in the previous section.

So far we have reported the effect on meniscus and viscous forces for a set of specific contact angles. Now we analyze the effect for a series of contact angles. Fig. 3.12 summarizes the effect of contact angles on both forces for both hydrophilic and hydrophobic cases. The left sides of Figs. 3.12a and b show the effects on meniscus and viscous forces for fixed θ_2 equals 60^o and various θ_1 from 0 to 90^o. The right sides of Figs. 3.12a and b show the effects on these forces for fixed θ_2 equals 120^o and various θ_1 from 90 to 180^o for a set of various h_0 equal 2 – 6 nm. It is observed that the contact angles have a large effect on the absolute magnitudes of meniscus forces for hydrophilic surfaces: the larger the θ_1, the smaller the meniscus forces. A larger θ_1 can also help decrease the effects of initial h_0 to the magnitude of meniscus forces. For hydrophobic surfaces (right sides of Figs. 3.12a and b), the trends are opposite. Though asymmetric contact angles largely affect meniscus forces, the effects on viscous forces are trivial (Fig. 3.10b). As compared to Figs. 3.12a and b, Figs. 3.12c and d show the effects on both forces for various θ_1 and θ_2 from 0 to 180^o for a fixed h_0 equals 2 nm. The results show that the increase in both or any one of the two contact angles leads to a noticeable decrease in the absolute magnitudes of meniscus forces for a hydrophilic case, as shown on the left side of Fig. 3.12c, but an increase in the absolute magnitudes of meniscus forces for a hydrophobic case, as shown on the right side of Fig. 3.12c. Again, the effects on viscous forces are small (Fig. 3.12d). From the analysis, an increase in contact angle leads to a decrease in attractive meniscus force but an increase in repulsive meniscus force (attractive or repulsive dependent on hydrophilic or hydrophobic surface, respectively). Contact angle has limited effect on the viscous force. For asymmetric contact angles, the magnitude of the meniscus force is in between the values for the two angles.

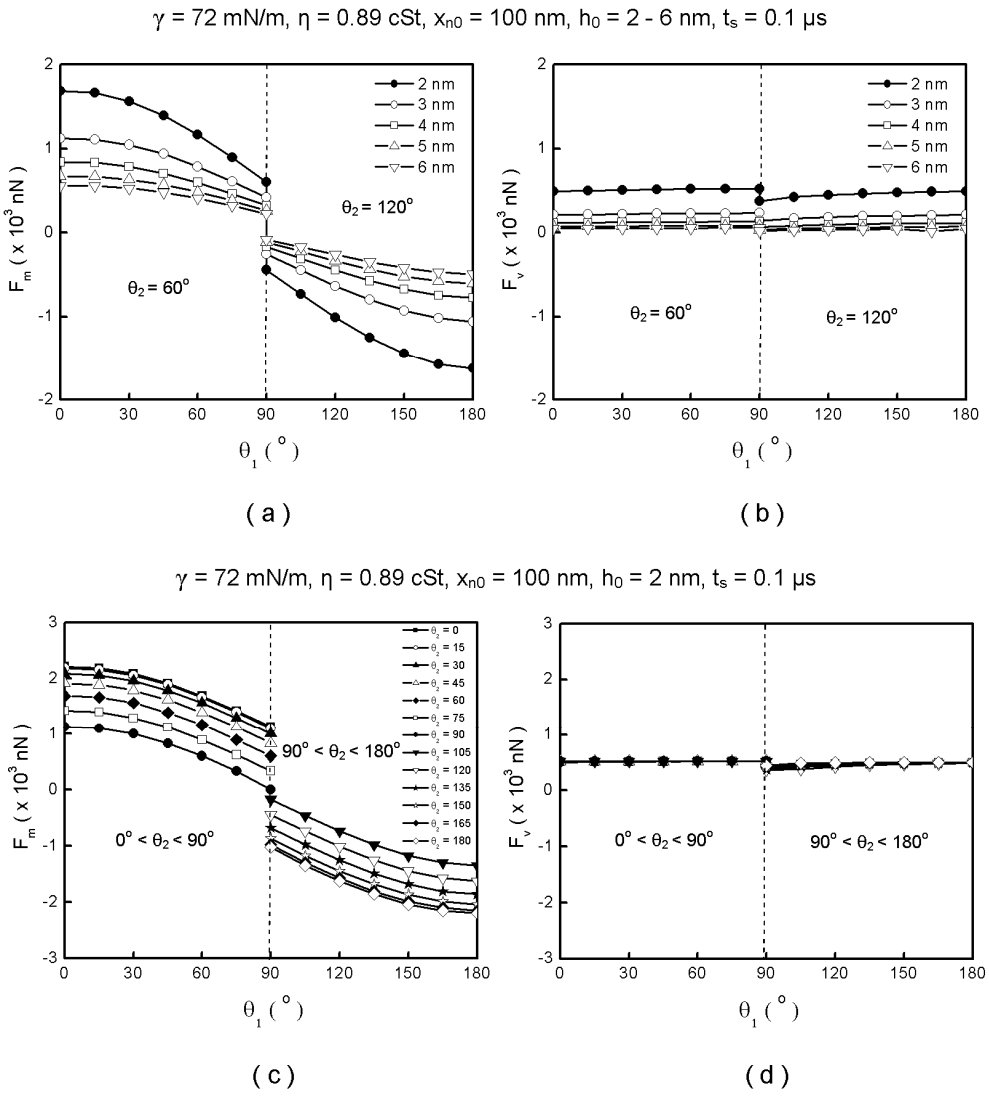

Figure 3.12. (a) Meniscus and (b) viscous forces for various initial meniscus heights (h_0) = 2 - 6 nm for a separation time t_s = 0.1 μs with γ = 72 mN/m, η = 0.89 cSt, x_{n0} = 100 nm, at fixed contact angle $\theta_2 = 60^o$ or $\theta_2 = 120^o$ and various contact angles θ_1; (c) Meniscus and (d) viscous forces at fixed initial meniscus heights (h_0) = 2 nm for a separation time t_s = 0.1 μs with γ = 72 mN/m, η = 0.89 cSt, x_{n0} = 100 nm, at various contact angles θ_1 and θ_2 [Cai and Bhushan, 2007b; 2008a].

3.2.4.4. Effect of separation time

Separation time t_s represents how fast two contact surfaces may be separated. It is an indicator of the system response of a certain device. It is an important parameter for the magnitude of viscous force. For an infinitely long t_s (practically not true), one may neglect viscous force, whereas for a short t_s, viscous force needs to be considered in order to properly estimate the total force needed to separate two surfaces from liquid mediated contacts. For example, the speed of separation is around a few meters per second in a fuel injector; thus, t_s in micro-second scale is used in the simulations. Fig. 3.13 shows both the attractive meniscus force and viscous force as functions of separation time for the cases of separating two flat surfaces (Fig. 3.13a) and a sphere and a flat surface without gap (Fig. 3.13b) and a sphere and a flat surface with gap (Fig. 3.13c). It shows that a very short t_s leads to a large viscous force, but viscous force drops very fast with increasing t_s. This indicates that viscous force may dominate if t_s is small enough.

Fig. 3.14a shows the both meniscus and viscous forces as a function of meniscus area for various initial meniscus heights for contact angles $\theta_1 = \theta_2 = 60^o$, and $\theta_1 = 0^o$, $\theta_2 = 60^o$ and fixed separation time of 0.1 μs, and Fig. 3.14b shows the critical meniscus area as a function of separation time t_s for various initial meniscus heights for contact angles $\theta_1 = \theta_2 = 60^o$, and $\theta_1 = 0^o$, $\theta_2 = 60^o$. Since viscous force is a function of the inverse of separation time t_s, an increase of separation time leads to an increase of critical meniscus area. The explanation is that a larger t_s results in a drop of viscous force, and thus an increase of meniscus area is needed to compensate for the force drop. For a given initial meniscus height and a separation time t_s, one can readily determine the dominating force from the figure during separation process, based on meniscus size information.

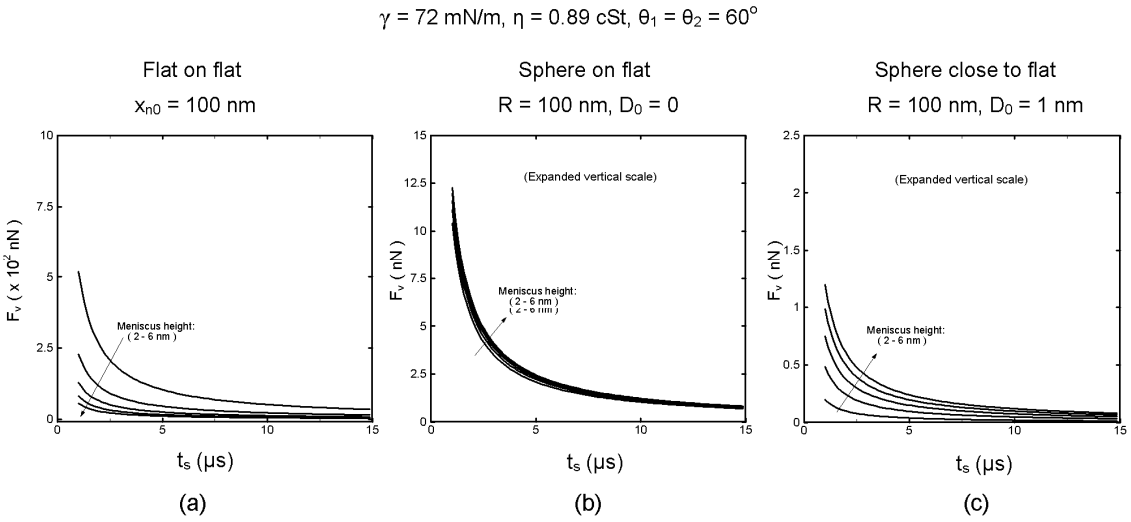

Figure 3.13. Viscous forces versus separation time during separation for various initial meniscus heights (s_0) = 2 - 6 nm with γ = 72 mN/m, contact angle $\theta_1 = \theta_2 = 60^o$ and initial distance, (a) flat to flat $D_0 = s_0$, (b) sphere to flat D_0 = 0, and (c) sphere to flat D_0 = 1 nm [Cai and Bhushan, 2007a].

3.2.4.5. Effect of meniscus area

Meniscus area is one of the most important determinant factors to the magnitude of both meniscus force and viscous force. In general, a larger meniscus area leads to larger meniscus and viscous forces. The goal here is not to verify this intuitive result, but to determine the role these two forces play during a separation process. Based on Fig. 3.14a and 3.14b presented earlier, it is observed that a decrease in contact angle leads to an increase in critical meniscus area. For the given contact angle sets, the asymmetric contact angle pair leads the critical meniscus area to move to a larger value. This is expected since the decrease in one of the contact angles results in a larger meniscus force, and thus, a larger meniscus area is needed for the viscous force to match the meniscus force. For asymmetric contact angles, the critical meniscus area is in between the values for the two angles. The results also show that the increase of meniscus area leads to a large magnitude increase of the two forces. It is observed that viscous force is even more sensitive to meniscus area. The increase of viscous force with meniscus area is much faster than the increase of meniscus force. At a fixed separation time t_s, the two types of forces are comparable when a critical meniscus area is reached. A continuous increase of meniscus area will result in a much higher viscous force (as compared to meniscus force). These trends indicate that either of these two forces may become dominant dependent on the size of meniscus area. The roles of the two forces largely depend on the size of the meniscus. Viscous force dominates for a meniscus size larger than the critical one, and vice versa. For a given separation time and initial meniscus height, a larger meniscus area leads to a larger value of critical meniscus area. Thus, one effective way to minimize these two forces is to minimize the meniscus area. One may neglect viscous force when meniscus area is small enough at a given separation time. But on the contrary, neglecting a viscous force for a large meniscus may lead to an underestimation of a total force needed to separate two surfaces from liquid mediated contacts.

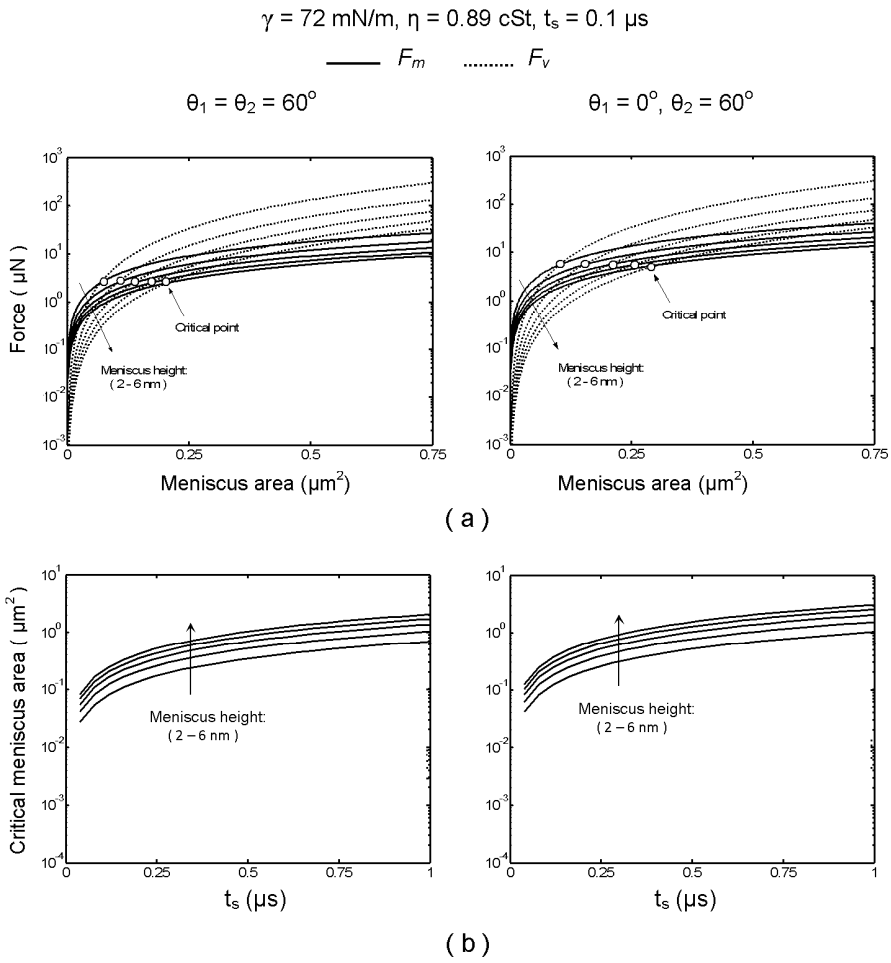

Figure 3.14 (a) Maximum meniscus and viscous forces versus meniscus area with separation time t_s = 0.1 μs, and (b) effect of separation time t_s to critical meniscus area (at which meniscus force and viscous force are comparable during separation of two parallel flats) for $\theta_1 = \theta_2 = 60^o$ and $\theta_1 = 0^o$, $\theta_2 = 60^o$ at various initial meniscus heights h_0 = 2 - 6 nm with γ = 72 mN/m [Cai and Bhushan, 2007 a, b; 2008a].

3.2.4.6. Division of menisci and roughness effects

Figure 3.15 shows the effect on both meniscus and viscous forces due to the division of a large meniscus (with area equal 1 μm^2) into smaller identical menisci. Meniscus forces as a function of the number of divisions are shown in Fig. 3.15a, and viscous forces as a function of the number of divisions are shown in Fig. 3.15b. The number of divisions ranges from 1 to 10^5. It is found that the effects of divisions on meniscus forces and viscous forces are opposite. The number of divisions N leads to an increase of meniscus forces whereas to a decrease of viscous forces. These trends clearly show the "force scaling" effects predicted in section 3.2.1.3. For a given set of non-zero contact angle pairs, one may expect the total meniscus force to increase with an increase in $\sqrt{N}$ due to the division if the initial meniscus area is very small. However, this does not hold for a large size meniscus, as shown here. For the viscous force, one can expect that its magnitude decreases by an order of inverse the number of division (1/N) due to the division, if the break distance is much larger than the initial meniscus height h_0, which is true here, and the viscous forces are very sensitive to the divisions. As compared to the number of division, the effects of initial meniscus height and contact angles on the forces are relatively small. Since the division of menisci produces opposite effects to meniscus and viscous forces, an optimal number of divisions N may be found if both forces are comparable. In the study cases, the optimal number N is a few hundred for a minimum combination of meniscus and viscous forces to achieve a low adhesion. For a set of given initial conditions, a maximum number of division N_{max} may be set, and one may not be able to divide a meniscus into infinitely small menisci. For a given initial meniscus with an area smaller than the critical area, meniscus force is dominant, and the division will result in an increase of the combined force, and vice versa. One may easily obtain low adhesion by reducing the viscous force through the division of the meniscus if the viscous force is the dominate one.

In the study of roughness effects, the number of asperities N used here range from 1 to 10^4, and we assume these surface asperities are identical and have spherical shapes, and these asperities fully occupy the nominal flat area. Fig. 3.16a shows the effects of the number of asperities on meniscus and viscous forces at different contact angles for both

hydrophilic and hydrophobic rough surfaces. It is observed that the increase in the number of asperities leads to an increase in meniscus force (an increase in attractive meniscus force for hydrophilic surfaces and an increase in repulsive meniscus force for hydrophobic surfaces) for a given fixed nominal flat surface area (here 100×100 μm^2). As compared to meniscus force, the effect of the number of asperities on viscous force is trivial for both hydrophilic and hydrophobic surfaces. A noticeable decrease in viscous force is observed for $\theta_1 = 180^o$ and $\theta_2 = 120^o$. This is believed to be due to the quick break of meniscus under the given condition.

For the purpose of comparison, meniscus and viscous forces for the separation of two smooth hydrophilic and hydrophobic surfaces with N identical menisci are also calculated as shown in Fig. 3.16b. The initial separation of two surfaces is the same as for the rough surface case. It is observed that for the study cases the attractive meniscus force slightly increases with the increase in N for hydrophilic smooth surfaces, whereas, it slightly decreases with an increase in N for hydrophobic smooth surfaces. The rate change of force is gradual. Part of the reason may be due to the insignificant change of total meniscus area with N for smooth surfaces. A quick decrease in viscous force is observed with the increase in N for either hydrophilic or hydrophobic surfaces. This is because each meniscus has a smaller meniscus area at larger N, and the meniscus can be broken very quickly. As compared to the rough surface case, both forces are much larger for smooth surfaces at a smaller N. This indicates that the introduction of a small number of asperities can help to reduce both forces significantly and thus reduce stiction.

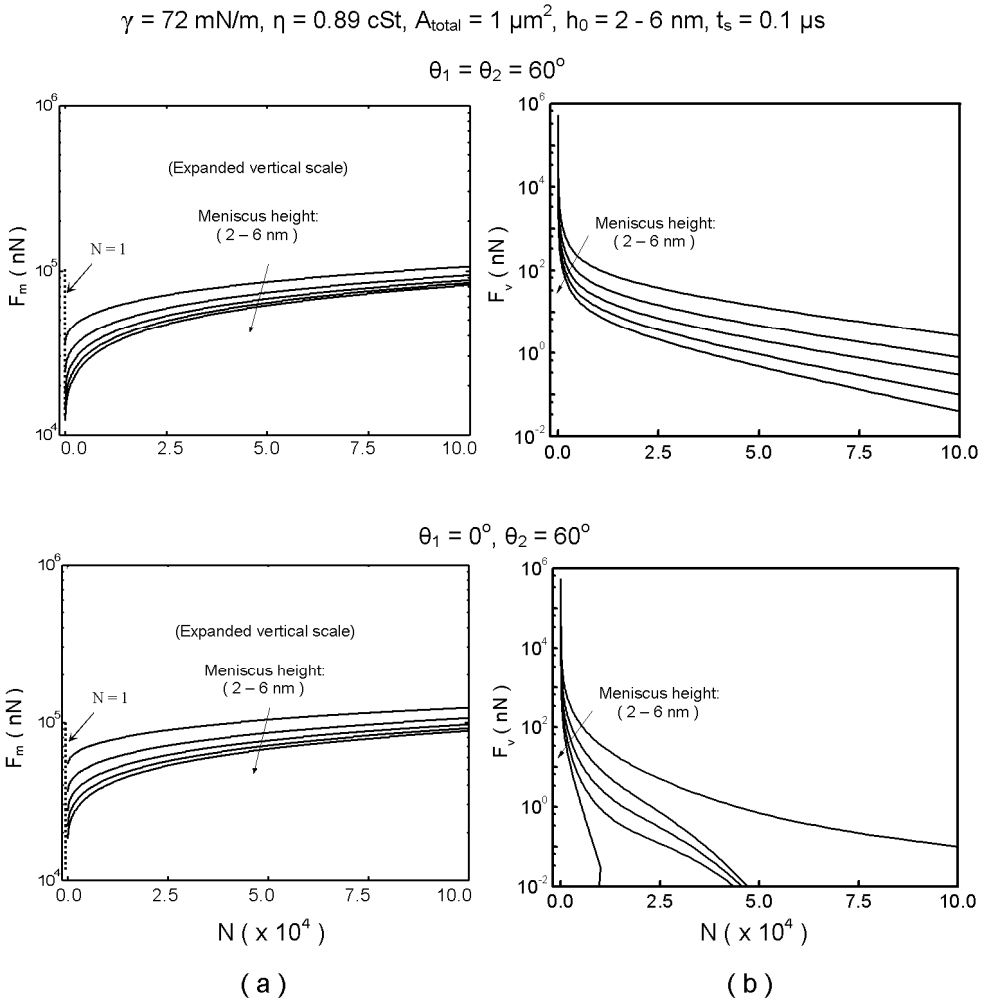

Figure 3.15 (a) Meniscus force and (b) viscous forces, versus number of division for a total meniscus area $A_{total} = 1\ \mu m^2$, various initial meniscus heights (h_0) = 2 - 6 nm for a separation time $t_s = 0.1\ \mu s$ with $\gamma = 72$ mN/m, $\eta = 0.89$ cSt, $x_{n0} = 100$nm, with various contact angles $\theta_1 = \theta_2 = 60^o$, and $\theta_1 = 0^o$, $\theta_2 = 60^o$ [Cai and Bhushan, 2007b].

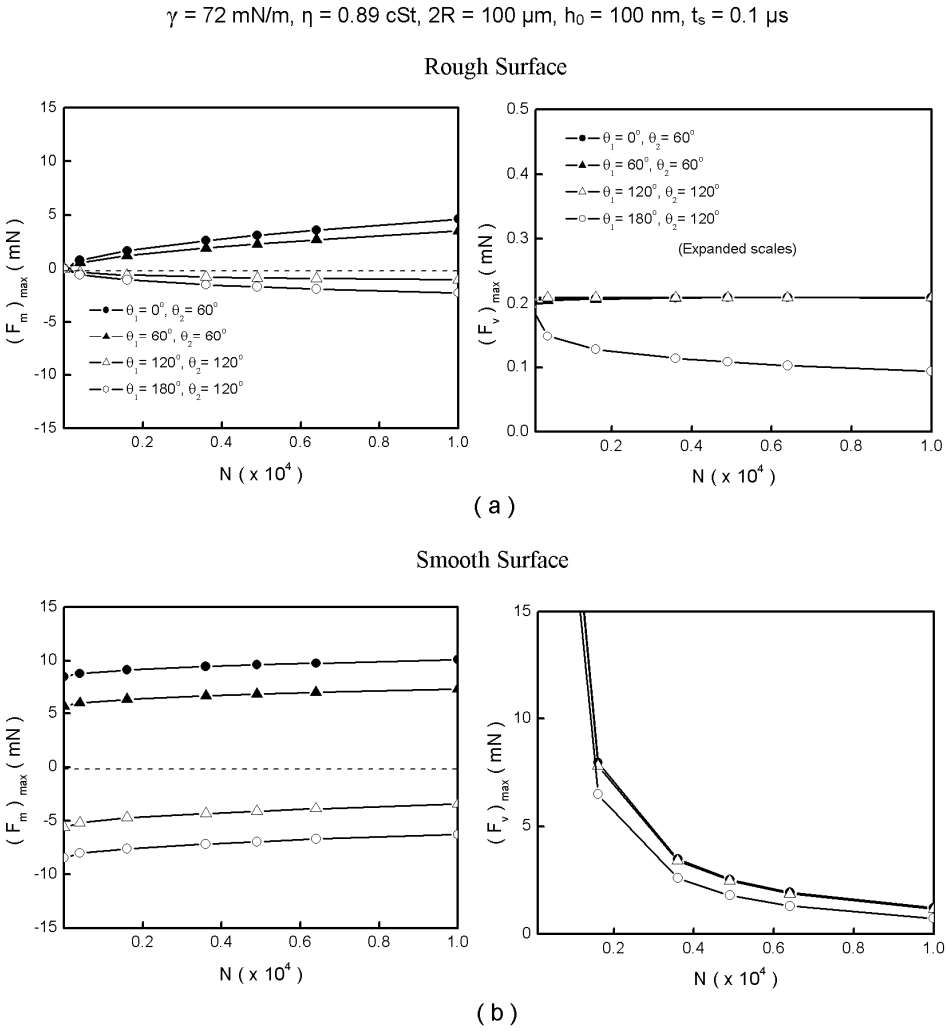

Figure 3.16 Maximum meniscus and viscous forces (a) versus number of asperities N for a rough surface, and (b) versus number of menisci N for a smooth surface for a surface area $2R \times 2R = 100 \times 100\ \mu m^2$ at initial meniscus heights $h_0 = 100$ nm for a separation time $t_s = 0.1$ μs with $\gamma = 72$ mN/m, $\eta = 0.89$ cSt, with various contact angles $\theta_1 = \theta_2 = 60^o$, $\theta_1 = 0^o$, $\theta_2 = 60^o$, $\theta_1 = \theta_2 = 120^o$, and $\theta_1 = 180^o$, $\theta_2 = 120^o$ [Cai and Bhushan, 2008a].

3.2.4.7. Summary

The representative results show that meniscus and viscous forces change at a rapid rate at the early stages of separation. Meniscus force decreases with an increase in separation distance, whereas, the viscous force has an opposite trend. Both forces decrease with an increase in initial meniscus height for separating two flat surfaces. Also, larger initial meniscus height has a longer meniscus break distance. An increase in contact angle leads to a decrease in attractive meniscus force but an increase in repulsive meniscus force (attractive or repulsive, dependent on hydrophilic or hydrophobic surface, respectively). For asymmetric contact angles, the magnitude of the meniscus force and the critical meniscus area are in between the values for the two angles. Though the contact angles significantly affect meniscus force, these only have limited effect on the viscous force. A slightly attractive force is observed for the hydrophobic surface during the end stage of separation, though the magnitude is small.

The combination effects of initial meniscus height and contact angles to both forces are summarized in Table 3.1. It is shown that at a fixed initial meniscus height, an increase in contact angle leads to a decrease in attractive meniscus force for a hydrophilic surface. An increase in both initial meniscus height and contact angle leads to a decrease in attractive meniscus force, and vice versa. For a hydrophobic surface, an increase in contact angle leads to an increase in repulsive meniscus force. An increase in initial meniscus height and a decrease in contact angle lead to a decrease in repulsive meniscus force, and vice versa. As compared to contact angle, the initial meniscus height dominates the effect on viscous force. An increase in separation time leads to a decrease of viscous force. Both forces increase with an increase in meniscus area, and the viscous force is observed to be more sensitive to the change in meniscus area. Either meniscus or viscous force could be a dominant one at a give separation time during the process of separation. For given conditions, a critical meniscus area will be reached when meniscus force equals viscous force. For a meniscus area larger than the critical area, viscous force is dominant, and vice versa. An increase in separation time, initial meniscus height, or the decrease of contact angle leads to an increase in critical meniscus area. For a given

separation time and initial meniscus height, a larger meniscus area leads the critical meniscus area to move to a larger value.

When a large meniscus is divided into a number of smaller identical menisci, "force scaling" effects are found to be true for both meniscus and viscous forces. Meniscus force is proportional to the number of divisions, whereas viscous force is proportional to an inverse of the number of divisions (1/N). The effect of division of menisci is summarized in Table 3.2. The observations will help to design strategies for control of the forces. For a rough surface, an increase in the number of surface asperities (roughness) leads to an increase in meniscus force; however, its effect on viscous force is trivial. As compared to a smooth surface, the introduction of a small number of asperities can help to reduce both forces.

(a) Meniscus forces for hydrophilic and hydrophobic surfaces

Hydrophilic surface (Attractive)

F_m	$\theta_1 = \theta_2$		$\theta_1 \neq \theta_2$			
	↑	↓	$\theta_1 \uparrow \theta_2 \downarrow$	$\theta_1 \downarrow \theta_2 \uparrow$	$\theta_1 \uparrow \theta_2 \uparrow$	$\theta_1 \downarrow \theta_2 \downarrow$
Fixed h_0	↓	↑	n/a	n/a	↓	↑
$h_0 \uparrow$	↓	n/a	n/a	n/a	↓	n/a
$h_0 \downarrow$	n/a	↑	n/a	n/a	n/a	↑

Hydrophobic surface (Repulsive)

F_m	$\theta_1 = \theta_2$		$\theta_1 \neq \theta_2$			
	↑	↓	$\theta_1 \uparrow \theta_2 \downarrow$	$\theta_1 \downarrow \theta_2 \uparrow$	$\theta_1 \uparrow \theta_2 \uparrow$	$\theta_1 \downarrow \theta_2 \downarrow$
Fixed h_0	↑	↓	n/a	n/a	↑	↓
$h_0 \uparrow$	n/a	↓	n/a	n/a	n/a	↓
$h_0 \downarrow$	↑	n/a	n/a	n/a	↑	n/a

(b) Viscous forces for hydrophilic and hydrophobic surfaces

F_v	$\theta_1 = \theta_2$		$\theta_1 \neq \theta_2$			
	↑	↓	$\theta_1 \uparrow \theta_2 \downarrow$	$\theta_1 \downarrow \theta_2 \uparrow$	$\theta_1 \uparrow \theta_2 \uparrow$	$\theta_1 \downarrow \theta_2 \downarrow$
Fixed h_0	not much	not much	not much	not much	not much	not much
$h_0 \uparrow$	↓	↓	↓	↓	↓	↓
$h_0 \downarrow$	↑	↑	↑	↑	↑	↑

Note: meniscus height dominates the effect to viscous force as compared to contact angles.

Table 3.1. Summary of effect of initial meniscus height and contact angle on meniscus and viscous forces [Cai and Bhushan, 2008a].

Division	F_m	F_v
N ↑	↑	↓
N ↓	↓	↑

Table 3.2. Effect of number of division N to meniscus and viscous forces [Cai and Bhushan, 2007b].

3.3. Viscous forces during tangential separation of meniscus bridges in hydrophilic surfaces

Viscous force in tangential separation is encountered in sliding applications. It is necessary to determine the tangential forces for complete characterization of forces in such a process. Matthewson (1988) and Bhushan (1999, 2002) reported the viscous impulses during sliding of a flat surface over another flat surface and a sphere over a flat surface at constant velocity with a meniscus formed in between. The analytical approach used to derive the equations is similar to that of the normal separation case. Recently, Cai and Bhushan (2008b) further formulated the problem and performed a comprehensive analysis to better understand the forces and their roles. In this work, a one- dimensional Couette flow model is used to develop the equations of viscous force during tangential separation of two flat surfaces and a sphere and a flat surface. The analysis is extended to tangential separation of rough surfaces. The effects on viscous force due to separation distance, initial meniscus height, separation time, and roughness are analyzed.

The tangential separation of two smooth/rough surfaces with meniscus bridges is reported in detail in this section. In the analysis, the two surfaces are assumed to be rigid. Due to the complexity of handling a flow with free boundaries, the meniscus shape is not considered during the tangential separation process. Instead, the volume of the trapped liquid in the meniscus is assumed to be constant, and the upper surface moves in one direction parallel to the fixed lower surface during separation. The interaction resulting in the maximum viscous force changes at the upper solid-liquid interface, and the interface is assumed to be a circular area. Thus, an overlapped projected area of the outmost upper and lower solid-liquid circular interfaces is used to estimate the viscous force. The meniscus bridge is assumed to be in equilibrium, and the liquid is incompressible. Thermal effects are considered to be negligible. The shear stress is constant throughout the flow domain. Based on these assumptions, a Couette flow model is used to derive the equations. Chan and Horn (1985) experimentally investigated the viscous force in the drainage of thin liquid films between solid surfaces. The results show that Reynolds theory is in good agreement with experimental viscous force data for a thin film down to

a few nanometers. Thus, in this study, the liquid is treated as continuum in nanoscale, and the properties of the liquid are assumed to remain the same as that in macroscale.

Two basic cases are considered in the study: namely, tangential separation of two flat surfaces, and a sphere and a flat surface. The configurations of the two cases are shown in Figs. 3.17a and b. Based on the Couette flow model, the constant shear stress τ in the liquid for separation of two parallel flat surfaces can be expressed as (Cameron and McEttles, 1981)

$$\tau = \eta \frac{v}{h_0} \tag{3.44}$$

where η is the kinematic viscosity of the given liquid, v is the constant velocity of the upper surface, and h_0 is the initial meniscus height. For a given involved fluid area A, the viscous force due to the liquid viscosity can be estimated

$$F = \tau A \tag{3.45}$$

The schematic of the fluid area A during tangential separation of a meniscus is shown in Fig. 3.17c. In the figure, the fluid area A at the initiation of sliding is the same as the projected meniscus area, and it changes during separation. During the separation process, the area of interest A is the crosshatched area obtained by overlapping the upper and lower boundary of the meniscus. The area A decreases during separation. The functions for the shapes of the upper and lower boundaries are indicated as f_l and f_u. x'_n (shown in the figure) is the radius of the outermost solid-liquid circular interface as indicated, and both upper and lower boundaries are assumed to have a same radius. L is the separation distance between the two centers defined by f_l and f_u during separation in x direction. The dotted circle indicates the final position of the

upper boundary when the break of a meniscus occurs. For the separation of a sphere and a flat surface, we can use the same configuration presented above to calculate the total viscous force. The total viscous force can be found by using the impulse-force relationship. The impulse is determined by integrating the shear stress times the area of interest (crosshatched area) over separation time.

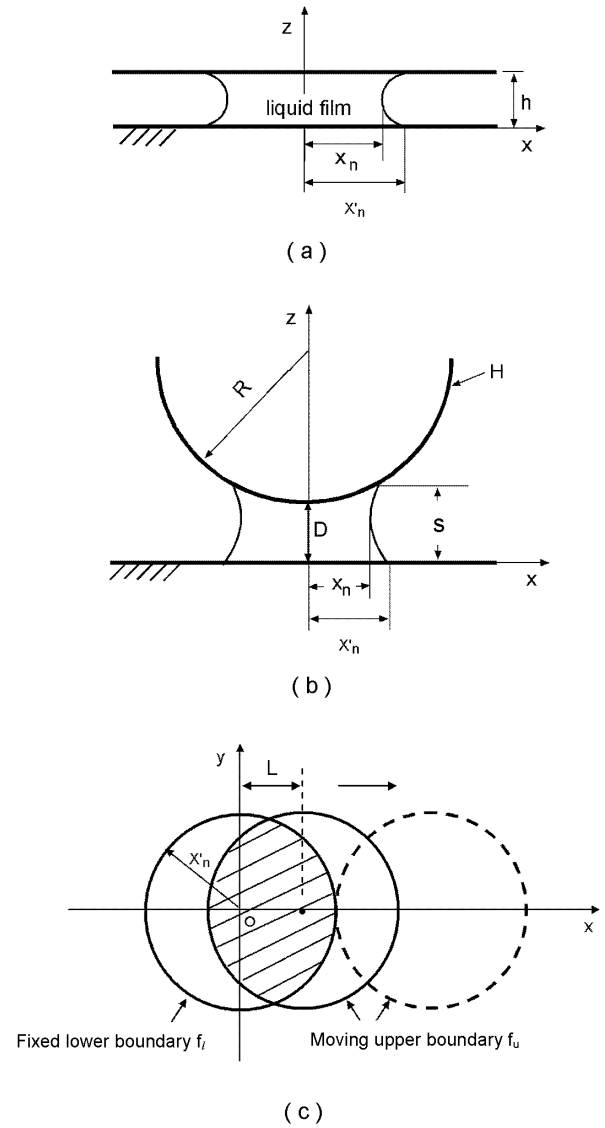

Figure 3.17. Schematics of (a) configurations of two flat surfaces with a meniscus formed in between, (b) configurations of a sphere and a flat surface with a meniscus formed in between, and (c) overlapped projected meniscus area during tangential separation of two surfaces [Cai and Bhushan, 2008b].

3.3.1. Flat-on-flat

In order to derive the equation to calculate the viscous force for the separation of two flat surfaces from a meniscus in tangential direction, we define two functions for the circular shapes of f_l and f_u

$$f_l:\ x^2 + y^2 = x_n'^2$$

$$f_u:\ (x-L)^2 + y^2 = x_n'^2 \tag{3.46}$$

During the separation process, the upper surface moves relative to the lower surface in x direction. An external impulse needed to initialize a separation should be no less than the viscous impulse. Let I_v represent the viscous impulse during separation; then at a finite time interval dt, the change of viscous impulse equals the viscous force F_v multiplying dt

$$\Delta I_v = F dt \tag{3.47}$$

Combining this equation with Eq. (3.44) and (3.45)

$$\Delta I_v = \frac{\eta}{h_0} A dL \tag{3.48}$$

where dl is the distance traveled within dt. The crosshatched area A can be found by using the shape functions f_l and f_u defined in Eq. (3.46). For the convenience of derivation, we define two intermediate functions f_1 and f_2 and rewrite f_l and f_u as $f_1(y) = x = \sqrt{x_n'^2 - y^2}$ and $f_2(y) = x = L - \sqrt{x_n'^2 - y^2}$, respectively. The A can be found

by integrating $f_1(y) - f_2(y)$ along y direction, and the integration limits in y direction can be calculated by substituting L/2 into Eq. (3.46).

$$A = \int_{-\sqrt{x_n'^2 - (\frac{L}{2})^2}}^{\sqrt{x_n'^2 - (\frac{L}{2})^2}} [f_1(y) - f_2(y)]dy \tag{3.49}$$

Since the total separation distance for a break to occur is $2x'_n$ and the circumferences defined by f_l and f_u are assumed to have a same radius, the impulse during the separation process can be obtained by integrating the crosshatched area [Eq. (3.49)] over the total separation distance,

$$I_v = \frac{\eta}{h_0} \int_0^{2x_n'} \int_{-\sqrt{x_n'^2 - (\frac{L}{2})^2}}^{\sqrt{x_n'^2 - (\frac{L}{2})^2}} [f_1(y) - f_2(y)]dydl \tag{3.50}$$

Replacing the functions f_1 and f_2 with their corresponding expressions, we get

$$I_v = \frac{\eta}{h_0} \int_0^{2x_{ni}'} \int_{-\sqrt{x_n'^2 - (\frac{L}{2})^2}}^{\sqrt{x_n'^2 - (\frac{L}{2})^2}} \left[\sqrt{x_n'^2 - y^2} - \left(D - \sqrt{x_n'^2 - y^2} \right) \right] dydl \tag{3.51}$$

Integrating the equation above leads to

$$I_v = \frac{8\eta x_n'^3}{3h_0} \tag{3.52}$$

Thus, the viscous force F_v at the break point can be obtained by using the impulse-force relationship [Eq. (3.47)]

$$F_v = \frac{8\eta x_n'^3}{t_s 3 t_s h_0} \tag{3.53}$$

3.3.2. Sphere-on-flat

For the case of tangential separation of a sphere and a flat surface (Fig. 3.17b), the derivation of the viscous force is similar to the case discussed in section 3.3.1. Since we calculate the viscous force from the crosshatched area over the separation distance, one may use Eq. (3.53) directly with necessary modifications as discussed below. Let H represent the shape function of the upper boundary at radius x within x_n

$$H(x) = \frac{x^2}{2R} + D \tag{3.54}$$

At a given meniscus height s, one can obtain the outermost solid-liquid interfacial radius

$$x_n' = \sqrt{2R(s-D)} \tag{3.55}$$

Substituting the above expression into Eq. (3.53), the viscous force during tangential separation of a sphere and a flat surface can be estimated

$$F_v = \frac{8\eta\left[2R(s-D)\right]^{\frac{3}{2}}}{3t_s s} \tag{3.56}$$

3.3.3. Rough surfaces

Similar to the normal situation (Fig. 3.5), for the separation of two rough surfaces with N number of identical spherical asperities arbitrarily distributed on a flat surface without fully occupying the total surface area, one can expect a maximum viscous force

$$(F_v)_{max} = NF_v \tag{3.57}$$

where F_v is obtained using Eq. (3.56). For the case of N identical spherical asperities fully occupying the total surface area as shown in Fig. 3.5a, the maximum meniscus and viscous force can be determined by using a proper single solid-liquid interfacial radius. Here, for instance, for a flat surface with an area 2R×2R, given that the number of asperities is N = n × n, the radius for each meniscus is R/n or $R/\sqrt{N}$. The viscous forces for each meniscus can be found by substituting this relationship into Eq. (3.56)

$$F_{v-N} = \frac{8\eta}{3st_s}\left[2\frac{R}{\sqrt{N}}(s-D)\right]^{\frac{3}{2}} \tag{3.58}$$

The maximum viscous force for the total N number of formed menisci is

$$(F_v)_{max} = \frac{8\eta}{3st_s\sqrt{N}}\left[2R(s-D)\right]^{\frac{3}{2}} \tag{59}$$

This equation shows that the introduction of roughness leads to a rapid decrease in viscous force. Viscous force is proportional to the inverse square root of the number N ($1/\sqrt{N}$) of asperities.

For tangential separation of two smooth surfaces with N identical menisci, given that the N menisci are arbitrarily distributed on a flat surface without fully occupying the total surface area, again, one can expect a maximum viscous force $(F_v)_{max} = NF_v$, and F_v here is associated with Eq. (3.53). Given that the N identical menisci fully occupy the total surface area as shown in Fig. 3.5b, each single meniscus has a radius $x'_n/\sqrt{N}$. The viscous forces for each meniscus can be found by substituting this relationship into Eq. (3.53)

$$F_{v-N} = \frac{8\eta}{3h_0 t_s}\left[\frac{x'_n}{\sqrt{N}}\right]^3 \tag{60}$$

The maximum viscous force for the total N number of formed menisci is

$$(F_v)_{max} = \frac{8\eta x'^3_n}{3h_0 t_s \sqrt{N}} \tag{61}$$

The equation shows that the viscous force is proportional to the inverse square root of the number N ($1/\sqrt{N}$) of asperities, which is the same as that for the tangential separation of rough surfaces described earlier.

3.3.4. Validation of the model

It is noted that the equations presented here to calculate viscous forces during tangential separation of two flat surfaces are analytically formulated and are consistent with those developed by Matthewson (1988) and Bhushan (1999, 2002). The equation to calculate viscous forces for tangential separation of a sphere and a flat surface is also analytically formulated (Cai and Bhushan, 2008b). The numerical procedure to solve the analytical equations has been verified by using characteristic values similar to that discussed in section 3.2.3.

3.3.5. Representative results

Tangential separation of two smooth/rough surfaces with various initial meniscus heights ranging from 2 to 6 nm is presented. The viscous force is calculated based on the overlapped projected area during separation. For simulation purposes, we assume a meniscus breaks when a zero overlapped projected area is reached. The force needed to overcome a viscous force (due to viscosity) equals the force resulting from the break of a meniscus bridge (which is assumed to occur at zero overlapped projected area). In the analysis, the dimensionless viscous force is defined as follows to eliminate the effect of liquid viscosity for the purpose of comparison. For tangential separation of two flat surfaces, we define the dimensionless viscous force F_v^* as

$$F_v^* = \frac{t_s}{\eta x_n'^2} F_v \tag{3.62}$$

where F_v in the equation is associated with Eq. (3.53). For tangential separation of a sphere and a flat surface, we define the dimensionless viscous force F_v^* as

$$F_v^* = \frac{t_s}{\eta R^2} F_v \tag{3.63}$$

where F_v in the equation is associated with Eq. (3.56). The effect of roughness based on the numerical model is also presented. In the analysis, liquid bridges formed from water are evaluated. 100 nm is used as the initial solid-liquid interfacial radius x'_{n0} for separation of two flat surfaces. This same value is used as the radius R of the spherical asperity for separation of a sphere and a flat surface. For the separation of rough surfaces, a nominal area 100 μm by 100 μm with various larger initial meniscus heights ranging from 100 to 500 nm is used. The separation time 0.1μs is used owing to the real separation time of a diesel fuel injector.

3.3.5.1. Effect of separation distance

Figures 3.18 and 3.19 show the dimensionless and dimensional viscous force versus relative separation Δ for separating two parallel surfaces and a sphere and a flat surface, respectively, from various initial meniscus heights $h_0 = 2 – 6$ nm. The dimensionless figures (Fig. 3.18a, and Fig. 3.19a) presented here are for the purpose of generalization and for general use since the effect of liquid properties has been eliminated. One can obtain the appropriate force magnitudes from these figures for various liquids by simply multiplying the viscosity effects. The dimensional figures (Fig. 3.18b, and Fig. 3.19b) presented here are to show the magnitudes of viscous forces for the purpose comparison. The results show that viscous force increases with an increase in separation distance. This trend is the same as that exhibited in normal separation (Cai and Bhushan, 2007a, b, 2008a). A larger rate of increase in the viscous force is observed at the beginning stage of separation. This trend is the same for both the dimensionless and dimensional results. The larger rate of increase in the force at the beginning of separation is due to the larger rate change in overlapped projected meniscus area which becomes gradual thereafter, as one can expect from examination of Fig. 3.17 for a given constant separation speed. This larger rate of increase in area leads to a relatively large increase in viscous force. As compared to tangential separation of two flat surfaces, the viscous force has a significantly smaller magnitude for separation of a sphere and a flat surface even though both cases have the same physical dimensions. It is not surprising to observe this difference since a spherical asperity leads to a decrease in meniscus area.

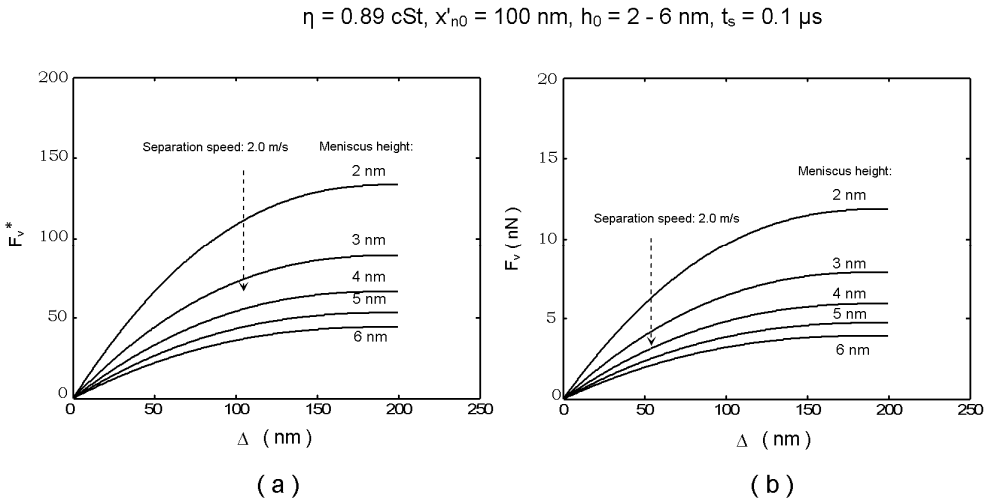

Figure 3.18. (a) Dimensionless and (b) dimensional viscous force versus separation for tangential separation of two flat surfaces for various initial meniscus heights (h_0) = 2 - 6 nm for a separation time t_s = 0.1 μs with η = 0.89 cSt, x'_{n0} = 100 nm [Cai and Bhushan, 2008b].

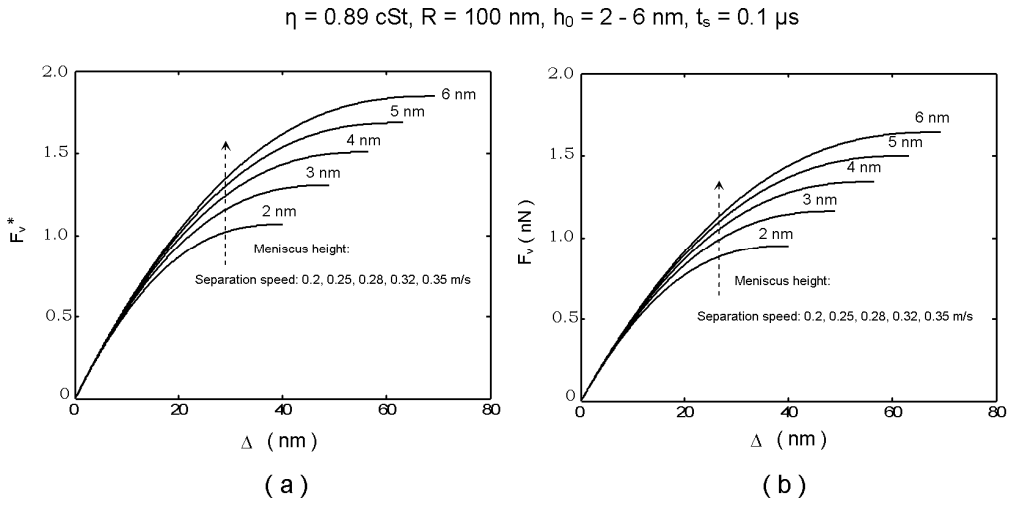

Figure 3.19. (a) Dimensionless and (b) dimensional viscous force versus separation for tangential separation of a sphere and a flat surface for various initial meniscus heights (h_0) = 2 - 6 nm for a separation time t_s = 0.1 μs with η = 0.89 cSt, R = 100 nm [Cai and Bhushan, 2008b].

3.3.5.2. Effect of initial meniscus height

The effect of initial meniscus height h_0 on viscous force can be observed from Figs. 3.18 to 3.21. Figs. 3.18 and 3.19 show the dimensionless and dimensional viscous force versus relative separation Δ for separating two parallel surfaces and a sphere and a flat surface for various initial meniscus heights. Fig. 3.20 shows the viscous forces as a function of separation time for separating two parallel surfaces (Fig. 3.20a) and a sphere and a flat surface (Fig. 3.20b) for various initial meniscus heights. Fig. 3.21 shows the viscous forces as a function of the number of menisci for separating two rough surfaces (Fig. 3.21a) and two smooth surfaces (Fig. 3.21b) for various initial meniscus heights. The initial meniscus height is observed to be one major factor that affects the magnitude of viscous force during the separation process. For separation of two flat surfaces, force decreases with an increase in initial meniscus height as shown in Figs. 3.18, 3.20a, and 3.21b. The same trend is also observed in normal separation (Cai and Bhushan, 2007a, b, 2008a), whereas, the separation of a sphere and a flat surface has an opposite trend as shown in Figs. 3.19, 3.20b, and 3.21a . The dimensionless and dimensional results have the same trend for both cases (Figs. 3.18 and 3.19). The results show that the initial meniscus height does not affect the break distance for the separation of two flat surfaces. This is expected since the initial meniscus height and initial solid-liquid interfacial radius are independent parameters for this case as one can see from Eq. (3.53). However, this situation is different for the case of separation of a sphere and a flat surface, and this is due to the interrelationship of the initial meniscus height and the initial solid-liquid interfacial radius as one can see from Eq. (3.55). For the separation of a sphere and a flat surface, a smaller initial meniscus height leads to a quicker break of meniscus and vice versa. This is due to a smaller initial meniscus height which results in a smaller initial solid-liquid interfacial radius and vice versa.

3.3.5.3. Effect of separation time

Separation time t_s represents how fast a meniscus breaks during the separation process. For an infinitely long t_s (practically not true), one may neglect viscous force, whereas for a short t_s, viscous force needs to be considered in order to properly estimate a

total force needed to separate two surfaces from liquid mediated contacts. Practically, the speed of separation is around a few meters per second in a diesel fuel injector; thus a separation time t_s in microsecond scale is used here to reflect this situation. Viscous force as a function of time is shown in Fig. 3.20, in which Fig. 3.20a is for separation of two flat surfaces and Fig. 3.20b is for separation of a sphere and a flat surface. It is observed that viscous force is proportional to the inverse of separation time which is the same as in normal separation (Cai and Bhushan, 2007a, b, 2008a). A very short t_s leads to a large viscous force, and viscous force drops fast with an increase in t_s. This indicates that viscous force can be significant and may play a major role if t_s is small enough. As compared to the separation of two flat surfaces, the separation of a sphere and a flat surface leads to a significantly smaller viscous force at a given separation time. A combination effect of separation time and initial meniscus height on the viscous force can also be observed from the figure. A larger magnitude difference of the force exists for various initial meniscus heights at a shorter separation time. This indicates that a shorter separation time enhances the effect of initial meniscus height to increase in the force.

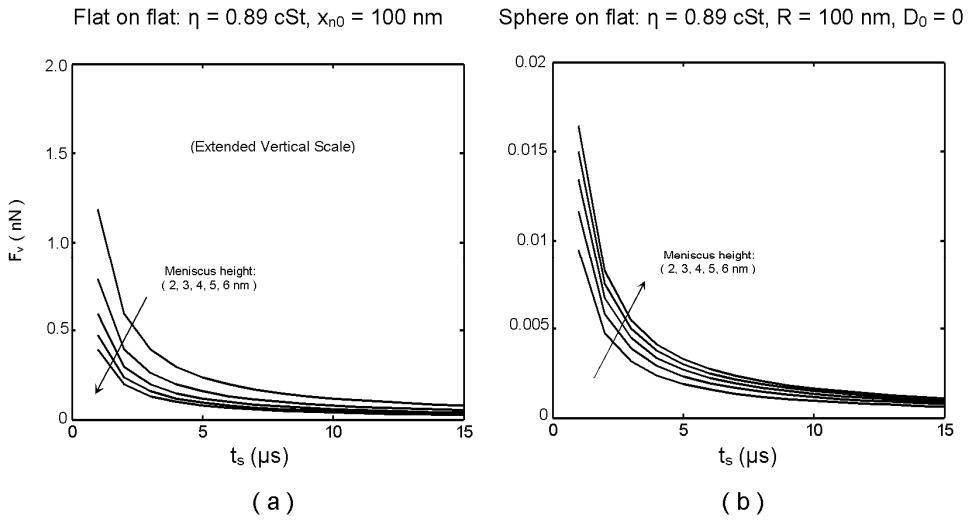

Figure 3.20. Viscous forces versus tangential separation time for various initial meniscus heights (h_0) = 2 - 6 nm with η = 0.89 cSt for (a) flat on flat x'_{n0} = 100 nm, (b) sphere on flat R = 100 nm and initial gap D_0 = 0 [Cai and Bhushan, 2008b].

3.3.5.4. Roughness effect

In the study of roughness effects, the number of asperities N used here ranges from 1 to 10^4. We assume these surface asperities are identical and have spherical shapes, and these asperities fully occupy the nominal flat area. Fig. 3.21a shows the effects of the number of asperities on viscous forces for various initial meniscus heights ranging from 100 nm to 500 nm. It is observed that the increase in number of asperities leads to a decrease in meniscus force for a given fixed nominal flat surface area (here 100×100 μm^2). Viscous force is proportional to the inverse of the square root of the number N ($1/\sqrt{N}$) of asperities. For the purpose of comparison, viscous forces for the separation of two smooth surfaces with N identical menisci are also calculated as shown in Fig. 3.21b. The initial separation of two surfaces is the same as that for the rough surface case. A same trend is observed for the rough surface case; however, the magnitude of the force is significantly larger. Also, the rate of change in force is more gradual as compared to the smooth surface case.

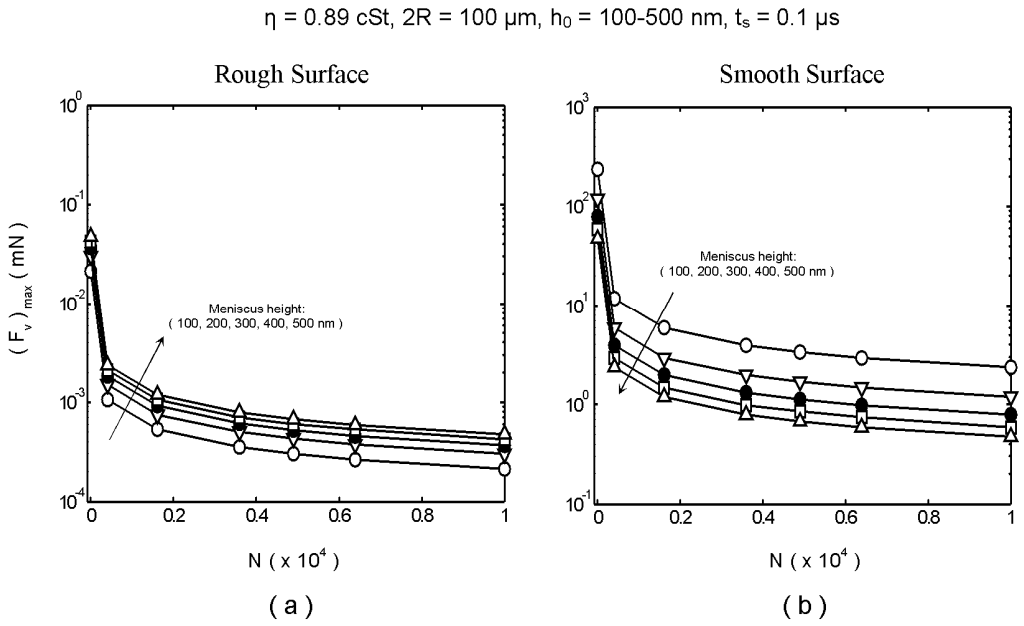

Figure 3.21. Maximum viscous forces (a) versus number of asperities N for a rough surface, and (b) versus number of menisci N for a smooth surface for a surface area $2R \times 2R = 100 \times 100\ \mu m^2$ for various initial meniscus heights h_0 = 100-500 nm at a separation time t_s = 0.1 μs with η = 0.89 cSt [Cai and Bhushan, 2008b].

3.3.5.5. Summary

The results show that viscous force increases with an increase in separation distance. The viscous force changes at a rapid rate at the early stages of separation. A larger magnitude increase in the viscous force is observed at the beginning of separation due to the larger rate change in overlapped projected meniscus area at these stages for a given constant separation speed. As compared to tangential separation of two flat surfaces, the viscous force has a significantly smaller magnitude for separation of a sphere and a flat surface for the studied cases.

Viscous force decreases with an increase in initial meniscus height for separation of two flat surfaces, whereas, it has an opposite trend for the separation of a sphere and a flat surface. Initial meniscus height is not observed to affect the break distance of a meniscus for separation of two flat surfaces due to the independence of the solid-liquid interfacial radius and its height. A larger initial meniscus height leads to a longer meniscus break distance for the separation of a sphere and flat surface owing to the interrelationship of solid-liquid interfacial radius and it height.

Viscous force is proportional to the inverse of separation time. An increase in separation time leads to a quick decrease in the magnitude of the viscous force. The magnitude differences are larger for various initial meniscus heights at a shorter separation time, which indicates that a shorter separation time enhances the effect of initial meniscus height to increase the force.

For the roughness effect, it is found that viscous force is proportional to the inverse square root of the number N ($1/\sqrt{N}$) of asperities. As compared to a smooth surface with a number of menisci, the introduction of roughness does not change the relationship; however, it leads to a significant decrease of the magnitude of the force.

3.4. Applications

Many devices experience adhesion/friction/stiction problems. Examples include magnetic head-disk interface, digital micromirror devices, and diesel fuel injectors. We first describe these three applications and then discuss how to address the problems using the analysis presented previously. The magnetic disk drive system shown in Fig. 3.22 is used for data recording applications (Bhushan, 1996). The read-write operation is performed under steady conditions where a load-carrying film is formed to separate the slider from the disk, and only isolated asperity contacts may occur between them. During the start-stop operations of the disk drive, physical contact occurs and friction is generated during the sliding motion. Thin magnetic films used in the construction of thin-film disks are metallic, such as Co-Cr alloys, which are soft and have poor wear and corrosion resistance. Protective diamond-like carbon (DLC) coatings with a thin lubricant overlay are used to provide low friction, low wear, and corrosion resistance. Due to the applied thin liquid lubricant or condensed water from ambient, the meniscus and viscous forces involved in the separation operation need to be addressed to resolve the potential problems like adhesion/friction/stiction.

Figure 3.23 shows two DMD pixels used for digital projection displays in TV sets, computer projectors, and movie theater projectors (Hornbeck, 1999). The surface micromachined array (chip set) consists of half a million to more than two million of these independently controlled reflective micromirrors (mirror size on the order of 12 μm^2 and 13 μm pitch) which flip backward and forward at a frequency on the order of 5000 times a second. For the binary operation, a micromirror/yoke structure mounted on torsional hinges is rotated at $\pm 10°$ (with respect to the horizontal plane) as a result of electrostatic attraction between the micromirror structure and the underlying memory cell, and is limited by a mechanical stop. Contact between cantilevered spring tips at the end of the yoke (four present on each yoke) with the underlying stationary landing sites is required for true digital (binary) operation. Stiction and wear during a contact between aluminum alloy spring tips and landing sites and sensitivity to particles in the chip package and operating environment are some of the important issues affecting the reliable operation of a micromirror device. The spring tip is used in order to use the spring- stored

energy to pop up the tip during pull-off. Perfluourodecanoic acid (PFDA) self-assembled monolayers applied by a vapor deposition process are used on the tip and landing sites to reduce stiction and wear (Robbins and Jacobs, 2001). Furthermore, a DMD chip is hermetrically sealed to keep it free of contamination and moisture.

Fuel injectors are a typical example of macroscale devices with high stiction due to thin liquid film. Fig. 3.24 shows a cross section of a diesel fuel injector provided by Siemens Diesel Systems Technology. The diameter of the valve is around 6.35 mm. the gap between the end cap and the end of the valve is around 20 μm. A load on the order of 40 N is applied to separate the valve from the end cap (~20 μm) in about 500 μs with an average separation speed of 40 mm/s. During operation, high pressure engine oil comes in and pushes a piston to move downward to push the diesel fuel to inject into the engine. The intake of the high pressure engine oil is controlled by the reciprocating motion of a spool valve, realized by the applied electromagnet attached at the end of an end cap. Adhesion between the spool valve and the end cap occurs frequently. This situation is even worse in cold weather. The adhesion problem reduces the reliability of the device. The solving of the problem needs to be based on the understanding of the forces involved during separation of two solid surfaces from thin liquid film.

The analysis shows that the meniscus force decreases with an increase in separation distance, whereas, the viscous force has an opposite trend (Figs. 3.9 and 3.10). Both forces decrease with an increase of initial meniscus height for separation two flat surfaces (Fig. 3.9 and 3.10). A larger contact angle leads to a smaller meniscus force (Fig. 3.12). A longer separation time leads to a decrease in the viscous force (Fig. 3.13). Both meniscus and viscous forces increase with an increase in meniscus area and the viscous force is observed to be more sensitive to the change in meniscus area (Fig. 3.14). It is observed that either the meniscus or viscous force could be a dominant force at give conditions during the process of separation. A critical meniscus area will be reached when meniscus force equals viscous force. The meniscus area larger than the critical area leads to the viscous force to be a dominant force, otherwise, the meniscus force is a dominant force. An increase in separation time or initial meniscus height or a decrease in contact angle leads to an increase in critical meniscus area. For a given separation time

and initial meniscus height, a larger meniscus area leads to a larger value of the critical meniscus area. The division of a larger meniscus into smaller menisci leads to a significant decrease in viscous force, however with accompanied increase of meniscus force (Fig. 3.15). An increase in roughness leads to a decrease in meniscus and viscous forces as compared to smooth surfaces (Fig. 3.16).

Various methods can be identified to reduce adhesion/friction/stiction problems based on these findings. The analysis presented in this paper can predict the transition (identified as critical meniscus area) from meniscus to viscous regime and helps in identifying relative forces during separation and at the break of a meniscus. The transition can be changed. For example, an increase in meniscus area, separation time, or decrease in viscosity leads to a larger value of critical meniscus area. For a given application, if the viscosity of the liquid is large then one should stay in meniscus regime to avoid/reduce large viscous force, otherwise, transit to viscous force regime as soon as possible. If the viscous force is a dominant force then the division of menisci can help to stay in meniscus regime because the division of a large meniscus into smaller menisci leads to a decrease in viscous force.

Figures 3.9 and 3.11 indicate that a spherical bump leads to smaller meniscus and viscous forces, therefore one may reduce the adhesion by introducing roughness or a few micro spherical bumps on one of the surfaces (i.e., the head for the head-disk system, and one of the mating surfaces of the digital micromirror device and the fuel injector) to obtain lower resultant adhesive force. The micro bumps can be created by using the laser texturing process as done in magnetic rigid disks (Bhushan, 2003). Since a larger contact angle and lower surface energy lead to a smaller meniscus force, coating the surfaces with a material with a lower surface energy and larger contact angle can also help to reduce the resultant adhesive force. Amount of liquid at the contacting interface can be reduced to reduce meniscus and viscous force. Heating the liquid just before relative motion to reduce the viscosity of the liquid can help to achieve lower viscous force (Bhushan, 2003).

In addition, high frequency oscillation of the surfaces with a small amplitude (a few microns) produces an intermittent separation of the contacting surfaces which helps

to reduce meniscus and viscous forces (Bhushan, 2003). Finally, liquid, if needed for lubrication, could be partially bonded to minimize formation of menisci as commonly done in magnetic thin film disks (Bhushan, 1996b, 2003).

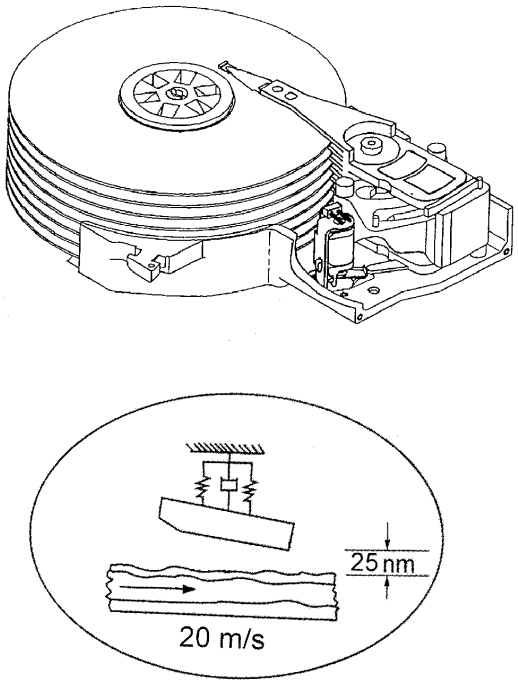

Figure 3.22. A magnetic head slider flying over a disk surface compared with an aircraft flying over ground with a close physical spacing. Stiction is a major issue [Bhushan, 1996].

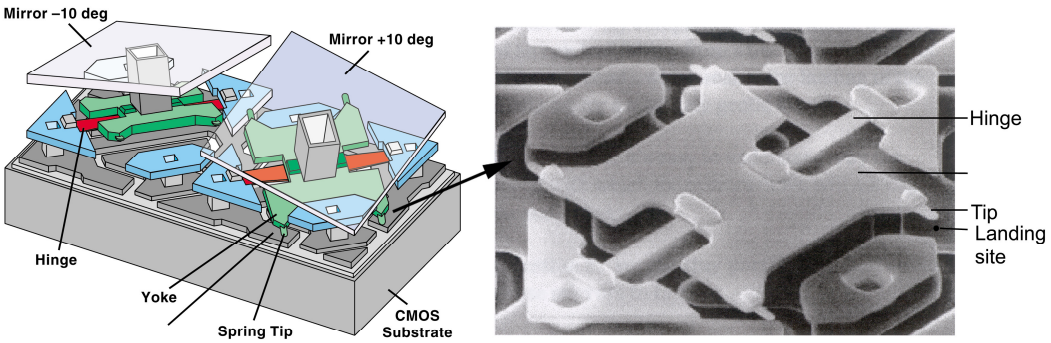

Digital micromirror device for displays (Hornbeck, 1999)

Figure 3.23. A MOEMS device having commercial use that experiences stiction. Typically 12 μm^2 size mirrors with a 13 µm pitch oscillated at a frequency on the order of 5000 times a second [Hornbeck, 1999].

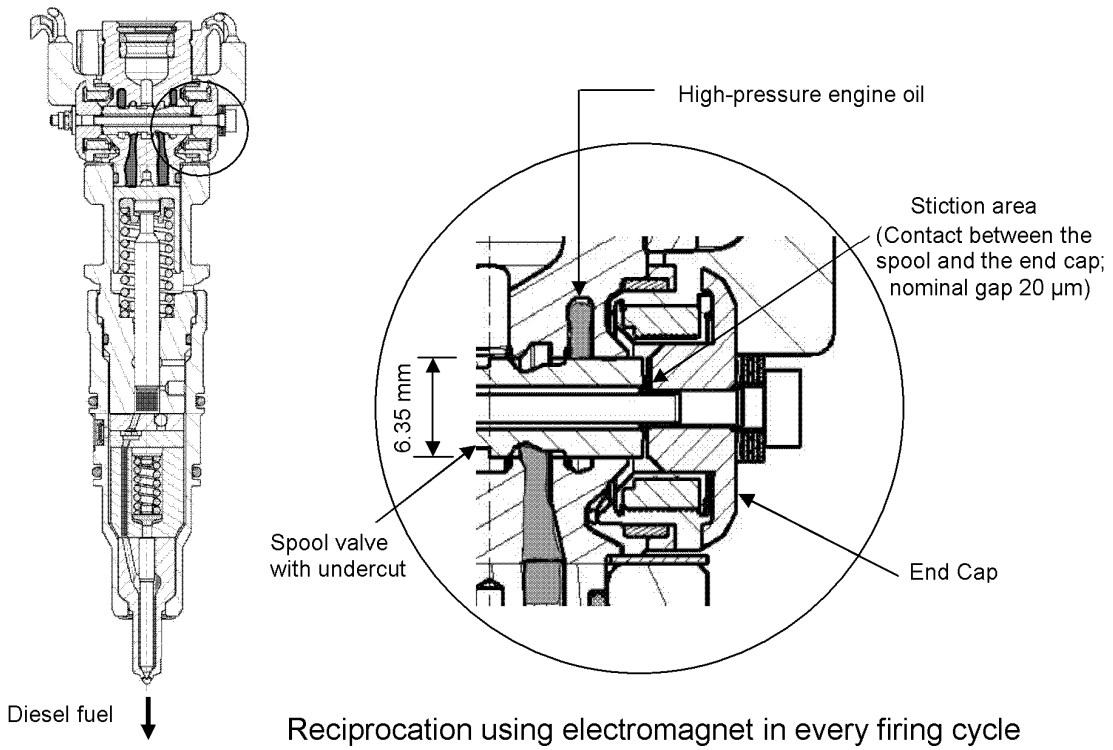

Figure 3.24. Schematic of a diesel fuel injector which experiences adhesion. Reciprocation of the spool occurs using an electromagnet in every firing cycle in order to inject diesel fuel into the engine (Provided by Greg Hafner of Siemens Diesel Systems Technology).

3.5. Recommendations for future work

The current models of separation of two surfaces with liquid mediated contacts are generally based on arc-shaped meniscus curvature. The boundary conditions are well defined. It would be of interest to determine the meniscus and viscous forces by considering a meniscus with free boundary (rather than a well defined boundary) during the separation process. The introduction of air inside a meniscus (as is in real world) will also be of interest. Idealized rough surfaces have been modeled, so far. The current models may be extended to take into account random rough surfaces. In addition, during separation, the effect of vibration of two surfaces on meniscus and viscous forces will also be of interest.

In the current model of tangential separation of two surfaces with liquid mediated contacts, the effect of contact angle is not considered. Instead, the meniscus is assumed to have flat boundaries. Based on the flat boundaries, a project meniscus area is used to calculate viscous forces for a constant meniscus volume. It would be of interest to include the contact angle in the future studies. The challenge would be to develop an effective method to determine the meniscus curvature for given contact angles. One way to do that would be the consideration of the meniscus having a free boundary rather than flat boundaries.

It is also noted that the current models are all analytically formulated. The validation of the models is done based on calculation of some characteristic values which is good for the analytical formulations. It would be more instructive if these models can be further verified with experiments. The experimental validation of these models is feasible and the method to design the experiments is straight forward. For example, one can choose two smooth surfaces, flat-on-flat or sphere-on-flat, with a small amount of liquid in between two surfaces. After measurement of some important parameters, e.g., the contact angle, the radius of the meniscus and the initial meniscus height, the two surfaces are pulled at a controlled speed. The force needed for separation of the two surfaces can be measured during the pull and at the point the liquid bridge breaks. The measured values can then be compared with the ones calculated using the analytical formulations.

CHAPTER 4

CONCLUSIONS AND RECOMMENDATION FOR FUTURE WORK

Numerical models for the contact of rough multilayered solid surfaces and separation of two surfaces from liquid mediated contacts are developed. The analyses are performed. The conclusions based on the analyses of both models are presented below. Recommendations for future work based on the studies are given at the end of this section.

4.1. Conclusion for contact of rough multilayered solid surfaces

Numerical contact models of layered solid rough surfaces are developed to study the contact mechanics and predict optimal design parameters, including roughness, stiffness, hardness, layers thickness, load, and coefficient of friction effects. Numerical approaches, such as FDM, FEM, or BEM are commonly used to perform simulation tasks depending on the way the rough solid is being divided. In general, FEM and BEM are more flexible than FDM, and theoretically both are applicable to multiple asperity contact. As compared to FEM, BEM can achieve high computational efficiency because discretization is carried out only of the contacting interface. The contact problems can be formulated with different principles depending on the complexity of the problem. Typically, there are three methods to formulate the problem, namely, direct formulation, weighted residual formulation, and minimum total potential energy formulation. The minimum total potential energy formulation allows the use of a quadratic programming method, such as the quasi-Newton method to solve an optimization problem, which

theoretically guarantees the convergence and the uniqueness of the solution. The combination of minimum total potential energy formulation with BEM approach is feasible to solve the 3D rough surface contact problems with a large number of contact points due to their associated advantages. Thus, the multilayered rough contact model can be simulated based on them. Representative results are reported to predict the contact pressure profile on the interface and contact statistics, namely fractional contact area, the maximum value of contact pressure, von Mises stresses, principal tensile stresses and shear stresses, and relative meniscus forces. These results are obtained for various surface roughness, elastic and elastic/plastic material properties, normal loading and frictional loading, and dry and wet conditions. The effects of the contact statistics, adhesion, friction, stiction issues, are addressed. Suggestions for design criteria are made from the tribological point of view.

The results show that the maximum contact pressure and surface/subsurface stresses are highly dependent on surface roughness, stiffness and hardness of the layers and the substrate, layer thickness, and load. Friction significantly affects the maximum surface/subsurface stresses; however, it does not have noticeable effect on contact pressure. The increase in surface roughness leads to a decrease in real area of contact, which is beneficial to minimize friction and stiction. However, the increase in surface roughness causes larger maximum contact pressure, accordingly large surface and subsurface stresses, which are not desirable to improve wear. As compared to a homogeneous solid, a stiff top layer leads to smaller real area of contact and larger contact pressure and stresses; a more compliant interlayer leads to lower maximum contact pressure and surface/subsurface stresses but a larger real area of contact, whereas, a more stiff interlayer has an opposite trend. A solid with a more compliant top layer is not advisable since it results in a significant increase in real area of contact which associates with high friction. These trends are consistent regardless of friction. Hardness effects exhibit similar trends as stiffness effects. The effective hardness plays a role in the elastic-plastic regime. The maximum contact pressure can be higher, lower or equal to the top layer's hardness for elastic-perfectly plastic contact. Its magnitude depends on the layer properties. It is not advisable to use a softer top layer since plastic contact is easier

to occur (with the increase of applied load) which leads to high wear. It is observed that no plastic contact occurs for a solid with a harder top layer. A higher hardness may be chosen in order to increase the resistance to wear. Layer thickness is a very important parameter to improve frictional properties. Proper layer thicknesses enhance the layer effects in both elastic and elastic/plastic contact domain. The proper design of layer thicknesses can be used to obtain lower maximum contact pressure and maximum surface/subsurface stresses and to avoid the possible occurrence of plastic contact, and therefore can be used to obtain low wear. The introduction of friction leads to a significant increase in the maximum surface/subsurface stresses, especially the shear stress. Also, it results in the change of their locations to the surface.

For wet contact, meniscus force decreases with an increase in surface roughness (increase in standard deviation of surface height σ or decrease in correlation length β^*). Meniscus force increases with an increase of real area of contact, and vice versa. For a given load, the meniscus force is lower for stiff/hard top layers, since fewer asperities can touch the liquid and form menisci, whereas compliant/soft top layers have the opposite effects. A compliant interlayer leads to a larger decrease in relative meniscus force as compared to that of compliant top layers, and a stiff interlayer leads only to a small increase in relative meniscus force as compared to that of stiff top layers. Similar trends are observed for the changing of hardness but confined to the elastic-plastic regime.

The applications of the multilayered rough contact model to magnetic storage devices are discussed.

4.2. Conclusion for separation of two surfaces from liquid mediated contacts

The equations for meniscus and viscous forces during separation of two flat surfaces and a sphere and a flat surface are developed. The equations are summarized in Table 4.1. Both forces during separation of hydrophilic and hydrophobic smooth/rough surfaces with symmetric and asymmetric contact angles are calculated. The effects of separation distance, initial meniscus height, contact angle, separation time, meniscus area, division of menisci, and roughness on both meniscus and viscous forces are quantitatively reported in normal separation, and the effects of separation distance, initial

meniscus height, separation time, and roughness on viscous force are reported in tangential separation. The combination of effects of initial meniscus height (for instance, humidity) and contact angles (material's property) and the effect of division of menisci on meniscus and viscous forces are summarized.

In normal separation, the results show that meniscus and viscous forces are largely dependent on separation distance. The meniscus force decreases with an increase in separation distance, whereas, the viscous force has an opposite trend. Both forces decrease with an increase in initial meniscus height. An increase in contact angle leads to a decrease in attractive meniscus force but an appreciable increase in repulsive meniscus force (attractive or repulsive dependent on hydrophilic or hydrophobic surface, respectively), but the contact angles have only limited effect on the viscous force. A slightly attractive force is observed for the hydrophobic surface during the end stage of separation though the magnitude is small. An increase in separation time leads to a decrease of viscous force. Both forces increase with an increase in meniscus area, and the viscous force is observed to be more sensitive to the change in meniscus area. Either the meniscus or viscous force could be a dominant at a given separation time during the process of separation. For given conditions, a critical meniscus area will be reached when meniscus force equals viscous force. When a meniscus area is larger than this area, viscous force is dominant, and vice versa. An increase in separation time, or initial meniscus height or a decrease in contact angle leads to an increase in critical meniscus area. For a given separation time and initial meniscus height, a larger meniscus area leads to a larger value of the critical meniscus area. "Force scaling" effects are observed for both forces when one larger meniscus is divided into a large number of identical micro-menisci. For rough surface, an increase in the number of surface asperities (roughness) leads to an increase of meniscus force, however; its effect on viscous force is trivial. An increase in roughness leads to a decrease in meniscus and viscous forces as compared to smooth surfaces.

In tangential separation, the results show that viscous force increases with an increase in separation distance, which is the same as in normal separation. As compared to tangential separation of two flat surfaces, the viscous force has a significantly smaller

magnitude for separation of a sphere and a flat surface for the studied cases. Viscous force decreases with an increase in initial meniscus height for separation of two flat surfaces, whereas, it has an opposite trend for the separation of a sphere and a flat surface. Again, viscous force is inversely proportional to the separation time. It is found that viscous force is proportional to the inverse square root of the number N ($1/\sqrt{N}$) of asperities when roughness is introduced.

The analysis of both meniscus and viscous force during separation of two surfaces provided here helps to better understand the physics of the problems involved, i.e., adhesion, friction and stiction and to provide solution to reduce these problems. Applications of the analysis to solve real engineering problems for both macro and micro devices are discussed.

Flat-on-Flat

Static meniscus force:

$F_m = \frac{\pi x_n^2 \gamma(\cos\theta_1 + \cos\theta_2)}{h} + 2\pi\gamma x_n \sin\theta_{1,2}$ (1 and 2 for lower and upper surface respectively)

Normal separation:

Meniscus force: $F_m = \frac{\pi x_{ni}^2 \gamma(\cos\theta_1 + \cos\theta_2)}{h} + 2\pi\gamma x_{ni} \sin\theta_{1,2}$

Viscous force: $F_V = \frac{3\pi\eta x_{ni}^4}{4t_s}(\frac{1}{h_s^2} - \frac{1}{h_0^2}) \sim \frac{-3\pi\eta x_{ni}^4}{4t_s h_0^2}$ (for $h_s \sim \infty$)

Sphere-on-Flat

Static meniscus force:

Normal separation:

$F_m = 2\pi R\gamma(\cos\theta_1 + \cos\theta_2) + 2\pi R\gamma \sin\phi \sin(\phi + \theta_2)$ (sphere-on-flat)

$\sim 2\pi R\gamma(\cos\theta_1 + \cos\theta_2)$ (for small ϕ)

$\sim \frac{2\pi R\gamma(cos\,\theta_1 + cos\,\theta_2)}{1 + (D/d_0)}$ (sphere close to flat and for small ϕ)

$\sim 2\pi R\gamma(1 + \cos\theta)$ (sphere close to a flat with a continuous liquid film And for small ϕ)

Meniscus force: $F_m = \pi x_{ni}^2 \gamma(\frac{1}{r_{li}} + \frac{1}{x_{ci} - r_{li}}) + 2\pi R\gamma \sin\phi \sin(\phi + \theta_2)$

Viscous force:

$F_V = \frac{6\pi\eta R^2}{t_s} \ln \frac{D_s[D_0 + H(x_{n0})]^2 \sqrt{H(x_{n0})^2 - D_0^2 + D_s^2}}{D_0 H(x_{n0})\left[D + \sqrt{H(x_{n0})^2 - D_0^2 + D_s^2}\right]^2} \sim \frac{6\pi\eta R^2}{t_s} \ln[\frac{H(x_{n0})}{2D_0}]$ (for $D_s \sim \infty$)

Continued

Table 4.1. A summary of equations for meniscus and viscous forces for various cases.

Table 4.1 continued

Normal Separation

Smooth Surfaces

$(F_m)_{\max} = NF_m$ (without full occupation, flat-on-flat)

$(F_v)_{\max} = NF_v$ (without full occupation, flat-on-flat)

$(F_m)_{\max} = NF_m(\frac{x_{ni}}{n})$ (full occupation , flat-on-flat)

$(F_v)_{\max} = NF_v(\frac{x_{ni}}{n})$ (full occupation, flat-on-flat)

Rough surfaces

$(F_m)_{\max} = NF_m$ (without full occupation, sphere-on-flat)

$(F_v)_{\max} = NF_v$ (without full occupation, sphere-on-flat)

$(F_m)_{\max} = NF_m(\frac{R}{n})$ (full occupation, sphere-on-flat)

$(F_v)_{\max} = NF_v(\frac{R}{n})$ (full occupation, sphere-on-flat)

Meniscus Division

Meniscus force: $F_{m-NT} = \frac{\pi x_{ni}^2 \gamma(\cos\theta_1 + \cos\theta_2)}{h} + 2\sqrt{N}\pi\gamma x_{ni}\sin\theta_{1,2}$

$F_{m-NT} \sim \sqrt{N}F_{m-N}$ (for small x_{ni})

Viscous force: $F_{v-NT} = \frac{3\pi\eta x_{ni}^4}{4Nt_s}(\frac{1}{h_{s-N}^2} - \frac{1}{h_0^2})$

$F_{v-NT} \sim \frac{F_V}{N}$ (for $h_s \sim \infty$)

Continued

Table 4.1 continued

Tangential Separation

Viscous force:

Falt-on-flat: Single meniscus: $F_v = \dfrac{8\eta x_n'^3}{3t_s h_0}$

Multiple menisci: $(F_v)_{\max} = NF_v$ (without full occupation)

$$(F_v)_{\max} = \frac{8\eta x_n'^3}{3h_0 t_s \sqrt{N}} \text{ (full occupation)}$$

Sphere-on-flat: Single meniscus: $F_v = \dfrac{8\eta\left[2R(s-D)\right]^{3/2}}{3t_s s}$

Multiple menisci: $(F_v)_{\max} = NF_v$ (without full occupation)

$$(F_v)_{max} = \frac{8\eta}{3st_s\sqrt{N}}\left[2R(s-D)\right]^{3/2} \text{ (full occupation)}$$

BIBLIOGRAPHY

Adamson AW (1990), *Physical Chemistry of Surfaces*, fifth ed., Wiley, New York.

Ai X and Sawamiphakdi K (1999), Solving elastic contact between rough surfaces as an unconstrained strain energy minimization by using CGM and FFT techniques, *ASME J. Tribol.* **121**, 639–647.

Aveyard R, Clint J H, Paunov VN, Nees D (1999), Capillary condensation of vapors between two solid surfaces: effects of line tension and surface forces, *Phys. Chem. Phys. Chem*. **1**, 155-163.

Bachmann J, van der Ploeg RR (2002), A review on recent developments in soil water retention theory: interfacial tension and temperature effects, *J. Plant Nutr. Soil Sci*. **165**, 468-478.

Bayramli E, Huh C and Mason SG (1978), Sphere tensiometry: wall effects and correction factors**,** *Canad. J. Chem*. **56**, 818-823.

Beer G and Watson JO (1992), *Introduction to Finite and Boundary Element Methods for Engineers*, John Wiley, New York.

Bentz DP, Quenard DA, Baroghel-Boouny V, Garboczi EJ and Jennings HM (1995), Modelling drying shrinkage of cement paste and mortar Part 1. Structural models from nanometres to millimeters, *Materials and Structures* **28**, 450–458.

Bhushan B (1994), Tribology of Solid Contacts in Magnetic Recording Devices, *Appl. Mech. Rev.* **47**, No. 6, Part 2, S199-S203.

Bhushan B (1996a), Contact Mechanics of Rough Surfaces in Tribology: Single Asperity Contact, *Appl. Mech. Rev.* **49**, 275-298.

Bhushan B (1996b), *Tribology and Mechanics of Magnetic Storage Devices*, second ed., Springer-Verlag, New York.

Bhushan B (1998), Contact mechanics of rough surfaces in tribology: Multiple asperity contact, *Tribol. Lett.* **4**, 1–35.

Bhushan B (1999a), *Handbook of Micro/Nanotribology*, CRC Press, Boca Raton FL.
Bhushan B (1999b), *Principles and Applications of Tribology*, Wiley, New York.

Bhushan B (1999c), Chemical, mechanical and tribological characterization of ultra-thin and hard amorphous carbon coatings as thin as 3.5 nm: recent developments, *Diamond Relat. Mater*. **8**, 1985–2015.

Bhushan B (2001), *Modern Tribology Handbook, Vol. 1: Principles of Tribology*; *Vol 2: Materials, Coatings, and Industrial Applications*, CRC Press, Boca Raton FL.

Bhushan B (2002), *Introduction to Tribology*, John Wiley, New York.

Bhushan B (2003), Adhesion and stiction: mechanisms, measurement techniques, and methods for reduction, *J. Vac. Sci. Technol. B* **21**, 2262-2296.

Bhushan B (2005), *Nanotribology and Nanomechanics: An Introduction*, Springer, Heidelberg, Germany.

Bhushan B (2007), *Springer Handbook of Nanotechnology, second ed.*, Springer, Heidelberg.

Bhushan B and Gupta BK (1991), *Handbook of Tribology: Materials, Coating and Surface Treatments*, McGraw-Hill, New York.

Bhushan B and Peng W (2002), Contact Mechanics of Multilayered Rough Surfaces, *Appl. Mech. Rev*. **55**, pp. 435–480

Bhushan B and Peng W (2002), Contact Mechanics of Multilayered Rough Surfaces, *Appl. Mech. Rev.* **55**, 435-480.

Bhushan B and Venkatesan S (2005), Effective Mechanical Properties of Layered Rough Surfaces, *Thin Solid Films.* **473**, 278-295

Bhushan B, Chyung K, and Miller RA (1996), Micromechanical property measurements of glass and glass-ceramic substrates for magnetic thin-film rigid disks for gigabit recording, *Adv. Inf. Storage Syst*. **7**, 3–17.

Bikerman JJ (1947), The Fundamentals of Tackiness and Adhesion, *J. Colloid. Inter. Sci.*, **2**, 163-175.

Bikerman JJ (1950), Sliding of drops from surfaces of different roughnesses, *J. Colloid. Inter. Sci.*, **5**, 349-359.

Bocquet L, Charlaix E, Ciliberto S, and Crassous J (1998), Moisture-induced ageing in granular media and the kinetics of capillary condensation, *Nature* **396** 735-737.

Bowden FP and Tabor D (1950), *The Friction and Lubrication of Solids, Part I*, Clarendon Press, Oxford.

Bowden FP and Tabor D (1964), *The Friction and Lubrication of Solids, Part II*, Clarendon Press, Oxford.

Burmister DM (1945), The general theory of stresses and displacements in layered systems, *J. Appl. Phys.* **16**, 89–94.

Cai S and Bhushan B (2005), A Numerical Three-Dimensional Contact Model for Rough, Multilayered Elastic/Plastic Solid Surfaces, *Wear* **259**, 1408–1423.

Cai S and Bhushan B (2006), Three-dimensional dry/wet contact analysis of multilayered elastic/plastic solids with rough surfaces, *ASME J. Tribol*. **128**, 18–31.

Cai S and Bhushan B (2007a), Three-Dimensional Sliding Contact Analysis of Multilayered Solids with Rough Surfaces, *ASME J. Tribol*. **129**, 40–59.

Cai S and Bhushan B (2007b), Meniscus and Viscous Forces During Normal Separation of Liquid-Mediated Contacts, *Nanotechnology* **18**, 465704, 1-14.

Cai S and Bhushan B (2007c), Effects of Symmetric and Asymmetric Contact Angles and Division of Menisci during Separation, *Phil.Mag.* **87**, 5505-5522.

Cai S and Bhushan B (2008a), Meniscus and Viscous Forces during Separation of Hydrophilic and Hydrophobic Smooth/Rough Surfaces with Symmetric and Asymmetric Contact Angles, *Phil. Trans. R. Soc. A,* in press.

Cai S and Bhushan B (2008b), Viscous Forces during Tangential Sliding of Micro Meniscus, *Phil. Mag.* **88**, 449-461.

Cameron A and McEttles CM (1981), *Basic Lubrication Theory*, Wiley, New York.
Carter WC (1988), The forces and behavior of fluids constrained solids, *Acta Metall*, **36**, 2283–2292.

Chan DY and Horn RG (1985), The drainage of thin liquid films between solid surfaces, *J. Chem. Phys*. **83,** 5311-5324.

Chandra S and Batur C (2006), Manipulation of capillary force by electrowetting for micromanipulation, *NSTI-Nanotech*, **3**, 578-581.

Chen WT (1971), Computation of stresses and displacements in a layered elastic medium, *Int. J. Eng. Sci.* **9**, 775–800.

Chen WT and Engel PA (1972), Impact and contact stress analysis in multilayer media, *Int. J. Solids Struct.* **8**, 1257–1281.

Chilamakuri SK and Bhushan B (1998), Contact analysis of non- Gaussian random surfaces, *Proc. Inst. Mech. Eng., Part J: J. Eng. Tribol*. **212**, 19–32.

Chilamakuri SK and Bhushan B (1999), A comprehensive kinetic meniscus model for prediction of long-term static friction, *J. Appl. Phys.* **86**, 4649-4656.

Clark WC, Haynes JM and Mason G (1968), Liquid bridges between a sphere and a plane, *Chem. Engng. Sci*. **23**, 810-812.

Cole SJ and Sayles RS (1992), A numerical model for the contact of layered elastic bodies with real rough surfaces, *ASME J. Tribol.* **114**, 334–340.

Cross NL and Picknett RG (1963a), *Particle adhesion in the presence of a liquid film, In the Mechanism of Corrosion by Fuel Impurities* (ed. H. R. Johnson and D. H. Littler), London: Butterworths.

Cross NL and Picknett RG (1963b), The liquid layer between Spheres and a plane surface. *Trans. Faraday Soc*. **59**, 846-855.

de Boer MP and de Boer PCT (2007), Thermodynamics of capillary adhesion between rough surfaces, *J. Colloid. Inter. Sci.*, **311**, 171–185.

Defay R and Prigogine I (1966), *In surface tension and absorption*, Wiley, New York.
Diao DF, Kato K, and Hayashi K (1994), The maximum tensile stress on a hard coating under sliding friction, *Tribol. Int.* **27**, 267–272.

Erle MA, Dyson DC and Morrow NR (1971), Liquid bridges between cylinders, in a torus, and between spheres, *A. I. Ch. E. J*. **17**, 115-121.

Everett DH (1967), *In the Solid-Gas Interface*, edited by E. A. Flood, Dekker, New York, **2**, 1055-1113.

Fisher RA (1926), On the capillary forces in an ideal soil; correction of formulae given by W. B. Haines, *J. Agric. Sci*. **16**, 492–505.

Fortes MA (1982), Axisymmetric liquid bridges between parallel plates, *J. Colloid. Inter. Sci*. **88**, 338–352.

Gao C (1997), Theory of menisci and its applications, *Appl. Phys. Lett*. **71,** 1801-1803.

Gorb S (2001), *Attachment devices of insect cuticle*, Dordrecht, Boston, London: Kluwer Academic Publishers.

Gupta PK and Walowit JA (1974), Contact stresses between an elastic cylinder and a layered elastic solid, *ASME J. Lubr. Technol.* **96**, 250–257.

Gupta PK, Walowit JA, and Finkin EF (1973), Stress distributions in plane strain layered elastic solids subjected to arbitrary boundary loading, *ASME J. Lubr. Technol.* **95**, 427–432.

Haines WB (1925), A note on the cohesion developed by capillary forces in an ideal soil, *J. Agric. Sci*. **15**, 529-543.

Halsey TC, Levine AJ (1998), How Sandcastles Fall, *Phys. Rev. Lett*. **80**, 3141-3144.
Heady RB and Cahn JW (1970), An analysis of the capillary forces in liquid-phase sintering of spherical particles, *Met. Trans*. **1**, 185-189.

Hibbeler RC (1999), *Mechanics of Materials*, 4th Edition, Prentice Hall, New Jersey.

Hocking LM (1973), The effect of slip on the motion of a sphere close to a wall and of two adjacent spheres, *J. Eng. Maths*. **7**, 207-218.

Hornbeck LJ (1999), A digital light processing update – status and future application, Proc. SPIE **3634**, 158-170.

Hotta K, Takeda K and Iinoya K (1974), The capillary binding force of a liquid bridge, *Powder Technol*. **10**, 231-242.

Huppmann WJ and Riegger H (1975), Modeling of rearrangement processes in liquid phase sintering, Acta metall. **23**, 965-971.

Israelachvili JN (1992), *Intermolecular and Surface Forces*, 2nd ed. (San Diego: Academic).

Johnson KL (1985) *Contact Mechanics*, Cambridge University Press, Cambridge, U.K.
Kalker JJ and van Randen Y (1972), A minimum principle for frictionless elastic contact with application to non-Hertzian half-space contact problems, *J. Eng. Math.* **6**, 193–206.

Kannel JW and Dow TA (1985), Evaluation of contact stress between rough elastic and layered cylinders, *Leed-Lyon Conf*, Butterworths, 198–206.

Kikuchi N and Oden JT (1988), *Contact Problems in Elasticity: AStudy of Variational Inequalities and Finite Element Methods*, SIAM, PA.

King RB and O'Sullivan TC (1987), Sliding contact stresses in a two-dimensional layered elastic half-space, *Int. J. Solids Struct.* **23**, 581–597.

Komvopoulos K (1988), Finite element analysis of a layered elastic solid in normal contact with a rigid surface, *ASME J. Tribol.* **110**, 477–485.

Komvopoulos K (1989), Elastic-plastic finite element analysis of indented layered media, *ASME J. Tribol.* **111**, 430–439.

Komvopoulos K and Choi DH (1992), Elastic finite element analysis of multi-asperity contact, *ASME J. Tribol.* **114**, 823–831.

Kral ER and Komvopoulos K (1996a), Three-dimensional finite element analysis of surface deformation and stresses in an elastic-plastic layered medium subjected to indentation and sliding contact loading, *ASME J. Appl. Mech.* **63**, 365–375.

Kral ER and Komvopoulos K (1996b), Three-dimensional finite element analysis of subsurface stresses and shakedown due to repeated sliding on a layered, *ASME J. Appl. Mech.* **63**, 967–973.

Kral ER and Komvopoulos K (1997), Three-dimensional finite element analysis of subsurface stress and strain fields due to sliding contact on an elastic-plastic layered medium, *ASME J. Tribol.* **119**, 332–341.

Kral ER, Komvopoulos K, and Bogy DB (1993), Elastic-plastic finite element analysis of repeated indentation of a half-space by a rigid sphere, *ASME J. Appl. Mech.* **60**, 829–841.

Kral ER, Komvopoulos K, and Bogy DB (1995a), Finite element analysis of repeated indentation of an elastic-plastic layered medium by a rigid sphere, Part I: Surface results, *ASME J. Appl. Mech.* **62**, 20–28.

Kral ER, Komvopoulos K, and Bogy DB (1995b), Finite element analysis of repeated indentation of an elastic-plastic layered medium by a rigid sphere, Part II: Subsurface results, *ASME J. Appl. Mech.* **62**, 29–42.

Lee J, Moon H, Fowler J, Schoellhammer T and Kim CJ (2002), Electrowetting and electrowetting-on-dielectric for micro scale liquid handling, *Sensors and Actuator*, **95**,259-268.

Lian G, Thornton C and Adams MJ (1993), A Theoretical Study of the Liquid Bridge Forces between Two Rigid Spherical Bodies, *J. Colloid. Inter. Sci*. **161**, 138-147.

Liu S and Wang Q (2002), Studying Contact Stress Fields Caused by Surface Tractions With a Discrete Convolution and Fast Fourier Transform Algorithm, *ASME J. Tribol.* **124**, 36–45.

Malvern LE (1969), *Introduction to the Mechanics of a Continuous Medium*, Prentice-Hall, New York.

Man KW (1994), *Contact Mechanics using Boundary Elements*, Computational Mechanics Publications, Boston MA.

Mao K, Sun Y, and Bell T (1996), A numerical model for the dry sliding contact of layered elastic bodies with rough surfaces, *Tribol. Trans.* **39**, 416–424.

Mao K, Bell T, and Sun Y (1997), Effect of sliding friction on contact stresses for multilayered elastic bodies with rough surfaces, *ASME J. Tribol.* **119**, 476–480.

Marion JE, Evans AG, Drory MD and Clarke DR (1983), High temperature failure initiation in liquid phase sintered materials, *Acta metall*. **31**, 1445-1457.

Martin JAC, Oden JT, and Simoes FMF (1990), A study of statix and kinetic friction, *Int. J. Eng. Sci.* **28**, 29–92.

Mason G and Clark WG (1965), Zero force liquid bridges between spherical particles, *Brit. Chem. Engng*. **10**, 859-866.

Mastrangelo CH and Hsu CH (1993), Mechanical stability and adhesion of microstructures under capillary forces. I. Basic theory, *J. Microelectromech. Syst*. **2**, 33-43.

Mate CM (1992), Application of disjoining and capillary pressure to liquid lubricant films in magnetic recording, *J. Appl. Phys*. **72**, 3084-3090.

Matsuoka H, Fukui S and Morishita H (2002), Dynamics of liquid meniscus bridge of intermittent contact slider, *IEEE Trans. Mag.* **38**, 2135-37.

Matthewson MJ (1988), Adhesion of spheres by thin liquid films, *Phil. Mag*. A, **57**, 207-216.

McFarlane J S and Tabor D (1950), Adhesion of solids and the effects of surface films *Proc. R. Soc. A* **202**, 224-43.

McHaffie IR and Lenher S (1925), The adsorption of water from the gas phase on. plane surfaces of glass and platinum, *J. Chem. Soc*., **127**, 1559-1572.

Melrose JC (1966), Model calculations for capillary condensation, *A.I.Ch.E. J*. **12**, 986-994.

Merriman T and Kannel J (1989), Analyses of the role of surface roughness on contact stresses between elastic cylinders with and without soft surface coating, *ASME J. Tribol.* **111**, 87–94.

Miyoshi KD, Buckley T, Kusaka C, Maeda and B.Bhushan (1988), *in Tribology and Mechanics of Magnetic Storage Systems*, edited by B. Bhushan and N. S. Eiss, ASLE, Park Ridge, IL.

Nogi T and Kato T (1997), Influence of a hard surface layer on the limit of elastic contact-Part I: Analysis using a real surface model, *ASME J. Tribol.* **119**, 493–500.

O'Sullivan TC and King RB (1988), Sliding contact stress field due to a spherical indenter on a layered elastic half-space, *ASME J. Tribol.* **110**, 235–240.

Obata KJ, Mokotado T, Saito S, Takahasi K (2004), A scheme for micro-manipulation based on capillary force, *J. Fluid.Mech.* **498**, 113-121.

O'Brien WJ and Yu CU (1972), Tensile strength of liquid bridges under reduced pressure, *Surface Sci*. **32**, 739-742.

Oden JT and Martin JAC (1985), Models and computational methods for dynamic friction phenomena, *Comput. Methods Appl. Mech. Eng.* **52**, 527–634.

Orr FM, Scriven LE and Rivas AP (1975), Pendular rings between solids: meniscus properties and capillary force, *J. Fluid Mech*. **67**, 723-742.

Padday JF, Pitt AR and Pashley RM (1975), Menisci at a free liquid surface: surface tension from the maximum pull on a rod, *J. Chem. Soc. Faraday Trans*. **1**, 1919-1931.

Peng W and Bhushan B (2001), A numerical three-dimensional model for the contact of layered elastic/plastic solids with rough surfaces by a variational principle, ASME *J. Tribol*. **123**, 330–342.

Peng W and Bhushan B (2002), Sliding Contact Analysis of Layered Elastic/Plastic Solids With Rough Surfaces, ASME J. Tribol. **124**, 46–61.

Peng W and Bhushan B (2003), Transient analysis of sliding contact of layered elastic/plastic solids with rough surfaces, *Microsys Technol*. **9**, 340-345.

Plumet S and Dubourg MC (1998), A 3-D model for a multilayered body loaded normally and tangentially against a rigid body: Application to specific coatings, *ASME J. Tribol.* **120**, 668–676.

Polonsky A and Keer LM (1999), A numerical method for solving rough contact problems based on the multi-level multi-summation and conjugate gradient techniques, *Wear* **231**, 206–219.

Polonsky A and Keer LM (2000a), A fast and accurate method for numerical analysis of elastic layered contacts, *ASME J. Tribol.* **122**, 30–35.

Polonsky A and Keer LM (2000b), Fast methods for solving rough contact problems: A comparative study, *ASME J. Tribol.* **122**, 36–41.

Poon CY and Bhushan B (1995), Comparison of surface roughness measurements by stylus profiler, AFM and non-contact optical pro-filer, *Wear* **190**, 76–88.

Poon CY and Bhushan B (1996), Numerical contact and stiction analyses of Gaussian isotropic surfaces for magnetic head slider/disk contact, *Wear* **202**, 68–82.

Press WH, Teukolsky SA, Vetterling WT and Flannery BP (1999), *Numerical Recipes in FORTRAN, the Art of Scientific Computing*, 2nd ed., Cambridge University Press, Cambridge, UK.

Richards TH (1977), *Energy Methods in Stress Analysis: with an Introduction to Finite Element Techniques*, Halsted, New York.

Robbins RA and Jacobs SJ (2001), U.S. Patent No. 6,300,294 B1.

Rose W (1958), Volumes and surface areas of pendular rings, *J. Appl. Phys*. **29**, 687-691.
Shaw T (1986), Liquid redistribution during liquid-phase sintering, *Am. Ceram.Bull. Soc*. **69**, 27-34.

Singh S, Houston J, Swol FV and Brinker CJ (2006), Superhydrophobicity: Drying transition of confined water, *Nature* **442**, 526-527.

Smith JO and Liu CK (1953), Stress due to tangential and normal loads on an elastic solid with application to some contact stress problems, *ASME J. Appl. Mech.* **201**, 157–166.

Sokolnikoff IS (1956) *Mathematical Theory of Elasticity*, 2nd Edition, McGraw-Hill, New York.
Stephens LS, Liu Y, and Meletis EI (2000), Finite element analysis of the initial yielding behavior of a hard coating/substrate system with functionally graded interface under indentation and friction, *ASME J. Tribol.* **122**, 381–387.

Stanley HM, Kato T (1997), An FFT-based method for rough surfaces contact, *ASME J. Tribol.* **119**, 481–485.

Stifter T, Marti O, and Bhushan B (2000), Theoretical investigation of the distance dependence of capillary and van der waals forces in scanning force microscopy, *Phys. Rev. B*, **62**, 667-673.

Thomson W (1870), *Pro. R. Soc. Edinburgh* **7**, 170-181.

Tian X and Bhushan B (1996a), A Numerical Three-dimensional Model for the Contact of Rough Surfaces by Variational Principle, *ASME J. Tribol*. **118**, 33–41.

Tian X and Bhushan B (1996b), The micro-meniscus effect of thin liquid film on the static friction of rough surface contact, *J. Phys. D: Appl. Phys*. **29**, 163–178.

Tsai RL and Raj R (1982), Creep Fracture in ceramics containing small amounts of liquid phase, *Acta metall*. **30**, 1043-1058.

Willett CD, Adams MJ, Johnson SA, Seville JPK (2000), Capillary Bridges between Two Spher ical Bodies, *Langmuir* **16**, 9396-9405.

Woodrow J, Chilton H, and Hawes RI (1961), Forces between slurry particles due to surface tension, *J. Nucl. Energy B, Reactor Tech*. **2**, 229–237.

Yu MH, Bhushan B (1996), Contact analysis of three-dimensional rough surfaces under frictionless and frictional contact, *Wear* **200**, 265-280.

Zienkiewicz OC (1977), *The Finite Element Method*, McGraw-Hill,New York.

APPENDIX A

EQUATIONS FOR VON MISES STRESS, PRINCIPAL TENSILE STRESS AND SHEAR STRESS

In this appendix, we present equations for von Mises, principal tensile and shear stresses. The normal and shear stresses acting on a volume element are shown in Fig. A.1 (Hibbeler, 1999).

The von Mises stresses are calculated as these relate to the von Mises yield criterion. According to this criterion, plastic yielding initiates once the maximum von Mises stresses reaches the yield stress in pure shear. The von Mises stress is given by

$$J_2 = \frac{1}{6}\left[\left(\sigma_{xx} - \sigma_{yy}\right)^2 + \left(\sigma_{yy} - \sigma_{zz}\right)^2 + \left(\sigma_{zz} - \sigma_{xx}\right)^2\right] + \sigma_{xy}^2 + \sigma_{yz}^2 + \sigma_{xz}^2$$

(A.1)

Principal tensile stresses affect propensity of crack propagation which is important in brittle materials. The principal tensile stress is given by

$$\sigma_t = \frac{\sigma_{xx} + \sigma_{yy}}{2} + \frac{1}{2}\sqrt{\left(\sigma_{xx} - \sigma_{yy}\right)^2 + 4\sigma_{xy}^2}$$

(A.2)

Shear stresses are related to the commonly used Tresca yield criterion. According to this criterion, the yielding will occur when the shear stress reaches the yield stress in

pure shear. Since we assume that the substrate and the layers are all isotropic, σ_{xz} is selected to represent the shear stress.

The von Mises, principal tensile and shear stress components are calculated using Eq. (20) in frequency domain.

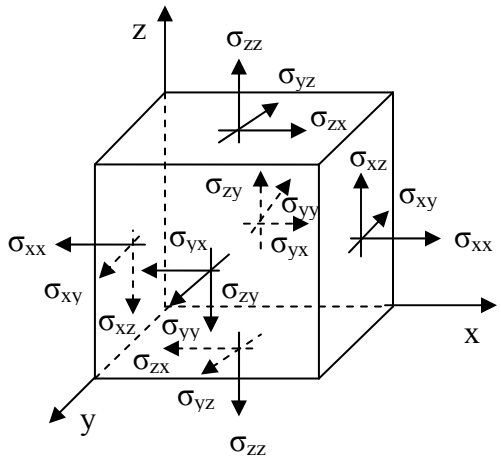

Fig. A.1 Schematic showing normal and shear stresses acting on a volume element.

APPENDIX B

THE INTERMEDIATE VARIABLES FOR THE COEFFICIENTS IN THE INFLUENCE COEFFICIENT MATRIX

The intermediate variables k_1 to k_{26}, R_1 to R_{10}, and R_a to R_d for Eq. (3.25-3.31)

$$k_1 = \frac{h_1}{G_{12}} - h_1 - \frac{2(1-\nu_1)}{\alpha}$$

$$k_2 = \frac{h_1}{G_{12}} - h_1 + \frac{2(1-\nu_1)}{\alpha}$$

$$k_3 = \frac{1}{G_{12}}\left(\frac{3-4\nu_1}{\alpha} + h_1\right) - \frac{1-2\nu_1}{\alpha} - h_1$$

$$k_4 = \frac{1}{G_{12}}\left(\frac{3-4\nu_1}{\alpha} - h_1\right) - \frac{1-2\nu_1}{\alpha} + h_1$$

$$k_5 = \frac{(3-4\nu_2)(1-2\nu_2)}{2(\nu_2-1)}\left[\frac{1}{G_{12}(3-4\nu_1)} - \frac{1}{1-2\nu_2}\right]$$

$$k_6 = \frac{(3-4\nu_2)(1-2\nu_2)}{2\alpha(\nu_2-1)}\left[\frac{3-4\nu_1+\alpha h_1}{G_{12}(3-4\nu_1)} - \frac{1-2\nu_1+\alpha h_1}{1-2\nu_2}\right]$$

$$k_7 = \frac{(3-4\nu_2)(1-2\nu_2)}{2\alpha(\nu_2-1)}\left[\frac{3-4\nu_1-\alpha h_1}{G_{12}(3-4\nu_1)} - \frac{1-2\nu_1-\alpha h_1}{1-2\nu_2}\right]$$

$$k_8 = \frac{(3-4\nu_2)(1-2\nu_2)}{2\alpha(\nu_2-1)}\left[\frac{G_2 R_4}{(3-4\nu_2)} - \frac{R_5}{1-2\nu_2}\right]$$

$$k_9 = \frac{1}{3-4\nu_3} G_3(\alpha R_7 + R_8)$$

$$k_{10} = \frac{1}{3-4\nu_3}\frac{2\alpha h_2 - 3 + 4\nu_2}{G_{23}}$$

$$k_{11} = \frac{3-4\nu_2}{G_{23}(3-4\nu_3)}$$

$$k_{12} = \alpha(1-\frac{1}{G_{23}})e^{-\alpha h_2}$$

$$k_{13} = \left[-\alpha - \frac{\alpha}{G_{23}} + (1-2\nu_3)\frac{2\alpha}{G_{23}(3-4\nu_3)}\right]e^{\alpha h_2}$$

$$k_{14} = \left[(1-2\nu_2) + \alpha h_2 - \frac{\alpha h_2}{G_{23}} - (1-2\nu_3)k_{11}\right]e^{-\alpha h_2}$$

$$k_{15} = \left[(1-2\nu_2) - \alpha h_2 - \frac{\alpha h_2}{G_{23}} + (1-2\nu_3)k_{10}\right]e^{\alpha h_2}$$

$$k_{16} = \left[\alpha - \frac{\alpha}{G_{23}} + (1-\nu_3)\frac{4\alpha}{G_{23}(3-4\nu_3)}\right]e^{\alpha h_2}$$

$$k_{17} = \left[2(1-\nu_2) + \alpha h_2 - \frac{\alpha h_2}{G_{23}} - (1-2\nu_3)k_{11}\right]e^{-\alpha h_2}$$

$$k_{18} = \left[-2(1-\nu_2) + \alpha h_2 - \frac{\alpha h_2}{G_{23}} + (1-2\nu_3)k_{10}\right]e^{\alpha h_2}$$

$$k_{19} = \left[\frac{1}{2}k_{12}(\frac{1}{G_{12}} + k_5) + \frac{1}{2}k_{13}(\frac{1}{G_{12}} - k_5) + \frac{k_{15}\alpha}{2(1-\nu_2)}(\frac{1}{G_{12}} - 1)\right]e^{-\alpha h_1}$$

$$k_{20} = \left[\frac{1}{2}k_{12}(\frac{1}{G_{12}} - k_5) + \frac{1}{2}k_{13}(\frac{1}{G_{12}} + k_5) + \frac{k_{14}\alpha}{2(-1+\nu_2)}(\frac{1}{G_{12}} - 1)\right]e^{\alpha h1}$$

$$k_{21} = \left[\frac{1}{2}k_{12}(\frac{h_1}{G_{12}} + k_6) + \frac{1}{2}k_{13}(\frac{h_1}{G_{12}} - k_6) + \frac{k_{14}\alpha}{2(\nu_2 - 1)}(k_1 - k_3) + \frac{k_{15}\alpha}{2(1-\nu_2)}(k_1 + k_3)\right]e^{-\alpha h_1}$$

$$k_{22} = \left[\frac{1}{2}k_{12}(\frac{h_1}{G_{12}} + k_7) + \frac{1}{2}k_{13}(\frac{h_1}{G_{12}} + k_7) + \frac{k_{14}\alpha}{2(\nu_2 - 1)}(k_2 - k_4) + \frac{k_{15}\alpha}{2(1-\nu_2)}(k_2 + k_4)\right]e^{\alpha h_1}$$

$$k_{23} = \left[\frac{1}{2}k_{12}(\frac{h_1}{G_{12}} + k_5) + \frac{1}{2}k_{16}(\frac{1}{G_{12}} - k_5) + \frac{k_{18}\alpha}{2(1-\nu_2)}(\frac{1}{G_{12}} - 1)\right]e^{-\alpha h_1}$$

$$k_{24}=\left[\frac{1}{2}k_{12}(\frac{h_1}{G_{12}}-k_5)+\frac{1}{2}k_{16}(\frac{1}{G_{12}}+k_5)+\frac{k_{17}\alpha}{2(-1+\nu_2)}(\frac{1}{G_{12}}-1)\right]e^{\alpha h_1}$$

$$k_{25}=\left[\frac{1}{2}k_{12}(\frac{h_1}{G_{12}}+k_6)+\frac{1}{2}k_{16}(\frac{1}{G_{12}}-k_5)+\frac{k_{17}\alpha}{4(\nu_2-1)}(k_1-k_3)+\frac{k_{18}\alpha}{4(1-\nu_2)}(k_1+k_3)\right]e^{-\alpha h_1}$$

$$k_{26}=\left[\frac{1}{2}k_{12}(\frac{h_1}{G_{12}}+k_{76})+\frac{1}{2}k_{16}(\frac{1}{G_{12}}-k_7)+\frac{k_{17}\alpha}{4(\nu_2-1)}(k_2-k_4)+\frac{k_{18}\alpha}{4(1-\nu_2)}(k_2+k_4)\right]e^{\alpha h_1}$$

$$R_1=-\frac{1}{\alpha}\left[\tilde{p}(\xi,\eta,0)+2i\xi(1-\nu_1)(B_1+\overline{B}_1)+i\alpha^2(B_{1,1}+\overline{B}_{1,1})\right]$$

$$R_2=-\frac{1}{i}\left[\frac{\xi}{\alpha}(B_1-\overline{B}_1)+\alpha(B_{1,1}-\overline{B}_{1,1})\right]$$

$$R_3=\frac{1}{i}\left[-\frac{1}{G_2}(B_{2,1}+\overline{B}_{2,1})-\frac{1}{\alpha G_1}\xi h_1(B_1e^{-\alpha h_1}-\overline{B}_1e^{\alpha h_1})+\frac{1}{G_1}\xi h_1(B_{1,1}e^{-\alpha h_1}-\overline{B}_{1,1}e^{\alpha h_1})\right]$$

$$R_4=-\frac{i}{\alpha G_2}\xi(B_2-\overline{B}_2)+\frac{i}{G_2}a(-B_{2,1}+\overline{B}_{2,1})-\frac{i}{G_1}\xi h_1(B_1e^{-\alpha h_1}+\overline{B}_1e^{\alpha h_1})+\frac{i}{\alpha G_1}\xi(B_1e^{-\alpha h_1}-\overline{B}_1e^{\alpha h_1})$$
$$-\frac{i}{G_1}\alpha(-B_{1,1}e^{-\alpha h_1}+\overline{B}_{1,1}e^{\alpha h_1})$$

$$R_5=-\frac{1}{i}\left[\begin{array}{l}\frac{1}{\alpha}\xi B_2-\frac{1}{\alpha}\xi\overline{B}_2-\alpha(-B_{2,1}+\overline{B}_{2,1})-(\frac{1}{\alpha}-h_1)\xi B_1e^{-\alpha h_1}+(\frac{1}{\alpha}+h_1)\xi\overline{B}_1e^{\alpha h_1}\\+\alpha(-B_{1,1}e^{-\alpha h_1}+\overline{B}_{1,1}e^{\alpha h_1})\end{array}\right]$$

$$R_6=-\frac{1}{\alpha}\left[\begin{array}{l}2i\xi(1-\nu_2)(B_2+\overline{B}_2)-i\alpha^2(B_{2,1}+\overline{B}_{2,1})-2i\xi(1-\nu_2)(B_1e^{-\alpha h_1}+\overline{B}_1e^{\alpha h_1})\\+i\alpha\xi h_1(B_1e^{-\alpha h_1}-\overline{B}_1e^{\alpha h_1})-i\alpha^2(-B_{1,1}e^{-\alpha h_1}+\overline{B}_{1,1}e^{\alpha h_1})\end{array}\right]$$

$$R_7=\frac{1}{i}\left[-\frac{1}{G_3}B_{3,1}-\frac{1}{\alpha G_2}\xi h_2(B_2e^{-\alpha h_2}-\overline{B}_2e^{\alpha h_2})+\frac{1}{G_2}(B_{2,1}e^{-\alpha h_2}-\overline{B}_{2,1}e^{\alpha h_{21}})\right]$$

$$R_8=-\frac{i}{\alpha G_3}\xi B_3+\frac{i}{G_2}a-B_{3,1}-\frac{i}{G_2}\xi h_2(B_2e^{-\alpha h_2}+\overline{B}_2e^{\alpha h_2})+\frac{i}{\alpha G_2}\xi(B_2e^{-\alpha h_2}-\overline{B}_1e^{\alpha h_2})$$
$$-\frac{i}{G_2}\alpha(-B_{2,1}e^{-\alpha h_2}+\overline{B}_{2,1}e^{\alpha h_2})$$

$$R_9=-\frac{1}{i}\left[\frac{1}{\alpha}\xi B_3+\alpha B_{3,1}-(\frac{1}{\alpha}-h_2)\xi B_2e^{-\alpha h_2}+(\frac{1}{\alpha}+h_2)\xi\overline{B}_2e^{\alpha h_2}+\alpha(-B_{2,1}e^{-\alpha h_2}+\overline{B}_{2,1}e^{\alpha h_2})\right]$$

$$R_{10} = -\frac{1}{\alpha}\begin{bmatrix} 2i\xi(1-\nu_3)B_3 + i\alpha^2 B_{3,1} - 2i\xi(1-\nu_2)(B_2 e^{-\alpha h_2} + \overline{B}_2 e^{\alpha h_2}) + i\alpha\xi h_2 (B_2 e^{-\alpha h_2} - \overline{B}_2 e^{\alpha h_2}) \\ - i\alpha^2(-B_{2,1} e^{-\alpha h_2} + \overline{B}_{2,1} e^{\alpha h_2}) \end{bmatrix}$$

$$R_a = -\alpha G_3 R_7 + (1-2\nu_3)k_9 + R_9$$

$$R_b = -\alpha G_3 R_7 + 2(1-\nu_3)k_9 + R_{10}$$

$$R_c = R_a - \frac{k_{12}}{2}(k_8 - G_2 R_3) + \frac{k_{13}}{2}(k_8 + G_2 R_3) - \frac{k_{14}}{4(\nu_2 - 1)}(-G_2 R_3 + \frac{R_6 - G_2 R_4 - R_5}{\alpha})$$
$$- \frac{k_{14}}{4(\nu_2 - 1)}(-G_2 R_3 + \frac{R_6 + G_2 R_4 + R_5}{\alpha})$$

$$R_d = R_b - \frac{k_{12}}{2}(k_8 - G_2 R_3) + \frac{k_{16}}{2}(k_8 + G_2 R_3) - \frac{k_{17}}{4(\nu_2 - 1)}(-G_2 R_3 + \frac{R_6 - G_2 R_4 - R_5}{\alpha})$$
$$- \frac{k_{18}}{4(\nu_2 - 1)}(-G_2 R_3 + \frac{R_6 + G_2 R_4 + R_5}{\alpha})$$